Lehrstuhl E15
Physik - Department
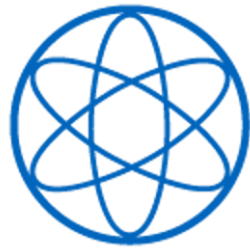
Development of a muon track reconstruction with the inner veto of Double Chooz

Diplomarbeit

Vincenz Zimmer

18. November 2010

Technische Universität München

Abstract

DOUBLE CHOOZ is a reactor neutrino experiment designed to search for the last unknown neutrino mixing angle ϑ_{13}. To achieve a high sensitivity two identical cylindrical detectors are used. A near detector monitors the electron antineutrino flux from the reactor and its spectral shape without oscillation effects, and a far detector is used to measure changes in the flux and shape due to the influence of ϑ_{13}. After three years of data taking with both detectors it is intended to reach a sensitivity of $\sin^2(2\vartheta_{13}) \leq 0.03$ in case of no positive signal.

The electron antineutrinos from the nuclear reactors are detected using the inverse beta decay reaction, which causes a delayed coincidence signal in the detector. Due to this clear signature the background candidates affecting the sensitivity are effectively reduced to those, which mimic such a delayed coincidence: fast neutrons and the β-n-emitters ^{8}He and ^{9}Li, which are produced by muons inside or in the vicinity of the detectors. A muon track reconstruction provides a tool to reject these backgrounds or to increase the understanding regarding the production processes.

In the present work two approaches for a muon track reconstruction using the inner veto of DOUBLE CHOOZ were studied. Both developed algorithms rely on the reconstruction of an inner veto entry and exit point. The reconstructed muon track is approximated to be the straight line defined by both points.

A first approach was the barycenter method, which uses the timing and charge information of the hit PMTs to reconstruct the entry and exit points using a barycenter formula. Inspired by problems in the early phase of the studies on the barycenter method a second approach has been studied: the maximum likelihood method uses histograms, containing the correlated information between the timing information and the distance to the true muon track as probability density functions. The entry and exit points are reconstructed to be the points at the top and the bottom inner veto with the best agreement between the timing data of the hits and the probability density functions.

To test both tracking algorithms detailed Monte Carlo simulations of vertical and inclined muons were performed. The barycenter method shows very similar results for vertical and inclined muons suggesting that this method is very robust regarding the degree of inclination of the muons. The accuracy in the determination of the inner veto entry and exit points is in the order of 25 cm. The resulting accuracy for the muon momentum direction is about 3.5 degrees.

The maximum likelihood method shows very good results for vertical muons with accuracies, which are roughly a factor of two better than for the barycenter method. The entry point reconstruction performs even more precisely for inclined muons with an accuracy of about 11 cm, while the exit point reconstruction suffers from highly inclined muons and has an accuracy of about 23 cm. Nevertheless, the muon momentum direction can be determined with an angular resolution of about 2.3 degrees.

Contents

1 Introduction

1.1 The standard model of particle physics

The standard model of particle physics [Alt05, Hal84, Pov94] describes the fundamental interactions between quarks and leptons - the elementary components of which all the visible matter is made of. Leptons and quarks are fermions, i.e. they have spin 1/2. In sum, there are 6 leptons and 6 quarks and their antiparticles, which have the same mass and lifetime, but the opposite electrical charge and quantum numbers. Leptons and quarks can be divided into three generations (also called families) each (see table 1.1). For the leptons a generation consists of a charged particle and an uncharged neutrino. A quark generation consists of a quark with charge $+2/3|e|$ and a quark with charge $-1/3|e|$, where $|e| = 1.6022 \cdot 10^{-19}$ C is the elementary charge.

LEPTONS				QUARKS			
symbol	name	$Q/|e|$	mass	symbol	name	$Q/|e|$	mass
e^-	electron	-1	0.511 MeV	u	up	$+2/3$	1.7-3.3 MeV
ν_e	e-neutrino	0	< 2.5 eV	d	down	$-1/3$	4.1-5.8 MeV
μ^-	muon	-1	105.66 MeV	c	charm	$+2/3$	~ 1.27 GeV
ν_μ	μ-neutrino	0	< 0.17 MeV	s	strange	$-1/3$	~ 100 MeV
τ^-	tauon	-1	1777 MeV	t	top	$+2/3$	~ 172 GeV
ν_τ	τ-neutrino	0	< 18 MeV	b	bottom	$-1/3$	~ 4.2 GeV

Table 1.1: *The fundamental fermions in the standard model of particle physics - the leptons and the quarks. $Q/|e|$ is the charge of the particles in units of the elementary charge $|e| = 1.6022\cdot10^{-19}$ C. The mass values are given in natural units ($c = \hbar = 1$). The quoted upper limits for the neutrino masses come from direct mass measurements. The measured oscillation parameters (see table 1.3) together with cosmological constraints on the sum of the three masses imply neutrino masses which are much smaller ($\lesssim 1$ eV) [Per09, PDG10, Pov94].*

In physics there are 4 fundamental forces known: the strong, the weak, the electromagnetic and the gravitational force. All but the gravitational force are described in the standard model of particle physics (gravitation is specified by the general theory of relativity). The interactions between the particles are mediated by gauge bosons: the strong interaction by so called gluons, the weak interaction by $W^\pm$- and Z^0-bosons and

the electromagnetic interaction by photons. The strong force acts on quarks and gluons only, while the electromagnetic force acts on all charged particles. Thus the uncharged neutrinos are not affected by the electromagnetic force. The weak interaction acts on all particles, but only on left-handed neutrinos and right-handed antineutrinos. Information on the fundamental forces and their gauge bosons is summarized in table 1.2 [Hal84, Per09, Pov94, PDG10].

interaction	relative strength	range	couples to	gauge bosons
strong	1	$< 10^{-15}\,\mathrm{m}$	quarks & gluons	8 gluons
electro-magnetic	10^{-2}	∞	charged particles	photon
weak	10^{-7}	$10^{-18}\,\mathrm{m}$	quarks, leptons, $W^{\pm}$, Z^0, Higgs	$W^{\pm}$ and Z^0
gravitation	10^{-39}	∞	massive particles	graviton

Table 1.2: *The fundamental interactions (strong, weak, electromagnetic and gravitational) and their relative strength, range and gauge bosons [Per09, Pov94].*

1.2 Neutrinos in the standard model

The neutrino was first postulated in 1930 by Wolfgang Pauli to ensure conservation of energy, momentum and spin for the beta decay [Sch97]. Cowan and Reines were able to detect neutrinos experimentally for the first time [Cow56]. They used a liquid scintillator to detect electron antineutrinos from a nuclear reactor via the inverse beta decay. The problem of detecting neutrinos is that neutrinos only interact via the weak interaction resulting in a small cross-section.

In the standard model neutrinos are treated as massless particles. Furthermore, neutrinos are left-handed and antineutrinos are right-handed as the parity is maximally violated for the weak interaction, i.e. the gauge bosons of the weak interaction couple to left-handed neutrinos and right-handed antineutrinos only. Therefore, neutrinos can only be produced with these helicities [Per09, Pov94].

Different neutrino experiments since the 60's found indications for finite neutrino masses, as for example the measured flux of electron neutrinos from the sun was too low compared to the models [Hax95]. This results in the need for an extension of the standard model.

1.3 Neutrinos beyond the standard model

1.3.1 Neutrino oscillations

The above mentioned neutrinos ν_e, ν_μ, and ν_τ are produced by processes of the weak interaction. Hence, they are eigenstates of the weak interaction - also called flavour eigenstates [Akh06]. A non zero mass of the neutrinos means that, in general, the mass eigenstates ν_1, ν_2, and ν_3 need not to be equal to the flavour eigenstates. The flavour eigenstates and the mass eigenstates are related by the Pontecorvo-Maki-Nakagawa-Sakata matrix U (PMNS matrix) (e.g. see [Akh00, Sch97]):

$$
\begin{pmatrix} \nu_e \\ \nu_\mu \\ \nu_\tau \end{pmatrix} = U \begin{pmatrix} \nu_1 \\ \nu_2 \\ \nu_3 \end{pmatrix} = \underbrace{\begin{pmatrix} U_{e1} & U_{e2} & U_{e3} \\ U_{\mu1} & U_{\mu2} & U_{\mu3} \\ U_{\tau1} & U_{\tau2} & U_{\tau3} \end{pmatrix}}_{PMNS\ matrix} \begin{pmatrix} \nu_1 \\ \nu_2 \\ \nu_3 \end{pmatrix} \tag{1.1}
$$

The PMNS matrix can be parametrized by three mixing angles ϑ_{12}, ϑ_{23}, ϑ_{13}, a CP violating phase δ, and two Majorana phases α_1 and α_2 [1] as follows [Akh06]:

$$
U = \begin{pmatrix} 1 & 0 & 0 \\ 0 & c_{23} & s_{23} \\ 0 & -s_{23} & c_{23} \end{pmatrix} \begin{pmatrix} c_{13} & 0 & s_{13}e^{-i\delta} \\ 0 & 1 & 0 \\ -s_{13}e^{i\delta} & 0 & c_{13} \end{pmatrix} \begin{pmatrix} c_{12} & s_{12} & 0 \\ -s_{12} & c_{12} & 0 \\ 0 & 0 & 1 \end{pmatrix} \begin{pmatrix} 1 & 0 & 0 \\ 0 & e^{i\alpha_1} & 0 \\ 0 & 0 & e^{i\alpha_2} \end{pmatrix} \tag{1.2}
$$

where $s_{ij} = \sin\vartheta_{ij}$ and $c_{ij} = cos\vartheta_{ij}$. The time evolution of the mass eigenstates ν_i is given by the Schrödinger equation (in the following natural units are used, i.e. $c = \hbar = 1$) [Bil99]:

$$
|\nu_i(t)\rangle = e^{-iE_it}|\nu_i(t=0)\rangle \tag{1.3}
$$

with the energy E_i of the mass eigenstates i

$$
E_i = \sqrt{p^2 + m_i^2} \overset{m_i \ll p}{\approx} p + \frac{m_i^2}{2p} \overset{p \approx E}{\approx} E + \frac{m_i^2}{2E} \tag{1.4}
$$

approximating that $p \approx E$ and that the masses of the neutrinos m_i are finite but small compared to the momentum p, i.e. $m_i \ll p$. With equation (1.1) and equation (1.3) the time evolution of the flavour eigenstate ν_α can be written as

$$
|\nu_\alpha(t)\rangle = \sum_{i=1}^{3} U_{\alpha i}|\nu_i(t)\rangle = \sum_{i=1}^{3} U_{\alpha i}e^{-iE_it}|\nu_i(t=0)\rangle \tag{1.5}
$$

With equations (1.1)-(1.5) the probability to detect a neutrino with flavour ν_β, when this neutrino was created with flavour ν_α, is:

---

[1] The Majorana phases only occur in the case that neutrinos are Majorana particles, i.e. particles which are their own antiparticles. The Majorana phases do not affect neutrino oscillations and thus will be omitted hereafter [Akh00, Akh06]

$$P_{\nu_\alpha \to \nu_\beta} = |\langle \nu_\beta | \nu_\alpha (t) \rangle|^2 \overset{\langle \nu_i | \nu_j \rangle = \delta_{ij}}{=} \left| \sum_{i=1}^{3} U_{\alpha i} U_{\beta i}^* e^{-iE_i t} \right|^2 \tag{1.6}$$

where the $U_{\beta i}^*$ are the matrix elements of the complex conjugated PMNS matrix.

For the DOUBLE CHOOZ experiment, as it uses the inverse beta decay to detect the electron antineutrino $\bar{\nu}_e$ from a nuclear reactor (see chapter 2), the transition probability $P_{\bar{\nu}_e \to \bar{\nu}_e}$ is of special interest and is [Bil01]

$$
\begin{aligned}
P(\bar{\nu}_e \to \bar{\nu}_e) = 1 \quad &- \quad 4 \cdot \sin^2 \vartheta_{13} \cdot \cos^2 \vartheta_{13} \cdot \sin^2 \left(\frac{\Delta m_{31}^2 L}{4E} \right) \\
&- \quad \cos^4 \vartheta_{13} \cdot \sin^2 (2\vartheta_{12}) \cdot \sin^2 \left(\frac{\Delta m_{21}^2 L}{4E} \right) \\
&+ \quad 2 \sin^2 \vartheta_{13} \cdot \cos^2 \vartheta_{13} \cdot \sin^2 \vartheta_{12} \cdot \\
&\qquad \cdot \left(\cos \left(\frac{\Delta m_{31}^2 L}{2E} - \frac{\Delta m_{21}^2 L}{2E} \right) - \cos \left(\frac{\Delta m_{31}^2 L}{2E} \right) \right)
\end{aligned}
\tag{1.7}
$$

for a $\bar{\nu}_e$ with energy E and at a distance L to the neutrino source. The $\Delta m_{ij}^2 = m_i^2 - m_j^2$ are the differences of the squared masses. At this point one can see that oscillations are only possible, when the different neutrino masses have different values. In particular, that means that at least one neutrino mass has to be non-zero. The second term of equation (1.7) corresponds to oscillations due to $\Delta m_{atm}^2 \approx \Delta m_{31}^2 \approx \Delta m_{32}^2$ and the third term to oscillations due to $\Delta m_\odot^2 \approx \Delta m_{21}^2$ (here the sign is known because of the so-called MSW effect [2]). The last term in equation (1.7) is an interference term between the amplitudes corresponding to the first three.

1.3.2 Measured oscillation parameters

Some of the parameters characterizing neutrino oscillations could be measured up to now [PDG10]. For $\sin^2 (2\vartheta_{13})$ an upper limit can be quoted. In table 1.3 all the currently known values and limits are shown. The upper limit for $\sin^2 (2\vartheta_{13})$ was calculated with the lower bound value of Δm_{32}^2 measured by MINOS and the data from the CHOOZ experiment [PDG10].

1.3.3 Experiments to search for ϑ_{13}

There are two favoured possibilities for current and near future experiments to measure ϑ_{13}: on the one hand the so-called superbeam experiments and on the other hand reactor neutrino experiments like DOUBLE CHOOZ.

---

[2]The Mikheyev–Smirnov–Wolfenstein (MSW) effect is a process where the oscillation probability is resonantly increased by matter effects [Akh00]. The signs of the different Δm_{ij}^2 are of interest as they define the hierarchy of the mass eigenstates.

parameter	measured value (90% C.L.)	mainly determined by
$\sin^2 2\vartheta_{12}$	0.87 ± 0.03	KamLAND & solar ν's
Δm_{21}^2	$7.59^{+0.19}_{-0.21} \cdot 10^{-5}\,\mathrm{eV}^2$	KamLAND & solar ν's
$\sin^2 2\vartheta_{23}$	> 0.92	Super-Kamiokande
Δm_{32}^2	$(2.43 \pm 0.13) \cdot 10^{-3}\,\mathrm{eV}^2$ (68% C.L.)	MINOS
$\sin^2 2\vartheta_{13}$	< 0.16	Chooz

Table 1.3: *The measured oscillation parameters and limits: the upper limit for $\sin^2 (2\vartheta_{13})$ from the first Chooz experiment was calculated with the lower 68 % C.L. value for $\Delta m_{32}^2 = 2.3 \cdot 10^{-3}\,eV^2$. All data were taken from [PDG10].*

Superbeam experiments:

Superbeam experiments use a neutrino beam produced at an accelerator for oscillation measurements [Hub07, Ard04]. These beams consist of muon neutrinos and antineutrinos. A distant detector (distance in the order of $\sim 100\,\mathrm{km}$) in the direction of the beam can be used to detect appearing electron neutrinos and antineutrinos. The appearance probability of electron neutrinos $P_{\nu_\mu \to \nu_e}$ can be derived considering matter effects to be as follows [Hub07, Ard04]:

$$
\begin{aligned}
P(\nu_\mu \to \nu_e) \simeq &\ \sin^2 (2\vartheta_{13})\ \sin^2 \vartheta_{23}\ \sin^2 \Delta_{31} \\
\pm &\ \alpha\ \sin(2\vartheta_{13})\ \sin\delta\ \cos\vartheta_{13}\ \sin(2\vartheta_{12})\ \sin(2\vartheta_{23})\ \sin^3 \Delta_{31} \\
- &\ \alpha\ \sin(2\vartheta_{13})\ \cos\delta\ \cos\vartheta_{13}\ \sin(2\vartheta_{12})\ \sin(2\vartheta_{23})\ \cos\Delta_{31}\ \sin^2 \Delta_{31} \\
+ &\ \alpha^2\ \cos^2\vartheta_{23}\ \sin^2 (2\vartheta_{12})\ \sin^2 \Delta_{31}
\end{aligned}
\tag{1.8}
$$

where δ is the CP violating phase from equation (1.2), $\alpha \equiv \Delta m_{21}^2 / \Delta m_{31}^2$ and $\Delta_{31} = \Delta m_{31}^2 L/(4E)$. The sign of the second term refers to neutrinos (minus) and antineutrinos (plus). On the one hand one can see in equation (1.8) that with superbeam experiments it is possible to measure ϑ_{13}, δ and Δm_{31}^2 (with its sign, i.e. the mass hierarchy). On the other hand one can also see that superbeam experiments may suffer from parameter correlations and degeneracies caused by different combinations of parameters.

Reactor neutrino experiments:

Complementary to superbeam experiments are reactor neutrino experiments [Ard04]. These experiments are placed in the vicinity of nuclear reactor plants and measure the

electron antineutrino rate and spectrum from the reactor via the inverse beta decay (see equation 2.1 in chapter 2). The relevant oscillation formula (equation (1.7)) was already presented before in section 1.3. The advantage of reactor neutrino experiments is that due to the relatively short baseline in the order of $\sim 1\,\mathrm{km}$ the terms containing $\Delta m_{21}^2 \ll \Delta m_{31}^2$ (the second and the fourth term in equation (1.7)) can be neglected [PDG10]. Thus, the transition probability $P_{\bar{\nu}_e \to \bar{\nu}_e}$ can be approximated as

$$P_{\bar{\nu}_e \to \bar{\nu}_e} \approx 1 - \sin^2\left(2\vartheta_{13}\right)\,\sin^2\left(\frac{\Delta m_{32}^2 L}{4E}\right) \tag{1.9}$$

using $\Delta m_{31}^2 \approx \Delta m_{32}^2$ as an additional approximation. One can see that this kind of experiment provides a direct possibility to measure ϑ_{13} without possible degeneracy effects. The weakness of reactor neutrino experiments up to now is that these experiments suffer from systematic uncertainties, for example due to the uncertainties in the knowledge of the precise neutrino spectrum from the fission products in the reactor fuel. These systematics can be reduced by using two or even more detectors, where one of the detectors is close enough to the neutrino source to measure the neutrino flux without oscillation effects. A second identical detector is placed at a distance to the neutrino source corresponding to the maximal oscillation probability due to Δm_{32}^2. This results in a relative measurement of the electron antineutrino flux and therefore a reduction of the systematic uncertainties. DOUBLE CHOOZ is such a reactor neutrino experiment, which is currently in the final steps of the installation of the first detector.

2 The Double Chooz experiment

2.1 Concept

Figure 2.1: *The Chooz reactor site and the positions of the near and far detector of the* DOUBLE CHOOZ *experiment [Irf10].*

DOUBLE CHOOZ is a reactor neutrino experiment designed to measure the neutrino mixing angle ϑ_{13} at the Chooz nuclear reactor plant in the French Ardennes [Ard04, Ard06] - see figure 2.1. The Chooz reactor plant has two reactor cores with a thermal power of 4.27 GW each.

The new concept of DOUBLE CHOOZ is to use two identical detectors instead of having only one detector: a near detector with an average distance of about 400 m to the reactor cores and a far one at an average distance of 1.05 km[1] [Ard06, Las09]. The near detector will measure the antineutrino flux without or just with a negligible effect of oscillations

---

[1]Here the average distances are quoted as the detectors will have different distances to each reactor core (see figure 2.1).
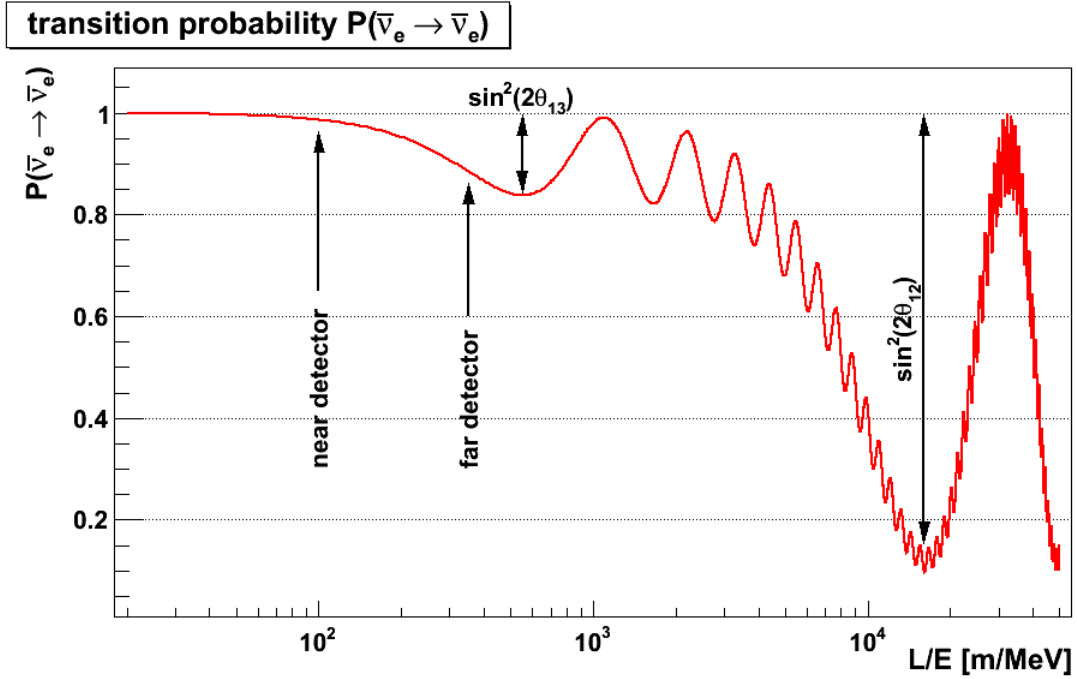
Figure 2.2: *The oscillation probability for electron antineutrinos based on equation (1.7): the survival probability $P_{\bar{\nu}_e \to \bar{\nu}_e}$ is plotted versus L/E on a logarithmic scale (where L is the distance to the source and E the neutrino energy). The plot relies on the following values of the oscillation parameters in equation (1.7): $\Delta m_{21}^2 = 7.59 \cdot 10^{-5} \, eV^2$, $\sin^2(2\vartheta_{12}) = 0.87$, $\Delta m_{31}^2 = 2.30 \cdot 10^{-3} \, eV^2$ (lower bound of the MINOS result) and $\sin^2(2\vartheta_{13}) = 0.16$ (CHOOZ limit with lower bound of the MINOS result). All data were taken from [PDG10]. For the L/E positions of both detectors the average distance to the reactor cores and the maximum energy of the expected neutrino energy spectrum (3 MeV) was used [Ard06].*

due to ϑ_{13}. The mean distance of the far detector to the nuclear reactors is near to the optimum distance regarding the maximal oscillation amplitude $\sin^2(2\vartheta_{13})$ (see equation (1.7) and figure 2.2). Measuring with both detectors has the advantage to minimize the effect of systematic uncertainties concerning for example the knowledge of the cross section of the detection reaction or the uncertainties in the β-spectrum of the fission products in the nuclear fuel. The sensitivity that can be obtained is increased by almost a factor of two compared to measuring with a far detector only (see figure 2.3).

The desired sensitivity of DOUBLE CHOOZ in the case that no oscillation signal can be seen is $\sin^2(2\vartheta_{13}) \leq 0.06$ after 1.5 years of data taking with the far detector only and $\sin^2(2\vartheta_{13}) \leq 0.03$ for additional 3 years with both detectors taking data (both values for $\Delta m_{31}^2 \approx 2.5 \cdot 10^{-3} \, \text{eV}^2$ and a 90 % C.L.) [Ard06]. The time dependency of the sensitivity is shown in figure 2.3. The desired discovery potential after 3 years running both detectors is $\sin^2(2\vartheta_{13}) = 0.05$ (3 σ).
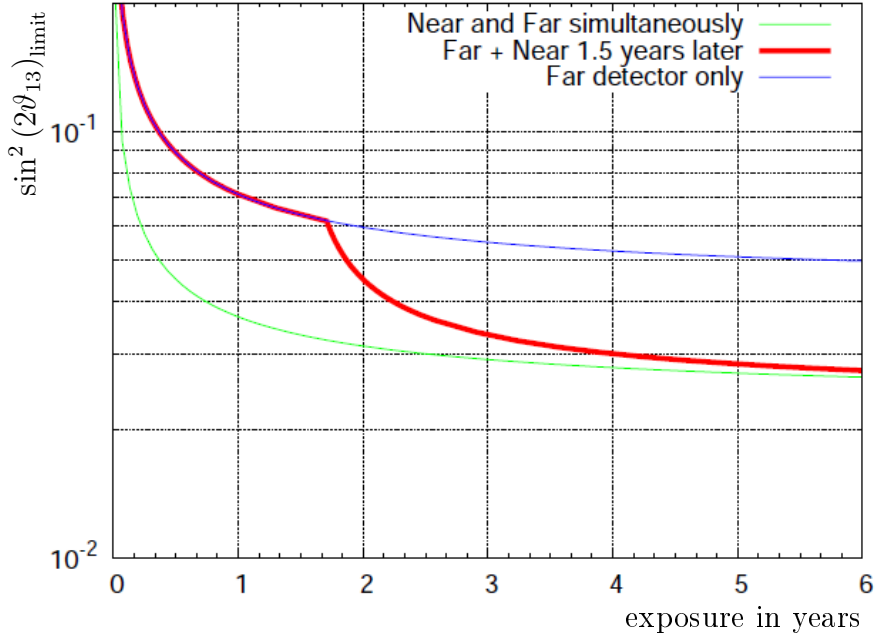
Figure 2.3: *Reachable sensitivity (90 % C.L.) of the DOUBLE CHOOZ experiment (red line): First 1.5 years with the far detector only, then with both detectors, when the near detector is built. The blue curve shows the sensitivity for taking data with the far detector only and the green one for both detectors starting to take data at the same time [Ard06].*

2.2 Signal

As the neutrinos from the nuclear reactor are electron antineutrinos $\bar{\nu}_e$ the detection reaction arising is the inverse beta decay:

$$\bar{\nu}_e + p \longrightarrow e^+ + n \tag{2.1}$$

The energy threshold for this reaction is 1.8 MeV. The created positron leads to a prompt signal as it deposits its kinetic energy in the scintillator and finally annihilates with an electron. This causes two gamma rays with a summed energy of 1.022 MeV, what leads to an energy deposition of at least 1 MeV when both gammas are completely absorbed in the scintillator. The neutron from the inverse beta decay thermalizes after its creation and is then captured with high probability on a gadolinium nucleus (Gd) in the scintillator. The resulting excited gadolinium nucleus deexcites by emitting ~ 3 - 4 gammas with a summed energy of about 8 MeV:

$$Gd + n \longrightarrow Gd^* \longrightarrow Gd + 8\,\text{MeV } \gamma's \tag{2.2}$$

The mean time difference between the prompt annihilation and the delayed neutron capture on Gd is about 30 µs [Lac05, Apo03]. This delayed coincidence provides a possibility to reduce the background sources to those mimicking a delayed coincidence.

The neutrino energy can be determined by measuring the total energy of the positron. Assuming a negligible kinetic energy of the neutron, which is valid for small neutrino energies, the visible energy of the positron signal is

$$E_{vis} \simeq E_{\bar{\nu}_e} - (m_n - m_p - m_e) \simeq E_{\bar{\nu}_e} - 0.8\,\text{MeV} \tag{2.3}$$

This leads directly to the initial neutrino energy $E_{\bar{\nu}_e}$ (m_n is the neutron mass, m_p is the proton mass and m_e is the electron/positron mass).

The neutrino rates without oscillations are expected to be about 69 per day in the far detector and about 480 per day in the near detector.

2.3 Detector design

As already mentioned in the previous section there will be a far and a near detector. The far detector will be in an averaged distance of 1.05 km to the reactor cores with an overburden of about 300 m.w.e. [Ard06]. The cave for the near detector will be built in an average distance to the reactor cores of about 400 m and an overburden of about 115 m.w.e. [Las09].

Both detectors will be of cylindrical shape with four inner detector parts and the outer veto (see figure 2.4):

- **Target:** The target is the innermost volume with a diameter of 2.3 m and a height of ~ 2.5 m. It is an acrylic vessel filled with 10.3 m^3 of gadolinium doped scintillator with a gadolinium concentration of 0.1 %. The gadolinium has a huge neutron capture cross section and is needed to increase the efficiency of detecting the neutron from the detection reaction (see equations (2.1) and (2.2)). This will be the sensitive volume for the detection of the reactor-$\bar{\nu}_e$ [Ard06].

- **Gamma catcher:** The gamma catcher is also an acrylic vessel filled with 22.6 m^3 of liquid scintillator and has a diameter of ~ 3.4 m and a height of ~ 3.6 m. This volume surrounds the target almost completely and is needed to increase the efficiency to detect the gammas from the positron annihilation and the neutron capture as the gammas travel a larger distance in the scintillator [Ard06].

- **Buffer:** The Buffer is a steel vessel filled with 114.2 m^3 of a non-scintillating liquid and has a diameter of ~ 5.5 m and a height of ~ 5.7 m. Hence, the thickness of this volume is about 1 m. This part of the detector houses the 390 inner detector PMTs (photomultiplier tubes). The buffer volume acts as a passive shielding against the background due to radioisotopes in the PMTs, the PMT support structure and also the buffer vessel [Ard06].

- **Inner veto:** The inner veto (IV) is a ~ 50 cm thick volume filled with liquid scintillator and acts as a veto against cosmic muons and fast neutrons produced by those muons (for the near detector the thickness can be higher due to the higher muon flux). The fast neutrons are the cause for using a liquid scintillator
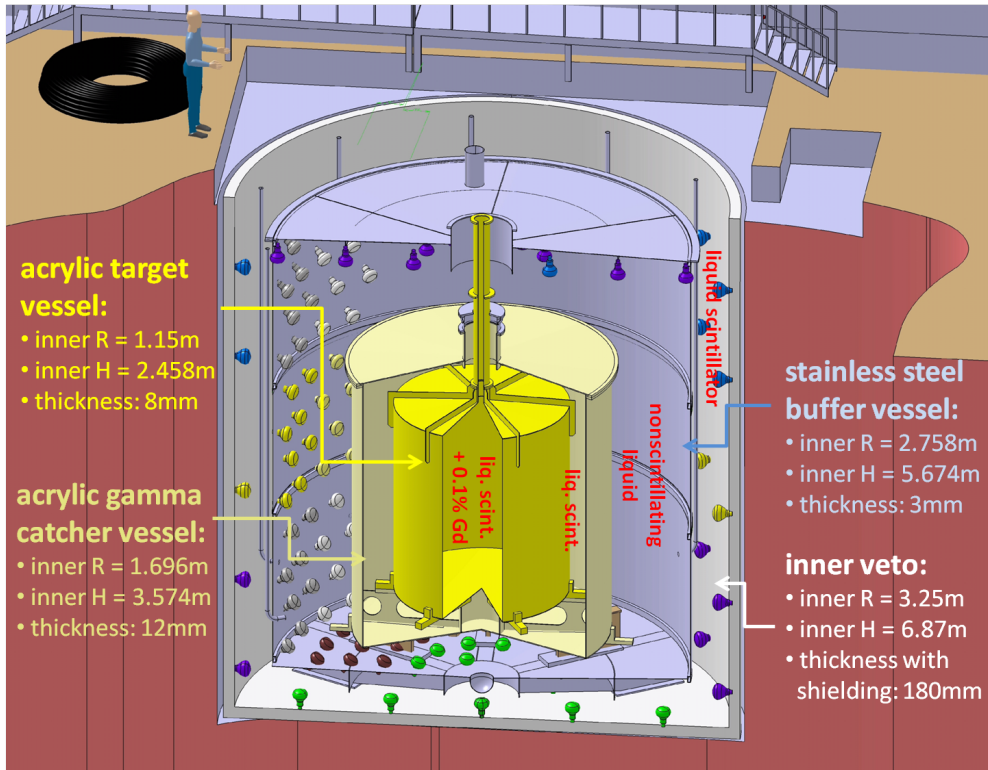
Figure 2.4: *Design of the DOUBLE CHOOZ detectors: the inner part of the detectors will consist of four volumes: the inner veto, the buffer, the gamma catcher and the neutrino target. The target, the gamma catcher and the inner veto will be filled with liquid scintillator (the target scintillator will be doped with gadolinium), while the buffer will be filled with a non-scintillating liquid. The outer veto is not depicted in this figure. It will be arranged on top of the detector (picture and data taken from [DC10]).*

instead of a water Cherenkov detector. Using a scintillator the fast neutrons can be detected by protons scattered off. The inner veto also houses 78 PMTs to detect the scintillation light. In section 2.5 the inner veto is introduced in more detail [Ard06].

- **Outer veto:** The outer veto (OV) is another part of the detector with the aim to reject the background due to cosmic muons and will be installed on top of the detector. It will consist of 44 plastic scintillator modules in case of the far detector. The outer veto is designed to have a large efficiency in the detection of muons and to track muons, which are propagating in the direction of the target area, with high accuracy. The OV consists of two layers: the lower layer will have an active area of $6.4 \times 12.8 \, \text{m}^2$ for the far detector and $11 \times 12.8 \, \text{m}^2$ for the near detector (for the near lab the pit will be built big enough, while the pit size constrains the size of the OV for the far lab). A second layer will be installed about $5 \, \text{m}$ above the IV vessel [Blu10].

2.4 Background

Dealing with neutrinos is always strongly correlated with background reduction and understanding. Building the experiment in the underground reduces the background from cosmic muons and their associated background sources. For Double Chooz this background is still quite high for both detectors as both have a relatively small overburden (see section 2.3)[2]. This is compensated by the large statistics of the neutrino signal due to the vicinity to the nuclear reactor plant. Other background sources like singles from radioactive decays in the material the detector is built of can only be reduced by using radiopure materials and to care for a sufficient cleanliness.

For Double Chooz there are two main background sources mimicking neutrino events (delayed coincidence, see section 2.2): the accidental background and the correlated background. The correlated background can be separated into two groups: the background due to β-n decaying cosmogenic isotopes and (fast) neutrons - both are induced by cosmic muons.

2.4.1 Accidental background

Accidental background is mainly caused by gamma rays and electrons from natural radioactivity (mainly isotopes of the thorium and uranium chains, and ^{40}K) of the detector materials. Gamma rays or electrons from these radioactive decays induce a prompt signal (singles) like the positron from the inverse beta decay. A slow neutron (for example induced by a muon), which is captured close by on gadolinium in a time window of $\sim 100\,\mu$s after the single, induces a delayed neutron event. This leads to a delayed coincidence mimicking a neutrino event.

The radioisotopes from the thorium and uranium chains are reduced to only few ones in the energy range of interest: the visible energy due to alpha particles is limited by the quenching effect to be well below the threshold energy of about $1\,$MeV. Furthermore, the energies of the decay electrons are below this threshold for many cases [Ard04].

The accidental background is expected to be about $3\,\%$ of the neutrino signal for the far detector. The contribution of this background can be determined by the measurement of the singles and neutron capture rate or a direct measurement of the accidental rate. Correlated events due to neutrinos and background can be found by searching for a neutron capture event in a certain time window after a positron like event. As the rate of the singles is not correlated with the rate of neutron events the rate of accidentals can be determined by searching for neutron captures in a time window of the same size, but starting the window a certain time after the positron like event. By this method the influence of correlated events on the measurement of the accidental rate is minimal. Knowing the accidental background its contribution to the systematics can be reduced to less then $0.1\,\%$ and thus, this background is not a severe problem [Ard06].

---

[2]Solar neutrino experiments, for example, typically have overburdens in the order of some thousand m.w.e. .

2.4.2 Muon background

Cosmic muons are created in the earth's atmosphere by reactions of the cosmic rays with nuclei of the gas atoms. Muons are one of the most significant background sources for underground experiments. For both DOUBLE CHOOZ detectors the mean muon energy is one order of magnitude lower than in other neutrino experiments like SUPER-KAMIOKANDE or KamLAND. For the far detector the mean muon energy is expected to be about 60 GeV (for the near it will be even lower due to the lower overburden)[Tan06], while the mean muon energy for KamLAND is about 260 GeV [Abe10]. The expected muon rate for the far detector is about 30 Hz for all volumes and about 5 Hz through the target region [Ard06]. Muons induce other background, which may cause correlated events, like fast neutrons and cosmogenic isotopes (see sections 2.4.3 and 2.4.4).

2.4.3 Neutron background

Neutrons in the detector are mainly caused by cosmic muons. Muons can produce neutrons by spallation or muon capture (in case of a negatively charged muon) in the rock or in the detector materials. Some of these neutrons are then captured after the veto time in the target area and may cause a delayed coincidence by scattering off a proton before the capture: the proton scattered off may cause a prompt signal like a positron and the neutron - captured on gadolinium - may cause a delayed signal. [Ard04].

In contrary to the accidental background the systematics of the background due to fast neutrons cannot be reduced significantly, as this background can not be measured efficiently. It may be partly reduced by the detection of correlated events due to fast neutrons (by scattered off protons) in different active volumes of the detector, e.g. a threefold coincidence of an energy deposition in the inner veto, the gamma catcher and the target. For the far detector site a contribution to the neutrino like signal of about 0.3 % (with a rate of $\sim 0.2 \, \mathrm{d}^{-1}$) is expected resulting in an effect on the systematics of 0.2 %. For the near detector the rate of the fast neutrons will be larger, but the neutrino signal will also be larger. This results in an effect on the systematics of the same order as for the far detector [Ard06].

2.4.4 Cosmogenic isotopes background

Cosmogenic isotopes decaying via a β-n cascade are also induced by muons via spallation on ^{12}C directly in the scintillator. The two most relevant isotopes for DOUBLE CHOOZ are ^{8}He and ^{9}Li. The branching ratios of the decay of these isotopes (normalized to 100 %) are shown in figure 2.5. As one can see, both isotopes have relatively high branching ratios to decay by emission of an electron and a neutron - 49.5 % for ^{9}Li and 12 % for ^{8}He - with a total energy well above the DOUBLE CHOOZ threshold of 1 MeV. If one of these isotopes is created by a muon in the target region, the electron may cause a prompt signal like a positron followed by a delayed capture of the neutron on gadolinium, what results in a neutrino-like event. The half-lives of both isotopes are rather large with 119 ms for ^{8}He and 178 ms for ^{9}Li, respectively. There is no chance to reduce this background by a
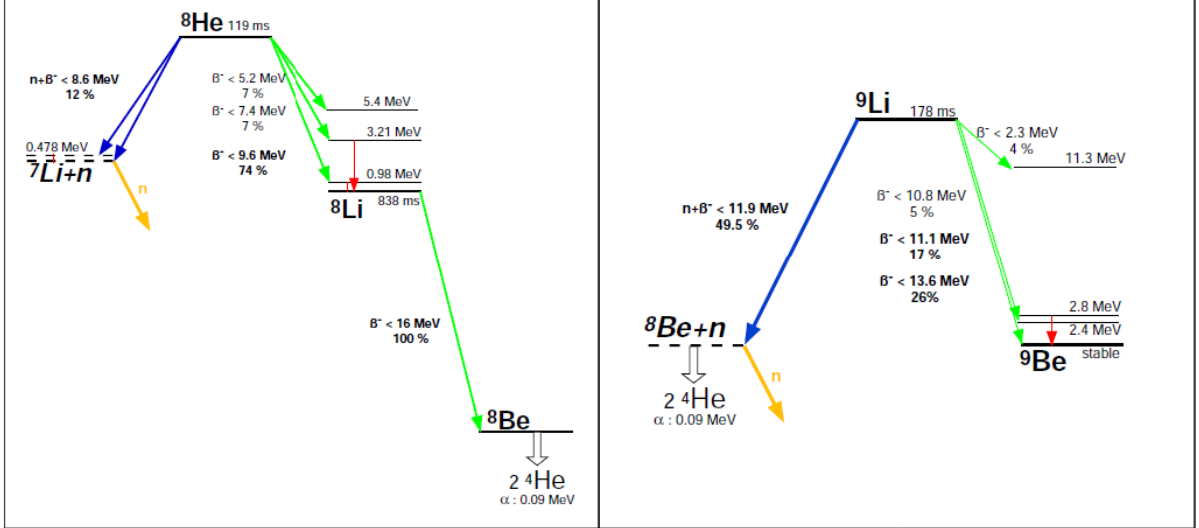
Figure 2.5: *The schemes show the relevant branching ratios for the decays of ^8He (left) and ^9Li (right). The branching ratios of the different decay modes and half-lives are shown. Of special interest for* Double Chooz *are the branching ratios of the decays depicted by the blue arrows: these decays cause an emission of an electron and a neutron. Such a decay in the target may cause a delayed coincidence mimicking a neutrino event [Ard04].*

detector dead time of some half-lives after a muon event, because the expected rate for muons is about 30 Hz for the whole far detector [Ard04]. The result would be a detector dead time exceeding 100 % by far.

Furthermore, the cross sections of the production of ^{8}He and ^{9}Li were only measured for relatively high energies up to now: in [Hag00] a measurement of the production cross sections of different cosmogenic isotopes in liquid scintillators is presented. The cross section for the ^{8}He- and ^{9}Li-production were only measured for a muon energy of 190 GeV, which is one order of magnitude larger than the mean muon energy for Double Chooz. In addition, only a combined production cross section for ^{8}He- and ^{9}Li could be measured[3] to be $\sigma(^8He +^9 Li) = (2.12 \pm 0.35)$ μbarn. With this value a prediction for the rate for the KamLAND experiment could be given to be 0.24 ± 0.05 counts/(d $\cdot$ 100 t). This is consistent with the measurement by KamLAND of 0.38 ± 0.07 counts/(d·100 t) [Abe10]. With this rate it is possible to estimate a rate for the Double Chooz far detector using the following equation 2.4 for the ratio of the rates for KamLAND $R_{KL}(^8$He $+^9$ Li) and Double Chooz $R_{DC}(^8$He $+^9$ Li) [Hag00]:

$$\frac{R_{DC}(^8\text{He} +^9 \text{Li})}{R_{KL}(^8\text{He} +^9 \text{Li})} = \left(\frac{\langle E_\mu^{DC}\rangle}{\langle E_\mu^{KL}\rangle}\right)^{0.75} \frac{\Phi_\mu^{DC}}{\Phi_\mu^{KL}} \tag{2.4}$$

---

[3]This is caused by the half-lives, which are too close to each other to be distinguished by a fit to the data.

parameter	value	taken from
$\langle E_\mu^{DC} \rangle$	$(60.6 \pm 0.4)\,\text{GeV}$	[Tan06]
$\langle E_\mu^{KL} \rangle$	$(260 \pm 8)\,\text{GeV}$	[Abe10]
$\Phi_\mu^{DC}(\text{sim})$	$2.2 \cdot 10^3\,\text{m}^{-2}\text{h}^{-1}$	[Ard06]
$\Phi_\mu^{DC}(\text{CHOOZ})$	$1.4 \cdot 10^3\,\text{m}^{-2}\text{h}^{-1}$	[Apo03]
Φ_μ^{KL}	$(5.37 \pm 0.41)\,\text{m}^{-2}\text{h}^{-1}$	[Abe10]
$R_{KL}(^8\text{He} +^9\text{Li})$	$(0.38 \pm 0.07)\,\text{d}^{-1}(100\,\text{t})^{-1}$	[Abe10]

Table 2.1: *The parameters used to estimate the rate of ^8He and ^9Li at the DOUBLE CHOOZ far detector: $\langle E_\mu^{DC} \rangle$ and $\langle E_\mu^{KL} \rangle$ are the mean muon energies for DOUBLE CHOOZ and KAMLAND and Φ_μ^{DC} and Φ_μ^{KL} the muon fluxes. For the DOUBLE CHOOZ muon fluxes the value from a simulation $\Phi_\mu^{DC}(\text{sim})$ and the value measured by the first CHOOZ experiment $\Phi_\mu^{DC}(\text{CHOOZ})$ were used. $R_{KL}(^8He +^9Li)$ is the rate of ^8He and ^9Li measured by the KAMLAND experiment.*

where $\langle E_\mu^{DC} \rangle$ and $\langle E_\mu^{KL} \rangle$ are the mean muon energies for DOUBLE CHOOZ and KAMLAND, and Φ_μ^{DC} and Φ_μ^{KL} the muon fluxes. The used values are summarized in table 2.1. In addition, the concentration of ^{12}C for KAMLAND and DOUBLE CHOOZ was approximated to be the same. In [Hag00] the energy dependence of the production cross section is assumed to be a power law: $\sigma(E_\mu) \propto E_\mu^\alpha$. The exponent 0.75 was chosen as this value is in good agreement with the exponents α measured for other isotopes produced by muons in a liquid scintillator.

With the DOUBLE CHOOZ target volume of $10.3\,\text{m}^3$ the rate of ^{8}He and ^{9}Li in the target can be estimated to be

$$R_{DC,target}^{sim}(^8\text{He} +^9\text{Li}) \approx 4.4\,\text{d}^{-1}$$

for the muon flux at the far detector site determined by the simulation and

$$R_{DC,target}^{\text{CHOOZ}}(^8\text{He} +^9\text{Li}) \approx 2.8\,\text{d}^{-1}$$

using the muon flux measured by the first CHOOZ experiment, which was performed at the DOUBLE CHOOZ far site.

The rate of the background due to ^{8}He and ^{9}Li at the far detector could also be estimated by an analysis of the data from the first CHOOZ experiment [Ard06]. For the CHOOZ experiment the best fit result for the ^{9}Li rate is $0.7 \pm 0.2\,\text{d}^{-1}$. With this an estimation for the DOUBLE CHOOZ far site can be made resulting in a rate of $1.4\pm0.5\,\text{d}^{-1}$. As one can see this value is smaller than the rates estimated from the results of the KAMLAND experiment with a mean muon energy, which is one order of magnitude larger than for the DOUBLE CHOOZ far site. The discrepancy between the two estimations may

be explained by a deviation of the energy dependence from the power law for smaller muon energies.

The rate estimated from the Chooz data corresponds to a contribution of about 2 % to the neutrino-like signal [Ard06]. The effect on the systematics is about 1 %, which is quite high. For the near detector the rate of this kind of background will be significantly higher, but the contribution to the neutrino-like signal smaller, what results in a smaller effect on the systematics than for the far detector [Ard06].

2.5 The inner veto

As already mentioned before the inner veto is filled with liquid scintillator and houses 78 PMTs (old PMTs from IMB and Super-Kamiokande - Hamamatsu R1408 [Zbi08]). The PMTs are arranged in five rings distributed in three areas (see figures 2.6, 2.7 and 2.8):

- **Top (PMTs 390-413):** At the top of the veto 24 PMTs are arranged in two rings - an outer and an inner ring with 12 PMTs each. The outer ring PMTs are alternatingly watching downwards and inwards, while the inner ring PMTs are alternatingly watching inwards and outwards.

- **Side wall (PMTs 414 to 425):** At the side wall at half the hight of the detector 12 PMTs are installed watching upwards and downwards.

- **Bottom (PMTs 426 to 467):** The bottom inner veto houses 42 PMTs also arranged in two rings. The bottom part of the inner veto also contains the buffer feet, what effects the arrangement of the PMTs in this part of the inner veto. The outer ring consists of 24 PMTs alternatingly watching upwards and inwards, while 6 of the 12 inwards watching PMTs face a buffer foot. The inner ring consists of 18 PMTs arranged in 6 groups of 3 PMTs between each buffer foot. Each triplet consists of one inwards watching and two outwards watching PMTs.

The inner veto has a diameter of 6.5 m and a height of almost 7 m. It has a thickness of about 50 cm at the side and the bottom and about 60 cm at the top. To increase the light collection efficiency in the inner veto the inner surface of the veto tank is painted with TiO_2-based white paint, which is diffusely reflecting. Furthermore, the buffer tank side wall is coated with a reflective VM2000 foil.

The inner veto has a weakness. As one can see in figures 2.4 and 2.6 the single detector parts will be accessible via a chimney. The chimney in the inner veto is made of stainless steel, so it is absolutely opaque for the scintillation light. Therefore, vertical muons can reach the target and gamma catcher region without making any signal in the top part of inner veto. This is particularly problematic when these muons have a low energy and are stopped in the inner part of the detector, as these even do not make any signal at the bottom of the inner veto. This problem will be solved when the outer veto is installed as the upper layer will cover the area above the chimney.
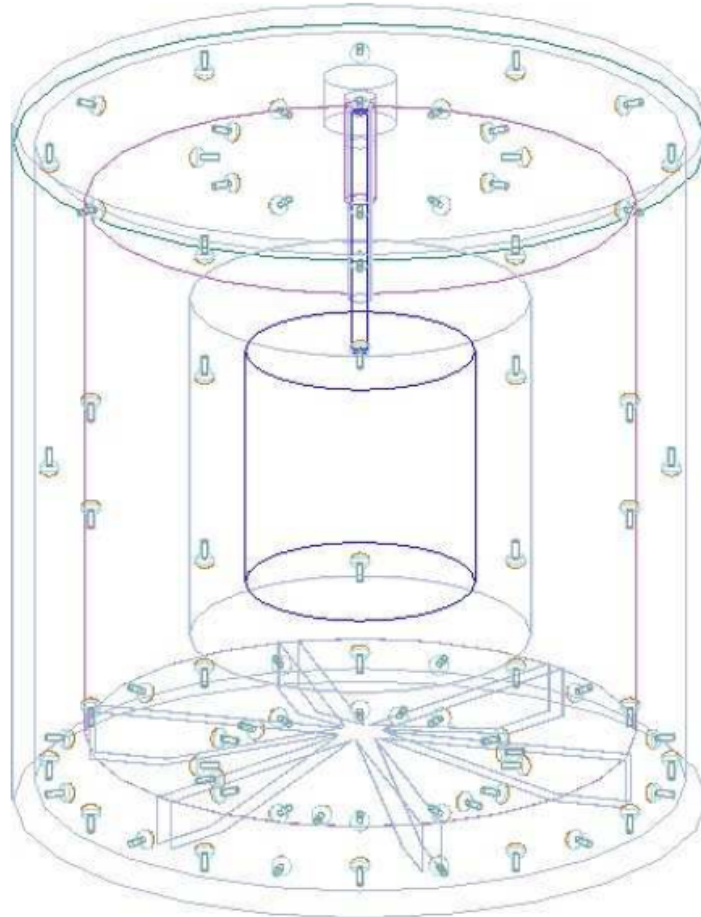
Figure 2.6: *The* DOUBLE CHOOZ *inner veto design: the position of the PMTs and their viewing directions in the inner veto are shown. The cylindric contours indicate the different inner detector volumes as presented in section 2.3. In the lower part of the picture one can see the six buffer feet [Ard06].*
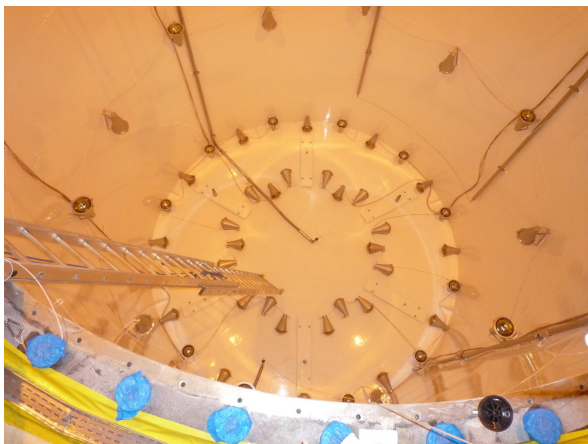
(a) The inner veto before the installation of the buffer vessel
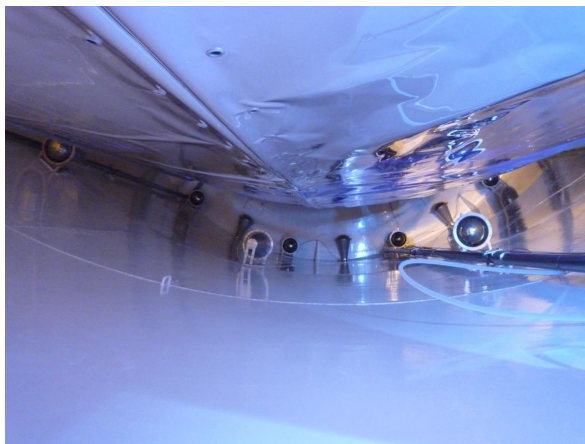
(b) The view from the top along the inner veto side wall to the bottom

(c) Installed PMTs at the bottom of the inner veto

(d) Installed PMTs at the bottom of the inner veto

Figure 2.7: *Photographs of the inner veto before (a) and after (b),(c),(d) the installation of the buffer vessel. On picture (b) one can see the VM2000 foil the buffer vessel is coated with (upper part) and on pictures (c) and (d) one can see a buffer foot in the back with a PMT facing this foot. Pictures taken from [Irf10].*
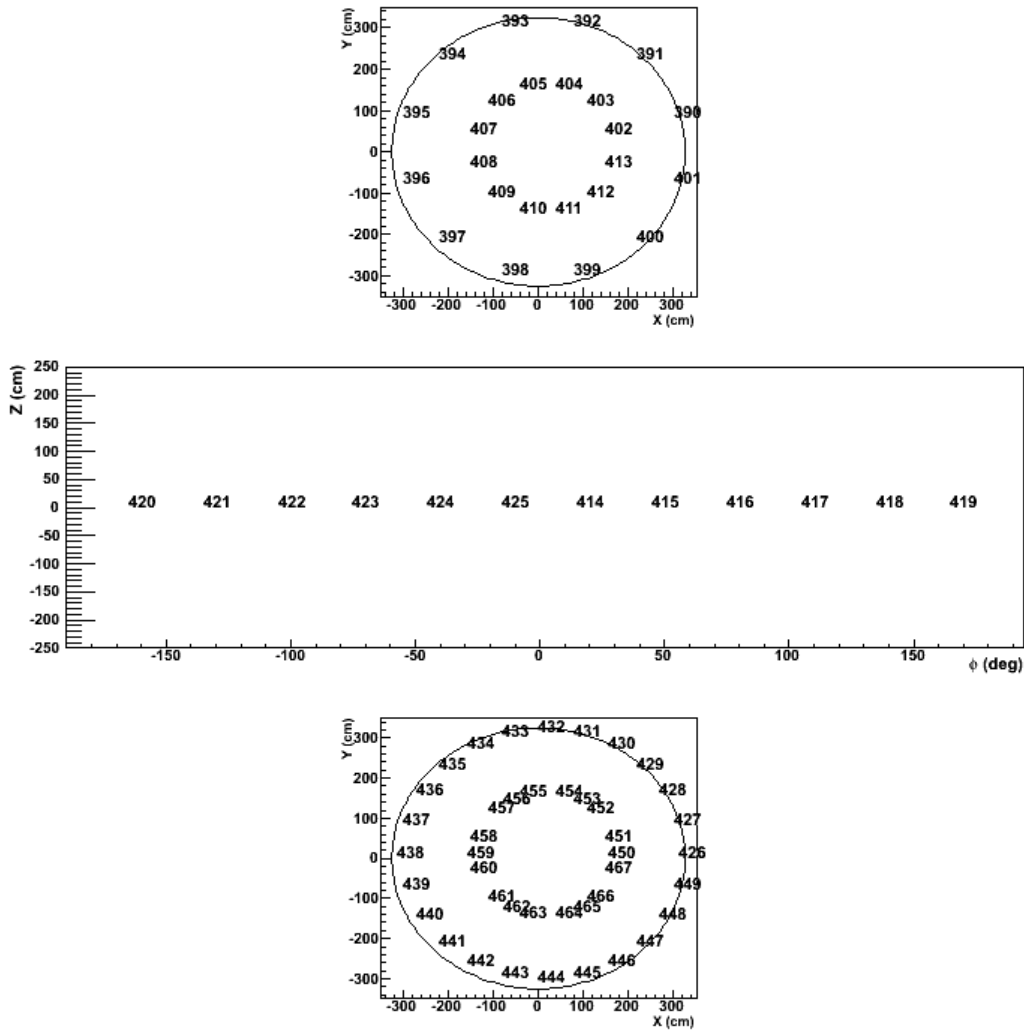
Figure 2.8: *The coordinates of the PMTs in the inner veto for each of the three areas: the upper plot shows the positions of the top PMTs (in the X-Y-plane at $Z \approx 3.2\,m$), the plot in the middle the positions of the side wall PMTs (polar angle ϕ and height Z for an radius $R \approx 3\,m$) and the lower plot the positions of the bottom PMTs (in the X-Y-plane at $Z \approx -3.2\,m$). The numbers shown are the PMT numbers. The numbering of the inner veto PMTs starts at 390 as the inner detector PMTs are numbered from 0 to 389 [Gre10].*

3 Motivation for a muon tracking in Double Chooz

As already mentioned in section 2.4 there are several background sources affecting the sensitivity of the measurement of $\sin^2(2\vartheta_{13})$. The background sources with the most significant effect are induced by cosmic muons - the cosmogenic β-n emitters ^{8}He and ^{9}Li, and fast neutrons. Therefore, muons provide information on the processes, rates and profiles for those background sources.

The main purpose of a muon track reconstruction is to derive the information where the muon has crossed the detector from all the single PMT hits. This information then can be used for different studies concerning backgrounds, detector performance or the muons themselves, e.g. the angular distribution of the muons. A track reconstruction may be used to select a sample of muons from all data, which contains only muons with special characteristics, e.g. vertical muons or muons which have passed not the inner detector region, but only the buffer.

As mentioned in section 2.4.4 the problem of the background due to ^{8}He and ^{9}Li are the relatively long half-lives of these isotopes combined with the large muon rate at both DOUBLE CHOOZ detector sites. Thus, one cannot apply a veto time window of some half-lives after each muon to cut those background events. A good track reconstruction may give a possibility to apply cuts for some half-lives on the volume around a muon track to partly reject this kind of background. In [Hag00] the lateral production profile of isotopes produced by muons in a liquid scintillator (basically reactions on ^{12}C) was measured. In figure 3.1 one can see the production profile for ^{11}C, which is assumed to be similar to that for ^{8}He and ^{9}Li. The measured production profile has the following distribution

$$\Phi(r) = \frac{1}{166}e^{-0.0403r^2} + \frac{1}{1223}e^{-0.098r} \tag{3.1}$$

where r is the lateral distance to the muon beam axis (in cm). The distribution $\Phi(r)$ is normalized to $\int_0^\infty \Phi(r)2\pi r\, dr = 1$. Therefore, $\Phi(r)$ describes the probability that an isotope is produced at a given distance r perpendicular to the muon track.

The DOUBLE CHOOZ target has a volume of $V_{target} \approx 10\,\text{m}^3$ with an height of $H_{target} \approx 2.5\,\text{m}$ and a radius of $R_{target} \approx 1.15\,\text{m}$. A cylindrical cut around a muon track with radius $r_{cut} = 0.3\,\text{m}$ (see figure (3.2)) would lead to a volume V_{cut} of

$$V_{cut} \approx \pi r_{cut}^2 \cdot H_{target} \approx 0.7\,\text{m}^3, \tag{3.2}$$

i.e. a vertical muon track fully contained in the target. A muon flying diagonally through the target would lead to a maximum volume cut of $V_{cut} \sim 1\,\text{m}^3$. Muons can
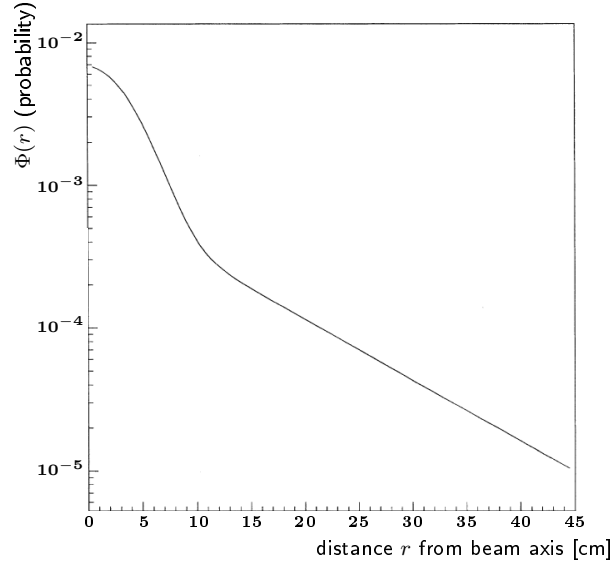
Figure 3.1: *The lateral activation profile $\Phi(r)$ for ^{11}C produced by cosmic muons in a liquid scintillator (from measurements presented in [Hag00]). $\Phi(r)$ describes the probability that an isotope is produced at a given distance r perpendicular to the muon track.*

also propagate through a small part of the target leading to a smaller volume than given in equation (3.2). As the muon rate throughout the target is expected to be 5 Hz [Ard06] one can estimate the dead target volume to be $3.5 \, \text{m}^3$ for a veto time of 1 s (for maximal dead volume: tracks such that volume cuts do not overlap). After 1 s only 0.3% of the ^{8}He (half-life of 119 ns) and 2.0 % of the ^{9}Li (half-life of 178 ms) remain. The veto time of 1 s corresponds to an almost permanent veto applied on $\lesssim 1/3$ of the target volume and therefore reduces the detected neutrinos by the same factor. A volume cut with $r_{cut} = 0.2 \, \text{m}$ would lead to $V_{cut} \sim 0.3 \, \text{m}^3$ resulting in an almost permanent cut volume of $\sim 1.6 \, \text{m}^3$ (about 15 % of the target volume). The values chosen for r_{cut} are quite realistic as r_{cut} should be at least as large as the error of the reconstruction.

In table 3.1 estimations for different r_{cut} and a veto time of 1 s are shown. The table shows also the effect on the efficiency of the cut, i.e. the fraction of cosmogenic isotopes that can be rejected by a cut with the corresponding value of r_{cut}. The values for the cut efficiency were estimated using equation (3.1) (integration from 0 to r_{cut}). Furthermore, the remaining ^{8}He and ^{9}Li after a veto time of 1 s were taken into account. As expected the efficiency decreases with decreasing r_{cut}, but a volume cut with $r_{cut} = 0.3 \, \text{m}$ already causes a rejection of the correlated events due to cosmogenics of about 76 %.

Another possibility would be to use a muon track reconstruction to measure the profile of ^{8}He and ^{9}Li produced by the muons. This is in principle the same as above, but the other way around: searching for a neutrino like event in the vicinity of a muon track. Obviously one needs a precise muon track reconstruction to do this. Furthermore, a good spatial resolution for the prompt positron-like events is mandatory to measure the lateral distance to the muon track from where ^{8}He or ^{9}Li were produced.
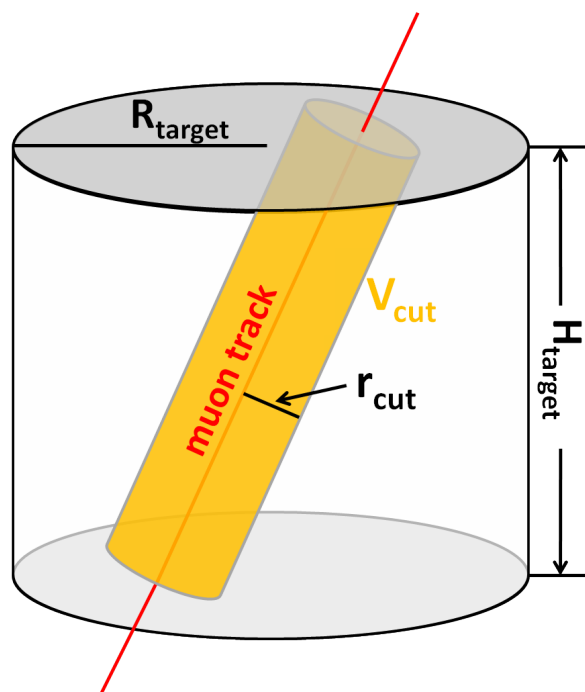
Figure 3.2: *Illustration of a volume cut around a muon track: H_{target} is the height of the target, R_{target} is the radius of the target and r_{cut} is the radius of the cylindrical volume cut.*

r_{cut} [m]	V_{cut} [m^3]	$\sum V_{cut} \approx 5 \cdot V_{cut}$ [m^3]	$\sum V_{cut}/V_{target}$	cut efficiency
0.5	~ 2.0	~ 10	$\sim 100\,\%$	$\sim 96\,\%$
0.4	~ 1.3	~ 6.5	$\sim 65\,\%$	$\sim 93\,\%$
0.3	~ 0.7	~ 3.5	$\sim 35\,\%$	$\sim 87\,\%$
0.2	~ 0.3	~ 1.5	$\sim 15\,\%$	$\sim 76\,\%$
0.1	~ 0.08	~ 0.4	$\sim 2\,\%$	$\sim 57\,\%$

Table 3.1: *Estimations of the detector dead volume for different radii r_{cut} of cylindrical volume cuts around muon tracks in the target. The volume cuts may be used to reject the correlated background due to ^8He and ^9Li. All values are just rough estimates. $\sum V_{cut} \approx 5 \cdot V_{cut}$ is the almost permanently dead target volume (for a veto time of $1\,s$), where the factor 5 corresponds to the muon rate of $5\,Hz$ in the target and the pessimistic approximation that the track volume cuts do not overlap. $\sum V_{cut}/V_{target}$ is the fraction of the dead volume in the target, where $V_{target} \approx 10\,m^3$ was used. The cut efficiency denotes an estimation of the fraction of cosmogenic isotopes that can be rejected by the corresponding volume cut around the muon track according to the production profile $\Phi(r)$ (see equation (3.1) and figure 3.1). For the estimated efficiency values the remaining ^8He and ^9Li after a veto time of $1\,s$ were taken into account: after $1\,s$ about $99.7\,\%$ of the ^8He and $98.0\,\%$ of the ^9Li have decayed.*

4 Simulation of muons

4.1 The DOGS framework

DOGS (Double Chooz Offline Group Software) is the C++ based simulation and analysis framework for Double Chooz. It relies on the data analysis framework ROOT [Roo10] and the particle simulation toolkit Geant4 [Ago03, Gea10]. The main packages used to simulate and analyse the data needed for the studies on a muon track reconstruction with the inner veto are **DCGLG4sim**, **RoSS**, **RecoPulse** and **DCAna template**, which shall be explained in more detail in the following.

4.1.1 DCGLG4sim

DCGLG4sim (Double Chooz Generic LAND Geant4 simulation) is the Geant4 based detailed simulation of the Double Chooz detector and is based on the simulation of the KamLAND experiment [Ard06].

Geant4 is a C++ based toolkit to simulate physical processes for an user-defined detector geometry. The particles and physical processes to be known by the simulation have to be defined in the so-called physics list. The physics list of DCGLG4sim contains in principle all physical processes that may be interesting for the experiment including scintillation and an optical model for the PMTs (for more details see section 4.2.1). Geant4 needs an user-defined primary particle as an input for each event to be simulated: the user has to specify the kind of particle, its energy, primary vertex position and momentum direction. Geant4 then propagates the primary particle and the created secondaries stepwise (all steps of a particle form a track). The length of the steps depends on the geometry and on the physical processes defined in the physics list. Geant4 tracks all particles until they have either been stopped in detector or have left all volumes of the simulation.

All the general simulation data generated by DCGLG4sim are stored eventwise in a ROOT-tree called *GlobalThInfoTree* [1]. Data concerning particle and tracking information of the simulated particles are stored in the *ParticleThInfoTree* and the *TrackThInfoTree* [2]. These ROOT-trees provide the possibility to have a look into the true information on the processes of interest.

---

[1] The abbreviation *Th* in the names of the ROOT-trees stands for *truth* denoting that this tree contains simulated data.

[2] The particle and tracking data is not saved by default by DCGLG4sim. For the simulation of vertical muons (see section 4.3) this data has not been stored, what has an effect on the calculations concerning the true muon track (see section 5.2).

4.1.2 RoSS

RoSS (Readout System Simulation) is a DOGS package that relies on the data simulated with DCGLG4sim. It simulates the response of the readout system of the detector to the simulated physical events, i.e. the PMT response to a photoelectron created at the photocathode and all following electronics - including all uncertainties like noise from the electronics or the time jitters of the PMTs (see section 4.2.2 for values implemented concerning the inner veto PMTs). The simulated data is stored in a ROOT-tree called *PulseThInfoTree*.

4.1.3 RecoPulse

RecoPulse is a package that finds and characterizes pulses from the raw data. The raw data can either be real data from the detector or simulation data processed through RoSS. All data concerning the reconstructed PMT pulses, like pulse start/maximum/end times and reconstructed pulse charges are saved to a ROOT-tree called *PulseInfoTree* [Nov09].

4.1.4 DCAna template

The DCAna template is a tool that creates a C++ class with an user-defined name. It provides an infrastructure to access the data in the different InfoTrees (like the ones mentioned above) and to analyse this data with self-written code. If needed one can define a new InfoTree to store the analysis results.

4.2 General simulation settings

Several simulation runs have been used to determine the performances of the muon track reconstruction methods. They were performed within the DOGS framework and basically with the packages described in section 4.1. The DOGS version used for all simulations and analysis was the Prod-06-01[3] (with Geant4 version 4.9.2.p01). The simulations of the muons were done with DCGLG4sim and processed through RoSS and RecoPulse to have data, where the influence of the electronic readout chain is fully taken into account. All simulations were performed at the IN2P3 Computing Centre (CCin2p3) located at Lyon (France) [CC10], especially to handle the huge number of simulated muons needed for the maximum likelihood reconstruction (see chapter 7).

4.2.1 DCGLG4sim

For all muon simulations DCGLG4sim was used with all available muon physics applied, i.e. multiple scattering, bremsstrahlung, ionization, pair production, capture at rest (in case of μ^-) and muon decay. Hadronic processes activated together with the Cherenkov

---

[3]Prod-06-01 is the internal version code of DOGS.

process or scintillation caused errors. Therefore, hadronic processes were omitted for all muon simulations - resulting in a slight speedup of the simulation. As hadronic processes[4] were not needed for the studies on a muon track reconstruction (see chapters 6 and 7) omitting these does not introduce errors. Scintillation and the Cherenkov effect were activated as these processes are necessary to have optical photons causing PMT signals.

Muon simulations are consuming a lot of computing time as muons produce very much light in the scintillator. The muon tracking algorithms presented in this thesis exclusively use the inner veto PMT signals. Therefore, the production of light in the target or the gamma catcher is not needed for testing these reconstructions. DCGLG4sim uses files as an input for the data concerning the detector geometry and the properties of the different detector materials. The properties of the scintillators and the buffer liquid are stored in a file, which contains the composition of the liquids, the concentrations of the single components, and the scintillation properties, in particular the scintillation light yield, which is set to 8500 photons per MeV for the inner veto scintillator [Gre10]. To increase the speed of the simulation some modifications were made regarding the target and gamma catcher liquids:

- The components of these liquids were set to non-scintillating oil only (in both cases dodecane). This was done to prevent scintillation in the inner detector parts as DCGLG4sim knows dodecane as non-scintillating. The concentrations (handled as volume fractions) were also set to one for the corresponding components.

- The scintillation light yields were set to 0 for target and gamma catcher.

These modifications increased the speed of the simulation by a factor of about 2 - 3.

4.2.2 RoSS and RecoPulse

RoSS and RecoPulse were used with the default ROOT-macros *'runRoSS.C'* and *'runRecoPulse.C'* and the default settings.

At this point some characteristics concerning PMTs, especially the timing of a PMT, are of interest. The timing is basically affected by the so-called *transit time spread* (TTS). The *transit time spread* (also called jitter) is the transit time fluctuation observed, when identical light pulses strike the same part of the photocathode of a PMT, i.e. the fluctuation in the time between the generation of the electron in the photocathode and the onset of the anode pulse. This is in principle the timing resolution of a PMT and therefore has a significant influence on the precision of a reconstruction using the timing information of the PMTs [Pho02].

Also *prepulses* have an influence on the timing of PMTs. Prepulses are, as the name implies, pulses preceding the normal pulse and are caused by photons passing the photocathode without interactions and producing a photoelectron on the surface of either the first dynode or the focusing electrodes. Therefore, these pulses should precede the

---

[4]For example spallation by muons is regarded as a hadronic process in Geant4. Therefore, the simulated data cannot be used for studies concerning the production of fast neutrons or cosmogenic isotopes (see section 2.4).

normal pulses by roughly the travel time of the photoelectron from the photocathode to the first dynode [Lub00]. This may affect a reconstruction as the prepulses cause earlier start times of the PMTs.

The *dark noise rate* of a PMT, i.e. the rate of pulses due to electrons from the photocathode, which are not produced by an incident photon (for example by thermal emission), also has an effect on the timing information [Pho02]. The dark pulses mimic a PMT hit and thus may affect the reconstruction of a muon track.

The corresponding values implemented in RoSS to simulate the pulses of the inner veto PMTs are as follows:

- **transit time spread (TTS)**: $2\,\text{ns}$ $(1\,\sigma)$

- **prepulses**:
    - probability: $3\,\%$
    - t_{pp}: $-20\,\text{ns}$
    - Δt_{pp}: $1\,\text{ns}$

- **dark noise rate**: $2\,\text{kHz}$

were t_{pp} is the mean time of the prepulses and Δt_{pp} the fluctuation of t_{pp}. These implemented values are quite realistic as indicated by measurements regarding the real inner veto PMTs (Hamamatsu R1408) [Jil96, Zbi08].

With these values for the prepulses and the dark pulse rate it is possible to estimate their influence on a possible track reconstruction. The mean number of PMTs per muon event in the inner veto experiencing a prepulse can be approximated to be $n_{pp} \approx 0.03 \cdot 78 = 2.34$ in case that all 78 IV PMTs are hit during a muon event (0.03 is the probability for a prepulse per PMT). As the side wall PMTs are not used in the current versions of both reconstruction methods the maximal number of used PMTs is 66 corresponding to a mean number of PMTs seeing a prepulse of about $n_{pp} \approx 2$.

The influence of dark noise ($2\,\text{kHz}$ per PMT) can be approximated with a characteristic time of a muon event of about $50\,\text{ns}$ considering the propagation time of the photons in the scintillator after their generation by the muon (see more details in section 5.1). This leads to an estimation of the probability for a dark pulse in a muon event of $2\,\text{kHz} \cdot 50\,\text{ns} \cdot 66 = 0.66\%$ in case that all 66 top and bottom inner veto PMTs contribute to a reconstruction. So this probability is very small an thus can be neglected. The dark noise pulses can also be rejected by applying a threshold on the PMT charges of more than one photoelectron (pe) as the dark noise pulses mimic single photoelectron pulses.

4.3 Vertical muons

Vertical muons are defined by a momentum direction $\hat{p} = (0, 0, -1)$ and were simulated for the reason of understanding muon events and the behaviour of the reconstruction without additional effects appearing for inclined muons.

The vertical muons (μ^+ and μ^-) are injected with a randomly chosen primary vertex on a circle area at $z = 4000\,\text{mm}$ (which is above the whole detector; the center of the target is at $(0, 0, 0)\,\text{mm}$) and with radius of $r = 3250\,\text{mm}$ (the radius of the inner veto).
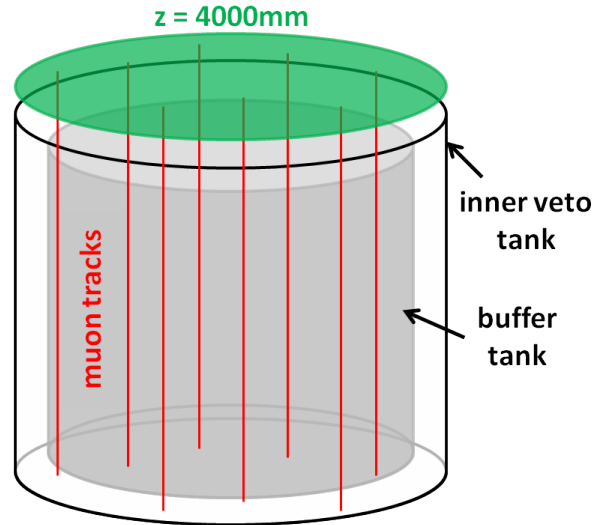
Figure 4.1: *Simulation of vertical muons: a primary vertex is generated randomly on a circle area at $z = 4000$ mm and with radius $r = 3250$ mm (green circle). The momentum direction of the muons (red) is $\hat{p} = (0, 0, -1)$.*

A total of 300 000 vertical muons were simulated with an energy of 100 GeV. 280 000 muons are intended to be used for the calibration of the maximum likelihood track reconstruction (see chapter 7). The remaining 20 000 muons are used to study the performance of the reconstruction methods. The energy of 100 GeV was chosen so that the muons have sufficient energy to pass the whole detector and are not significantly deflected due to scattering (see section 5.2 and figure 5.6).

4.4 Inclined muons

Inclined muons, i.e. muons with an inclination with respect to the z-axis, were simulated in the following way (see figure 4.2): a pair of random points is generated, where one point $\vec{x}_1$ is on a circle area at $z_1 = 3500\,\text{mm}$ (above the detector) and the other point $\vec{x}_2$ on a circle area at $z_2 = -3500\,\text{mm}$ (below the detector). Both circles have a radius of $r = 3250\,\text{mm}$. $\vec{x}_1$ is used for the primary vertex and the momentum direction $\hat{p}$ is calculated from both points as follows:

$$\hat{p} = \frac{\vec{x}_2 - \vec{x}_1}{|\vec{x}_2 - \vec{x}_1|} \tag{4.1}$$

The cause of simulating inclined muons of this kind is that all muons enter the detector through the top lid and leave it through the bottom (when the energy is large enough
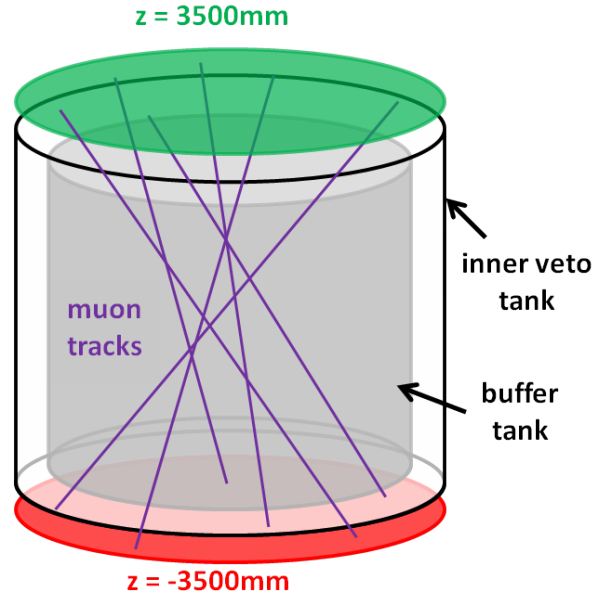
Figure 4.2: *Simulation of inclined muons: two random points on circle areas at $z = 3500\,mm$ (green) and $z = -3500\,mm$ (red) are chosen. The momentum direction of the muons (violet) is calculated from both points (see equation (4.1)) and the point on the upper circle area is used as primary vertex. Such inclined muons were simulated for an energy of $100\,GeV$ and for a momentum range from $100\,MeV/c$ to $5\,GeV/c$.*

that the muons are not stopped or decay inside the detector). It was intended that no muon enters or leaves the detector through the side wall, because the reconstruction of those muons is more difficult due to the geometric PMT arrangement in the inner veto. For this reason the algorithms explained later in this thesis (see chapters 6 and 7) are not able to reconstruct those muons properly - especially the maximum likelihood method.

Inclined muons were simulated with different energies: for $100\,\text{GeV}$ and for a primary momentum range from $100\,\text{MeV/c}$ to $5\,\text{GeV/c}$[5]. In sum, $550\,000$ monoenergetic $100\,\text{GeV}$ muons were simulated: $500\,000$ used for the calibration of the maximum likelihood method and $50\,000$ to be reconstructed by the different algorithms. Again, as for the vertical muons the energy of $100\,\text{GeV}$ was chosen to simulate muons that pass the whole detector and are not significantly deflected by scattering.

For the momentum range ($100\,\text{MeV/c}$ to $5\,\text{GeV/c}$) in sum $650\,000$ inclined muons were simulated: again $500\,000$ are used for the calibration of the maximum likelihood method and $150\,000$ are used to test the reconstruction performance. The momentum range from $100\,\text{MeV/c}$ to $5\,\text{GeV/c}$ was chosen to study the behaviour of the reconstruction algorithms for smaller muon energies.

---

[5]This momentum range corresponds to muon energies from about $145\,\text{MeV}$ to $5\,\text{GeV}$.

5 Muons in the inner veto

5.1 Principle characterization of a muon event in the inner veto

As mentioned before in chapter 4 all simulated data was processed through RoSS and RecoPulse to have muon data looking similar to the real data, i.e. data from the detector. All further analysis will always rely on the timing and charge information of the PMTs (reconstructed by RecoPulse from the raw data from the detector). The timing is the time information of the single PMT pulses: the pulse start time, the pulse maximum time and the pulse end time (in the order of ns). The charge of a PMT pulse is the area under the pulse and is given either in units of pe (photoelectrons) or DUQ (digital units of charge). Figure 5.1 shows a PMT pulse (schematic) with the different pulse times and the charge. The data actually used are:

- the pulse start time in ns ('*fTstart*' in '*PulseInfoTree*')

- the total PMT charge in pe ('*fQPE*' in '*PulseInfoTree*')

The pulse start times are available with a 2 ns accuracy only as this is the ADC sampling rate [Aki08, Nov09]. RecoPulse provides different algorithms to reconstruct the pulse start time. For all data used in this thesis the algorithm relying on a current threshold was used: the pulse start time is defined to be the time when the pulse exceeds a certain threshold above the pedestal [Nov09]. The threshold value actually used was the default value, which is set to be five standard deviations above the pedestal (where standard deviation means the width of the pedestal).

The PMT charge may not always contain the proper information about the muon track as especially the PMTs close to the track see very much light causing saturation of the PMT pulse[1]. This effect is included in RoSS. Therefore, the charge of such a pulse may not be reconstructed properly by RecoPulse.

5.1.1 A vertical muon in the inner veto

In figure 5.2 the pulse start times (figure 5.2a) and charges in pe (figure 5.2b) of the hit inner veto PMTs are depicted for a typical event, where the vertical lines separate the different PMT rings (see figures 2.6 and 2.8). The muon used for these plots has a

---

[1]Muons produce very much light in a scintillator. The energy loss of muons with energies between 100 MeV and 1 TeV in matter due to ionization can be approximated to be $\sim 2 \cdot \rho$ MeV/cm, where ρ is the density of the material [Leo94, PDG10].
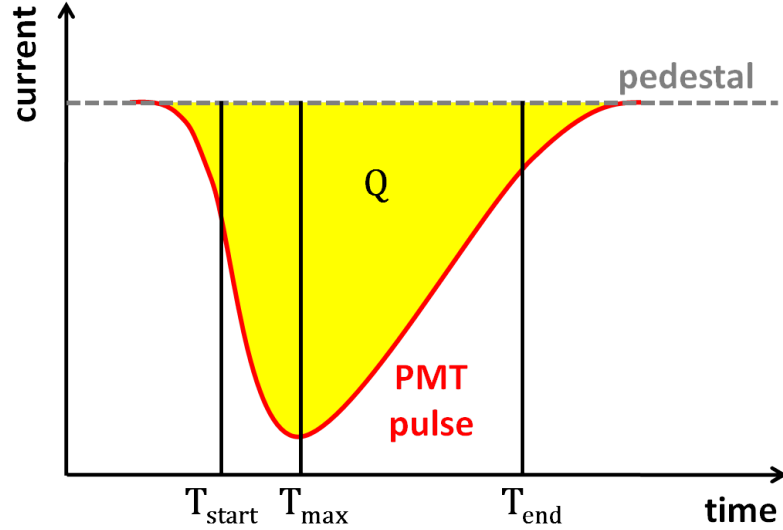
Figure 5.1: *A schematic PMT pulse: the pedestal is depicted with the grey dashed line and the red curve denotes the PMT pulse. The charge Q is depicted as the yellow area under the pulse. The pulse start (T_{start}), maximum (T_{max}) and end time (T_{end}) are illustrated by vertical lines. T_{start} is defined by the time the pulse exceeds a current threshold of $5\,\sigma$ above the pedestal and T_{end} is defined by the time the pulse amplitude falls below $20\,\%$ of the maximum value.*

kinetic energy of $100\,\text{GeV}$ and passes the inner veto vertically along the side wall with $x = -3000\,\text{mm}$ and $y = -10\,\text{mm}$. Hence, it crosses the inner veto only. This event was chosen as it nicely demonstrates the evolution of PMT hits in the inner veto.

The muon enters the detector through the top. Therefore, the PMTs at the top inner veto are hit first. The top outer ring PMTs are hit slightly earlier than the PMTs from the inner ring, as the muons passes closer to the outer ring. One also can see the time evolution in each ring, what results in a shape looking like a "V" in the case of this muon (caused by the geometric positions of the PMTs). The PMTs of the side wall ring are hit next and then finally the bottom PMTs are hit. For the bottom the outer ring again is hit slightly earlier than the inner ring.

Comparing figure 5.2a and figure 5.2b one can see that the earlier a PMT is hit the larger the charge is. This is caused by the fact that the scintillation light is emitted isotropically what leads to a decreasing intensity of the photons with increasing distance to the muon track.

5.1.2 An inclined muon in the inner veto

Figure 5.3 shows the start time (figure 5.3a) and charge (figure 5.3b) evolution for an inclined $100\,\text{GeV}$ muon crossing the whole detector diagonally entering the inner veto at $x = -2705\,\text{mm}$ and $y = 235\,\text{mm}$ and leaving it at $x = 2659\,\text{mm}$ and $y = 915\,\text{mm}$.
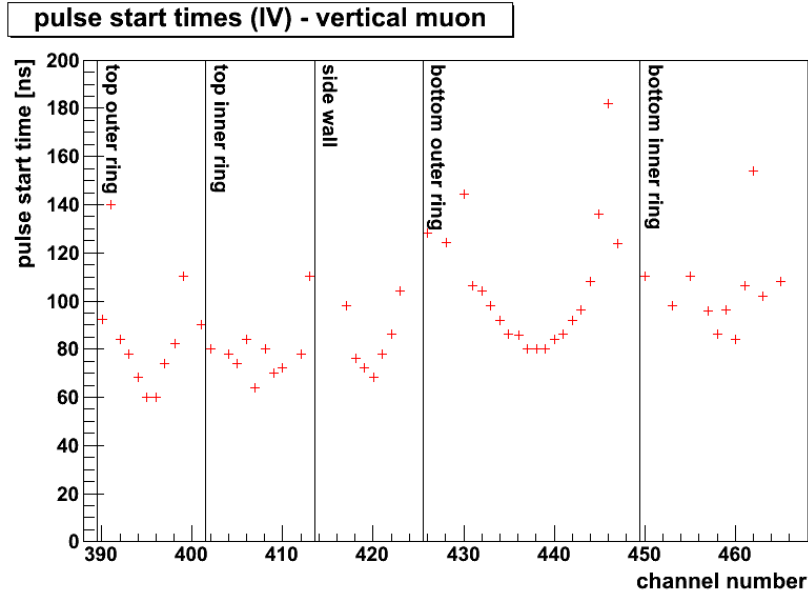
(a)
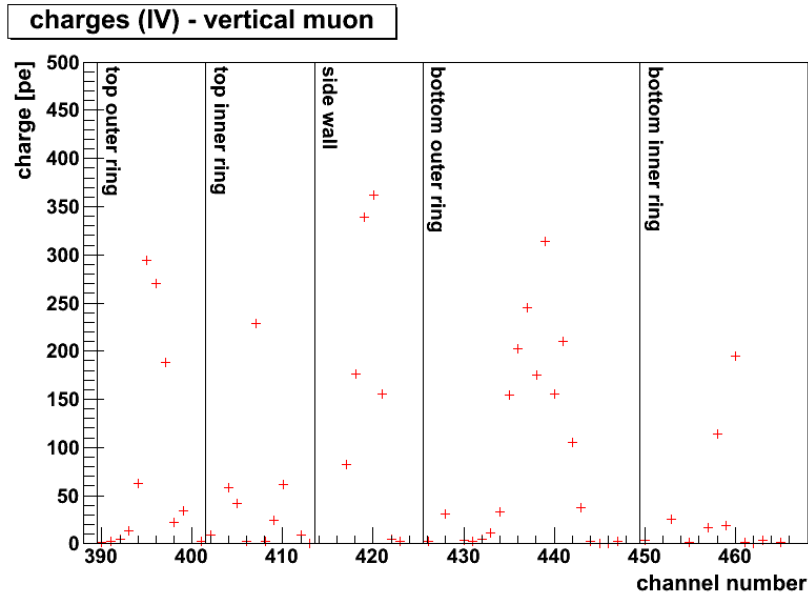
(b)

Figure 5.2: *The pulse start times (a) and charges in pe (b) of the IV PMTs for the same vertical 100 GeV muon. The horizontal lines separate the different PMT rings (see figure 2.8). This muon was chosen as it crosses the inner veto vertically along the side wall at $(x, y) = (-3000, -10)$ mm. Hence, it demonstrates the time evolution of the event in the inner veto. The closer to the muon track a PMT is the earlier is its start time. One can see that early hit PMTs have large charges, while the PMTs, which are hit later, have relatively small charges.*

(a)

(b)
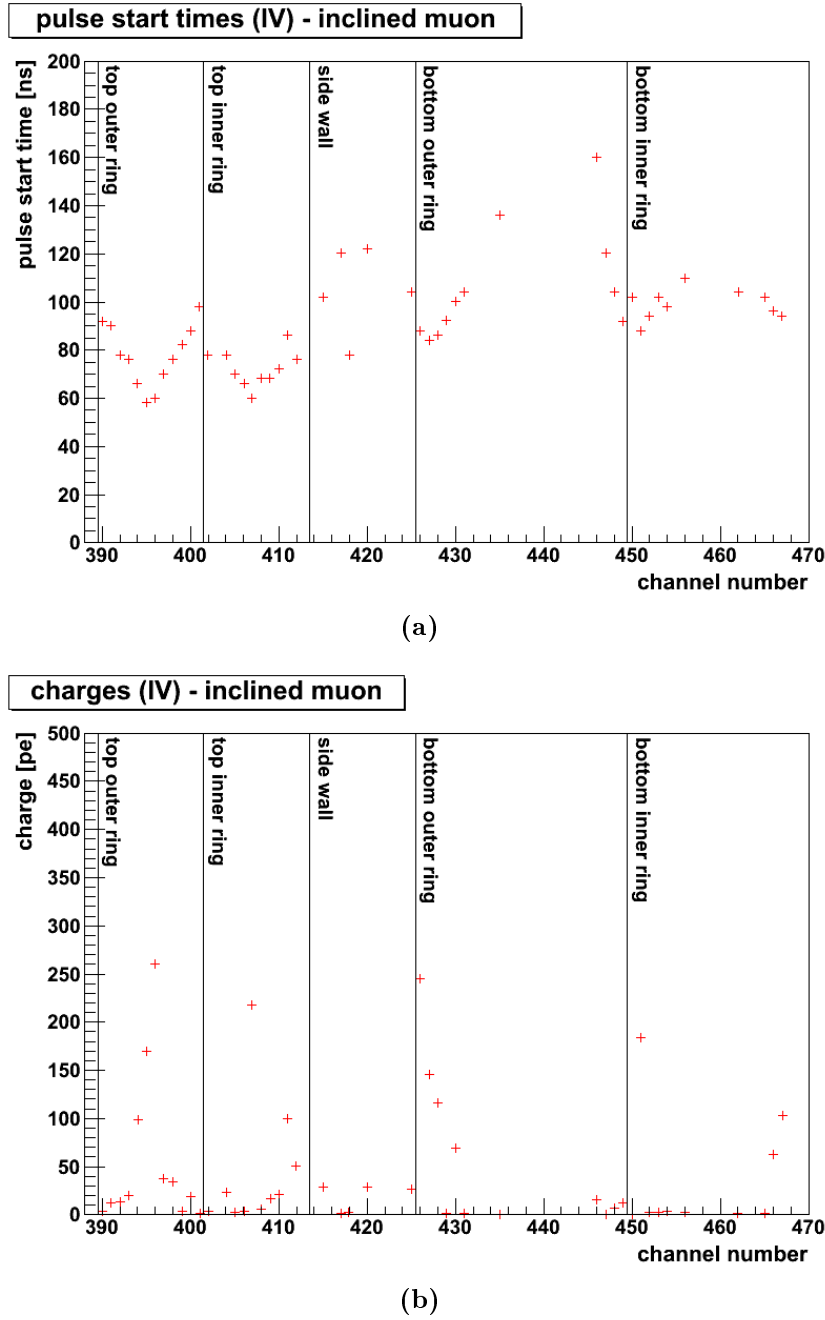
Figure 5.3: *The pulse start times (a) and charges in pe (b) of the IV PMTs for the same inclined 100 GeV muon. The horizontal lines separate the different PMT rings (see figure 2.8). The muon crossed the inner veto almost diagonally - it enters the inner veto at $x = -2705$ mm and $y = 235$ mm and leaves it at $x = 2659$ mm and $y = 915$ mm. The closer to the muon track a PMT is the earlier is its start time. One can see that early hit PMTs have large charges, while the PMTs, which were hit later, have relatively small charges. This does not apply to the side wall PMT hits as these hits are caused by light produced at the top part of the inner veto.*

Regarding figure 5.3a the time evolution for this muon can be seen. Again the top PMTs are hit first as the muon enters the inner veto at the top. The side wall PMTs are hit before the bottom PMTs. As the muon crosses the whole detector diagonally these hits cannot be due to light produced in the vicinity of these PMTs. The photons causing the side wall PMT hits are created by scintillation at the top inner veto. The structure of the hits at the bottom shows that the muon leaves the inner veto on the opposite side as it has entered the veto at the top.

In figure 5.3b one can see again that the early hits have larger charges. For the side wall PMTs this can not be observed. As mentioned above this can be explained by the fact that the light seen by the side wall PMTs is light from the top part of the veto and hence, the distance to the creation point is large.

5.1.3 Characteristic times

To characterize a muon event in the inner veto it is of interest to estimate characteristic times in the inner veto, like the time scintillation light needs to travel from the top of the inner veto to the bottom or from one edge to the other. These times then have to be compared with characteristic times of a muon in the inner veto.

The characteristic times of the light in the scintillator depend on the refractive index n of the scintillator. The simulation uses values between 1.59 (for 200 nm) and 1.43 (for 800 nm) for the inner veto scintillator (these are preliminary values as the true values still have to be measured) [Gre10]. To estimate the characteristic times in the following an average value of $n_{IV} = 1.5$ will be used for the refractive index. With this value the resulting value for the speed of light in the scintillator is $c_{IV} = c_{vac}/n_{IV} = 2/3 \cdot c_{vac} \approx 2 \cdot 10^8 \, \mathrm{m\,s^{-1}}$.

In contrary to photons the velocity of the muons in the scintillator can be approximated to be $v_\mu \approx c_{vac}$ for muons with energies large compared to their rest mass $m_\mu \approx 106 \, \mathrm{MeV/c^2}$ [PDG10]. With a mean muon energy of $\sim 60 \, \mathrm{GeV}$ at the DOUBLE CHOOZ far detector site this is a good approximation for the majority of the muons.

In figure 5.4 the dimensions of the inner veto are depicted. The interesting parameters are the height $H_{IV} = 6.87 \, \mathrm{m}$, the radius $R_{IV} = 3.25 \, \mathrm{m}$ and the diagonal $D_{IV} = 9.64 \, \mathrm{m}$.

With these parameters and the speed of the photons and muons it is possible to estimate the characteristic times. The time the light needs to travel a distance of H_{IV}, i.e. from the top to the bottom and vice versa, can be estimated to be

$$t_\gamma(H_{IV}) \approx 34 \, \mathrm{ns} \tag{5.1}$$

The time the muon needs to travel this distance can be estimated to be

$$t_\mu(H_{IV}) \approx 23 \, \mathrm{ns} \tag{5.2}$$

and the time the muons needs for the diagonal distance D_{IV} is

$$t_\mu(D_{IV}) \approx 32 \, \mathrm{ns} \tag{5.3}$$
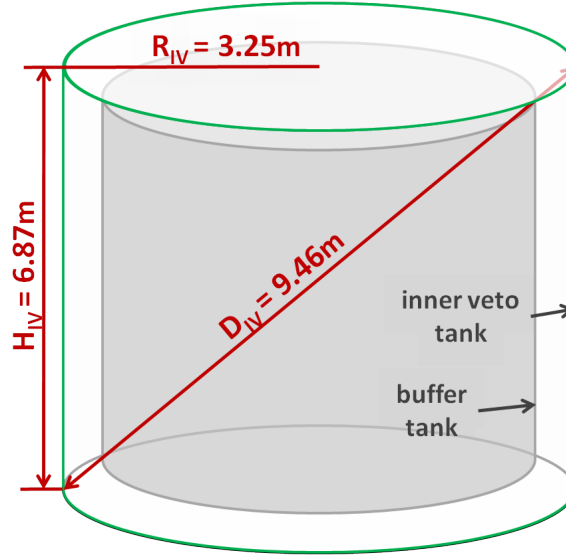
Figure 5.4: *The dimensions of the inner veto: R_{IV} is the inner radius of the IV tank, H_{IV} is the height of the IV and D_{IV} its diagonal. The dimensions are used to estimate characteristic times in the inner veto.*

As the light can not take the shorter way through the inner detector the corresponding time for the light can be estimated to be the time the light needs to travel the complete height H_{IV} in addition to the distance $2R_{IV}$ from one edge of the detector to the other. The time corresponding to $2R_{IV}$ regarding the photons can be estimated to be

$$t_\gamma(2R_{IV}) \approx 32\,\text{ns} \tag{5.4}$$

Hence, the time corresponding to $t_\mu(D_{IV})$ is

$$t_\gamma(2R_{IV}) + t_\gamma(H_{IV}) \approx 66\,\text{ns} \tag{5.5}$$

Comparing these estimated times one can see, that it is a good approximation to take the first PMT hits as hits due to direct light from the muon, i.e. light, which is not reflected. The value of $t_\gamma(2R_{IV}) \approx 32\,\text{ns}$ is of interest as this time limits the hits that can be used in one area (top or bottom) to those in a time window of maximal 32 ns after the first hit. All hits, which appear later are most likely due to reflected light.

5.2 The true muon track

Speaking about the true muon track means the track of the muon in the simulation. The true muon track is useful to check the performance of the reconstruction algorithms. Both reconstruction methods described in this theses rely on the reconstruction of an inner veto entry and exit point. There are two approaches to calculate the true entry and exit points from the simulation data depending on the data which is available: one approach considers multiple scattering of the muons and the other one uses the approximation

that the deflection by multiple scattering can be neglected. A comparison between both will be given in section 5.2.2.

5.2.1 Calculations without tracking information

If there is no tracking data (i.e. no *TrackInfoTree*; see section 4.1) available, the true entry and exit points are calculated using the approximation that the muon is hardly deflected by multiple scattering. That means that the muon track can be approximated to be a straight line defined by the primary vertex position and the primary momentum direction. The true entry points are determined by the intersection of this straight line with the x-y-plane at $\bar{z}_{top} = 3178.75\,\text{mm}$ and the true exit points by the intersection with the x-y-plane at $\bar{z}_{bottom} = -3170\,\text{mm}$, where $\bar{z}_{top}$ and $\bar{z}_{bottom}$ are the mean PMT z-positions for the top and the bottom inner veto.

These planes are used as the z-coordinates of the entry and exit points reconstructed by the barycenter method are very close to these mean PMT z-positions (the barycenter is a weighted average of the PMT positions; see section 6). The maximum likelihood method actually reconstructs the x-y-coordinates of the entry and exit points only. In this case the z-coordinates are fixed to be the mean PMT z-positions.

5.2.2 Calculations with tracking information

If the track information is available the true inner veto entry and exit point are determined in the following way: as already mentioned in section 4.1 a track in GEANT4 consists of different steps at which the particle interactions take place. This true entry and exit point calculation relies on the two steps which are the closest to the x-y-planes at $\bar{z}_{top}$ and $\bar{z}_{bottom}$, where one of the steps is above $(\vec{x}_1)$ and the other beneath $(\vec{x}_2)$ the corresponding plane (see figure 5.5).

The true entry points are determined by the intersection of the line defined by the two steps belonging to the x-y-plane at $\bar{z}_{top} = 3178.75\,\text{mm}$ and the true exit points analogously using the two steps corresponding to the x-y-plane at $\bar{z}_{bottom} = -3170\,\text{mm}$. In case that the muon track ends before the top or the bottom x-y-plane the algorithm cannot determine the corresponding $\vec{x}_2$. If the muon is stopped before the top x-y-plane, but has entered the inner veto, the true entry point is determined as described in section 5.2.1 and if the muon reaches the bottom inner veto, but not the bottom x-y-plane, the true exit point is calculated to be the intersection of the line defined by the last two steps of the muon track with the plane at $\bar{z}_{bottom}$.

5.2.3 Comparison between both calculations

As the true entry and exit points are determined using the approximation of negligible deflection, if the tracking information is not available (see section 5.2.1), the question arising is whether this is a good approximation. Figure 5.6 shows the distance between the determined exit points from both calculations in the x-y-plane, i.e. the calculations with the approximation of negligible deflection and the calculations using the tracking
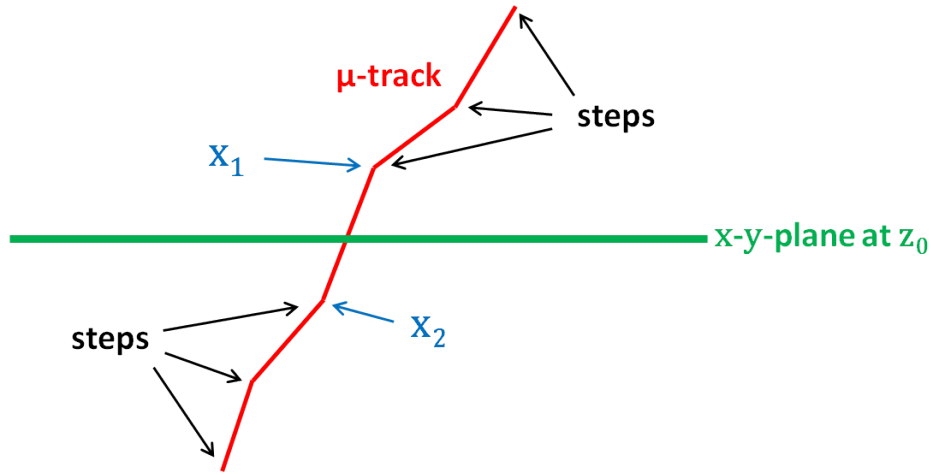
Figure 5.5: *To calculate the true entry and exit point using the tracking data from the simulation the two steps $\vec{x}_1$ and $\vec{x}_2$ closest to the corresponding x-y-plane at z_0 are determined ($z_0 = \bar{z}_{top}$ for the entry point and $z_0 = \bar{z}_{bottom}$ for the exit point).*

information. The plot was produced with $50\,000$ inclined muons with an energy of $100\,\mathrm{GeV}$ as described in section 4.4. As one can see the deviation from the true track is smaller than $10\,\mathrm{mm}$ for almost all cases with a mean value of about $3\,\mathrm{mm}$. Both reconstructions presented later in this thesis show a precision, which is at least one order of magnitude larger than this mean value. Therefore, the approximation of a negligible deflection of the muons is good enough to be used for the simulated vertical $100\,\mathrm{GeV}$ muons, for which the tracking information is not available. Vertical muons have to cover a smaller distance between the entry and the exit point. Therefore, the distribution for vertical muons is expected to be even more narrow.
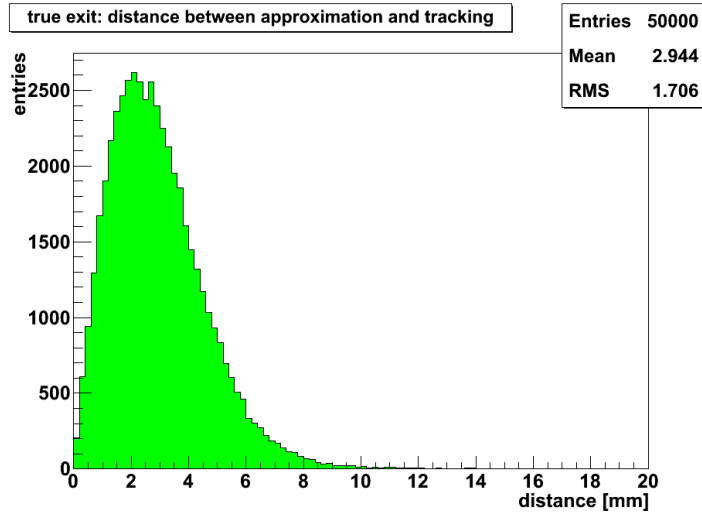
Figure 5.6: *The distance between the true entry point calculated with the approximation of negligible deflection of the muons (see section 5.2.1) and the true entry point calculated using the tracking information (see section 5.2.2). The plot was produced with the data of 50 000 inclined 100 GeV muons simulated as described in section 4.4. The mean deviation from the true muon track of about 3 mm is small compared to the precision of the reconstruction algorithms presented in this theses (see chapters 6 and 7), what makes the approximation of negligible deflection of the muons good enough to be used for the simulated 100 GeV vertical muons (here the tracking information is not available).*

6 Barycenter method

The barycenter approach for a muon track reconstruction with the inner veto was inspired by the muon tracking with the muon veto of BOREXINO [Wur09]. The reconstruction is based on the DCAna template (see section 4.1) and uses the pulse start times and charges in pe of the hit PMTs.

6.1 The basic equations

This method relies on the calculation of a barycenter of the hit PMTs using a weight factor for each hit, which depends on the charge and the timing. The reconstruction is based on the determination of an inner veto entry point $\vec{x}_{entry}$ and an inner veto exit point $\vec{x}_{exit}$. The entry point is determined from the top PMTs (PMTs 390 to 413) and the exit point from the bottom PMTs (PMTs 426 to 467). From these two points the reconstructed momentum direction $\hat{p}_{rec}$ can be derived as follows:

$$\hat{p}_{rec} = \frac{\vec{x}_{exit} - \vec{x}_{entry}}{|\vec{x}_{exit} - \vec{x}_{entry}|} \tag{6.1}$$

The entry and the exit point are reconstructed using the pulse information from all hit PMTs, where only the earliest pulse for each PMT is taken into account - in case there are several pulses per PMT. This is realized by a barycenter formula:

$$\vec{R}_{bc} = \frac{\sum_i w_i \cdot \vec{r}_{PMT,i}}{\sum_i w_i} \tag{6.2}$$

where the sum includes all contributing hits i (see section 6.2 for the criteria of the hit selection). $\vec{R}_{bc}$ is the coordinate of the reconstructed point, $\vec{r}_{PMT,i}$ are the positions of the hit PMTs i, and w_i the weight factors. The formula for the w_i is based on the weightings used for the BOREXINO muon tracking [Wur09]:

$$w_i = (q_{pe,i})^m \cdot \exp\left[-\left(\frac{t_{s,i} - t_{s,min}}{t_{window}}\right)^n\right] \tag{6.3}$$

where $q_{pe,i}$ is the charge in pe of the hit PMT i, $t_{s,i}$ the pulse start time of hit i and $t_{s,min}$ the start time minimum of the hits for the top (entry point) or the bottom (exit point). t_{window} is a time window after the first hit in which all contributing hits have to be. The two exponents m and n can be varied to find the weighting with the best reconstruction performance.

For the PMT coordinates $\vec{r}_{PMT,i}$ in the barycenter formula (6.2) the centers of mass of the PMTs photocathodes are used as these can be seen as the effective photocathode

positions. These coordinates are also used for the maximum likelihood reconstruction later (see chapter 7).

As figures 5.2 and 5.3 imply the weights should be chosen in a way that hits with early start times and huge charges are emphasized. The weightings quoted in equation (6.3) satisfy this condition: the charge factor $(q_{pe,i})^m$ emphasizes larger charges and earlier start times are emphasized by the exponential function as this function decreases with increasing $t_{s,i}$. Figure 6.1 shows the behaviour of the timing term in equation (6.3) for n between 1 and 3.
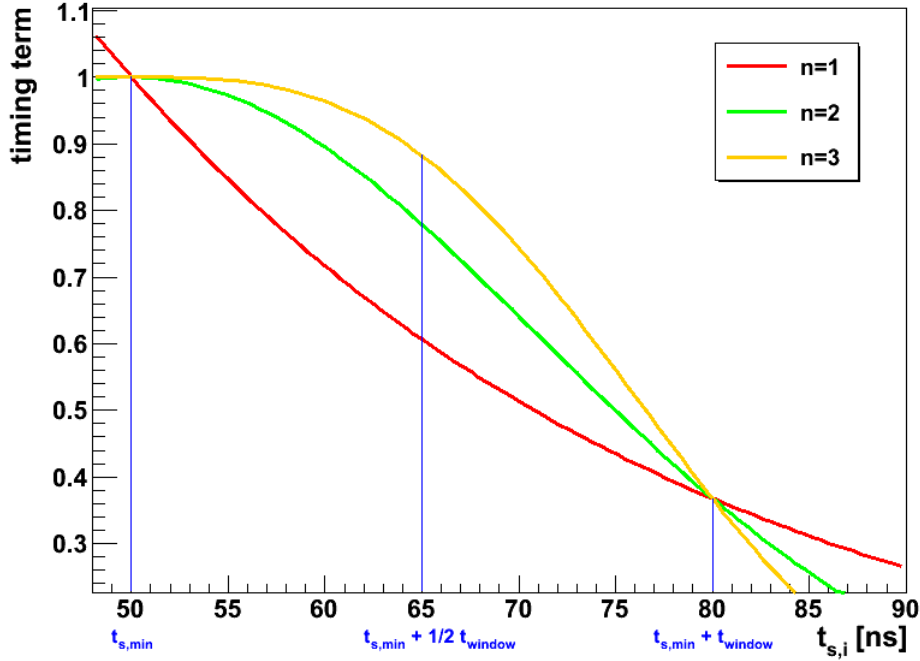
Figure 6.1: *Behaviour of the timing term in equation (6.3) and n between 1 and 3 (for $t_{s,min} = 50\,ns$ and $t_{window} = 30\,ns$).*

As one can see a increasing exponent n causes that the early hits are more and more weighted equally, while the emphasis on later hits decreases stronger. The diagram shows that the size of the time window has an influence on how strong the earliest contributing hits are emphasized with respect to the later ones: a smaller time window causes the first hits to be weighted stronger.

6.2 PMT hit selection

The selection of the hits used to reconstruct both the entry and the exit point is based on thresholds in charge and time and the time window after the first hits at the top and the bottom.

As one can see in figures 5.2 and 5.3 the PMT hits are always at times later than

$\sim 55\,\text{ns}$[1]. All pulses that appear earlier are most likely dark pulses or prepulses and thus, have to be rejected. In the reconstruction this is realized by a threshold in the start time of 50 ns for the top PMTs and of 70 ns for the bottom PMTs, where only hits with start times later than these thresholds contribute. The threshold for the bottom PMTs was chosen because of the time of flight of vertical muons in the inner veto of $t_\mu(H_{IV}) \approx 23\,\text{ns}$ (see equation (5.2)). These time thresholds are not meant to be varied.

The PMT hits, which contribute to the reconstruction, are chosen by a time window t_{window}, which is opened after the first hit at the top and the bottom inner veto. Only those hits with a start time difference to the first hit smaller or equal to this time window are used for the reconstruction. This time window should be chosen to be smaller or equal to 30 ns, what is based on the characteristic time of a photon travelling from one edge of the detector to the opposite edge in one area (top or bottom): $t_\gamma(2R_{IV}) \approx 32\,\text{ns}$. The slightly smaller value was chosen as the maximal PMT distance ($\sim 6\,\text{m}$) is smaller than the diameter of the inner veto. All hits, which appear later than this time are very likely due to reflected light.

Furthermore, all contributing hits must have charges larger than a chosen threshold q_{thresh}, which should be at least 1 pe. By applying this charge threshold the effects due to prepulses and dark pulses are reduced. Both the value for the time window and the charge threshold may be varied to restrict the number of hits contributing to the reconstruction.

In figure 6.2 the selection of the PMTs contributing to the reconstruction of the entry and exit point is depicted with the conditions which have to be satisfied by each PMT hit to contribute to the reconstruction. The reconstruction using the barycenter formula (see equation (6.2)) only makes sense if there are at least two contributing PMT hits for each the entry and the exit point. Therefore, only muon events with more than one PMT hit satisfying the selection criteria are reconstructed.

6.3 Tools to determine the performance

To test the performance of the reconstruction algorithms presented in this thesis the differences between the reconstructed entry and exit point coordinates and the true entry and exit point coordinates were calculated - for the x- and y-coordinate (X and Y), the radius (R) and the polar angle (ϕ):

$$\begin{aligned}
\Delta X &= X_{rec} - X_{true} \\
\Delta Y &= Y_{rec} - Y_{true} \\
\Delta R &= R_{rec} - R_{true} \\
\Delta \phi &= \phi_{rec} - \phi_{true}
\end{aligned} \qquad (6.4)$$

were the index *rec* stands for the reconstructed entry or exit point and the index *true* for the true entry or exit point (for the determination of the true points see section 5.2).

---

[1]In fact, all hits should be later than 50 ns as RoSS simulates all normal pulses (i.e. pulses that are not prepulses, late pulses or dark pulses) with an internal offset of 50 ns.
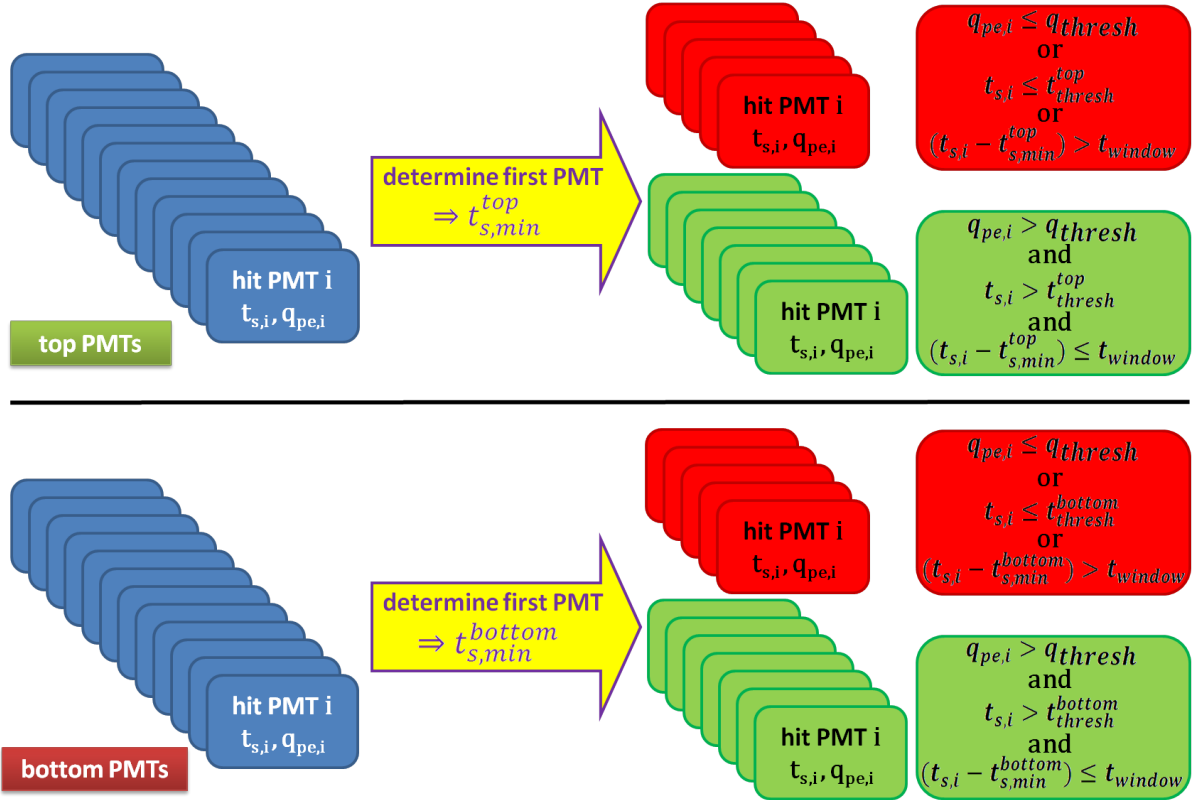
Figure 6.2: *The selection of the PMT hits contributing to the reconstruction with the conditions for a contribution on the right-hand side. The contributing PMT hits are depicted in green, and the rejected hits in red.*

In theory, the distributions of these differences for a number of muons should be narrow and symmetric with a shape similar to a Gaussian and centered around $0\,\mathrm{mm}$. Thus, the width and the mean value of these distributions should be good measures for the performance of the reconstruction. In particular, the used values are the mean and the standard deviation of the histogram or the mean and the width of a Gaussian fit (if applicable).

The differences for the radius R and the polar angle ϕ are calculated, because they contain complementary information as the distributions for ΔX and ΔY can suffer from symmetry effects. Both the radius and the polar angle are calculated from the x- and y-coordinate (reconstructed and true). Such symmetry effects may cause that systematic effects may not be seen in the distributions of ΔX and ΔY: for example a systematic radius shift to smaller radii.

6.4 Performance for vertical muons

Vertical muons (see section 4.3) were simulated without tracking info only. Hence, the true entry and exit point calculations were performed with the assumption of negligible deflection of the muons due to multiple scattering.

The best performance of the reconstruction was found for the following parameters in equation (6.3) [2]: the exponent of the charge term $m = 2$, the exponent of the timing term $n = 1$, a time window of $t_{window} = 10$ ns, and a charge threshold of $q_{thresh} = 1$ pe. 20 000 vertical muons with an energy of 100 GeV have been reconstructed with this parameter set for the plots shown in the following (figures 6.3 to 6.9).

6.4.1 Entry point reconstruction

In figure 6.3 the true and reconstructed entry points are depicted in the x-y-plane at the top PMT mean z-position. Figure 6.3a only contains the true entry points for muons that could have been reconstructed. One can see a void at small x and y caused by the chimney, which has a diameter of 600 mm. Vertical muons flying through the chimney can not be detected in the top inner veto. Both the entry and the exit points are only reconstructed, when at least two PMTs satisfy the selection criteria. The reconstructed entry points are depicted in figure 6.3b. As one can see the distribution of the points is not homogeneous:

- **Clustering:** One can see that the points cluster near PMT positions (see figure 2.8) and on the connecting lines between the PMTs, what results in the star-like sixfold symmetry. This can be explained by the nature of the barycenter calculation: the reconstructed points are always located in the area between the contributing PMTs. An additional explanation for the clustering can be given by the time window of $t_{window} = 10$ ns. As it was indicated by the blue labels in figure 6.1 a shorter time window causes stronger weights for the first hit PMTs. Therefore, the reconstructed barycenters are shifted more towards the first hit PMTs. Nevertheless, this short time window was chosen as it resulted in a better performance than longer time windows (see section 6.5).

- **Void at the center:** The void at the center of figure 6.3b can be partly explained by the muons, which are fully contained in the chimney. These muons can not be seen in the inner veto and therefore, a void of the size as for the true entry points can be expected. An explanation for the larger void can be given by an interplay of the chimney, the nature of the barycenter method and the time window. The chimney is opaque and has a reflective surface. Therefore, light produced by the muons has to be reflected several times to get to the opposite side of the chimney. The short 10 ns time window rejects most of the PMT hits due to this light. Hence, the contributing PMTs are restricted to those on that side of the chimney, where the

---

[2]This configuration was selected from different tested sets of the values for these parameters. The behaviour of the reconstruction for the different sets is shown in section 6.5 in more detail.
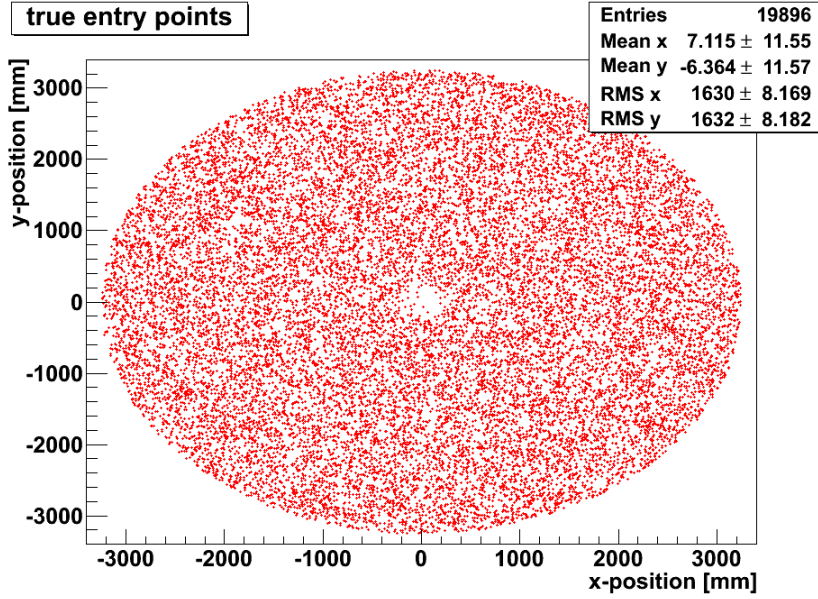
(a) True entry points
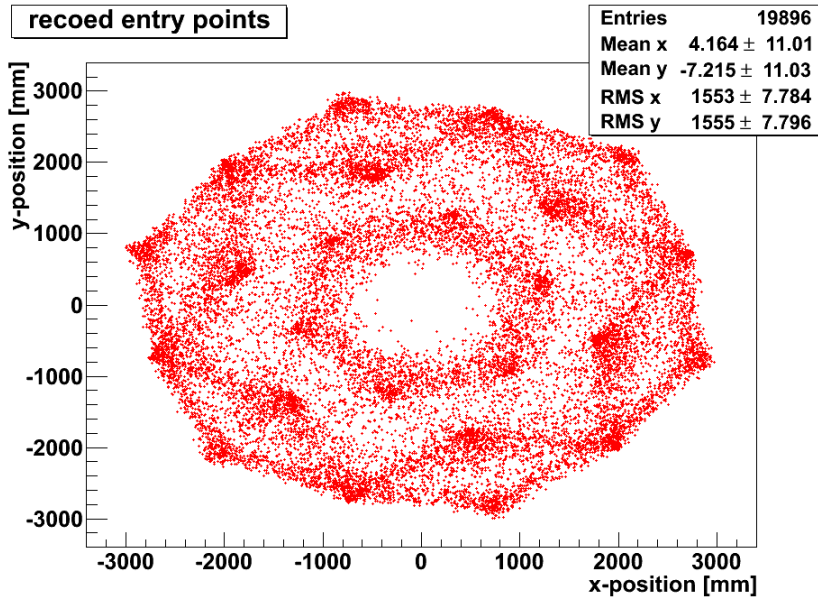
(b) Reconstructed entry points

Figure 6.3: *The true (a) and reconstructed (b) entry points in the x-y-plane at the top PMT mean z-position for 20 000 vertical muons (the missing muons either were contained in the chimney or were not reconstructed because of the time window). The void at the center of both plots can be explained by the presence of the chimney. The star like shape of the distribution of the reconstructed entry points - clustering of the points near PMT positions and on the connecting lines between the PMTs - can be explained by the nature of a barycenter calculation and the time window t_{window} (see text).*
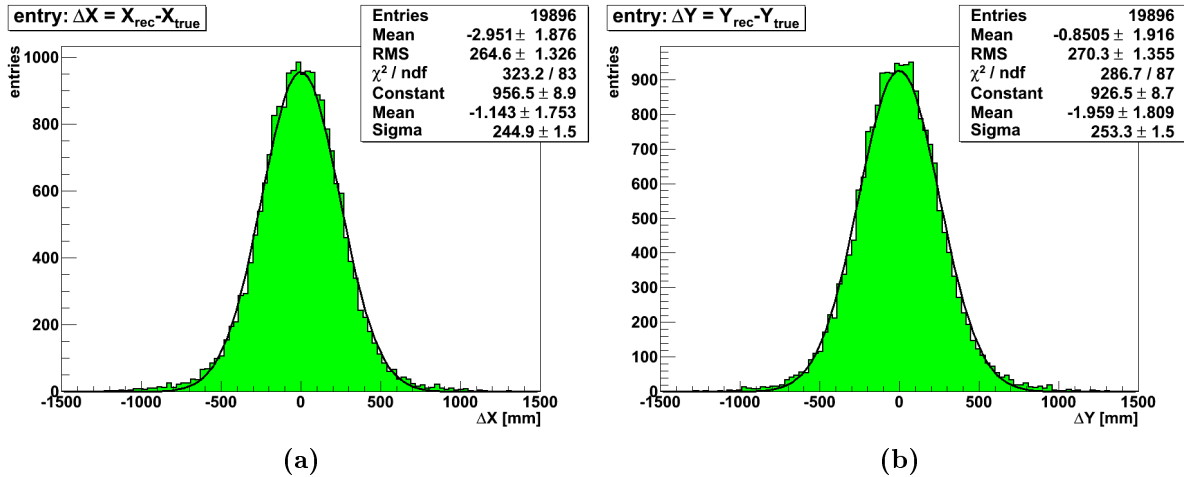
Figure 6.4: *Difference distributions for the x- and y-coordinate of the entry point for vertical 100 GeV muons. The distributions were fitted with a Gaussian to visualize the degree of symmetry.*

muon has passed. As the barycenters lie within the area between the contributing PMTs, the reconstructed entry points are shifted outwards.

- **Maximum radius of the reconstructed points:** The maximum radius of the reconstructed entry points is limited by the area within the positions of the outer ring PMTs. The radius coordinate of the outer ring PMTs is about 2.9 m for the inwards watching PMTs and about 3.1 m for the downwards facing PMTs. This limits the maximum reconstructed radius to these values.

To estimate the quality of the reconstruction the distributions of ΔX and ΔY (see equation 6.4) are depicted in figure 6.4. As one can see the distributions are centered at a value close to zero. The root mean square (RMS) of the histograms are about 270 mm and the σ of the Gaussians, which were fitted to the distributions, with about 250 mm. The slightly smaller values for the σ of the fit is caused by the actually non Gaussian shape of the distributions. This is also indicated by the values of the reduced χ^2, which should be close to one for a good fit. The deviation from the Gaussian shape can be explained by the inhomogeneous distribution of the reconstructed points (see figure 6.3b).

Figure 6.5 shows the distributions of ΔR and $\Delta \phi$ for the reconstructed vertical muons. As one can see the mean of the distribution for ΔR (histogram and fit) is shifted to negative values by almost 70 mm. This can be explained by the reduced maximum radius of the reconstructed points, what also causes the increased number of entries for $\Delta R < -700$ mm. In addition, a shadowing appears when the muons pass behind the inwards watching outer ring PMTs. Hence, those PMTs can see the light from this muon by reflection only. This causes a smaller charge and a later pulse start time than for the direct light. Therefore, the reconstructed entry point is shifted towards the PMTs,
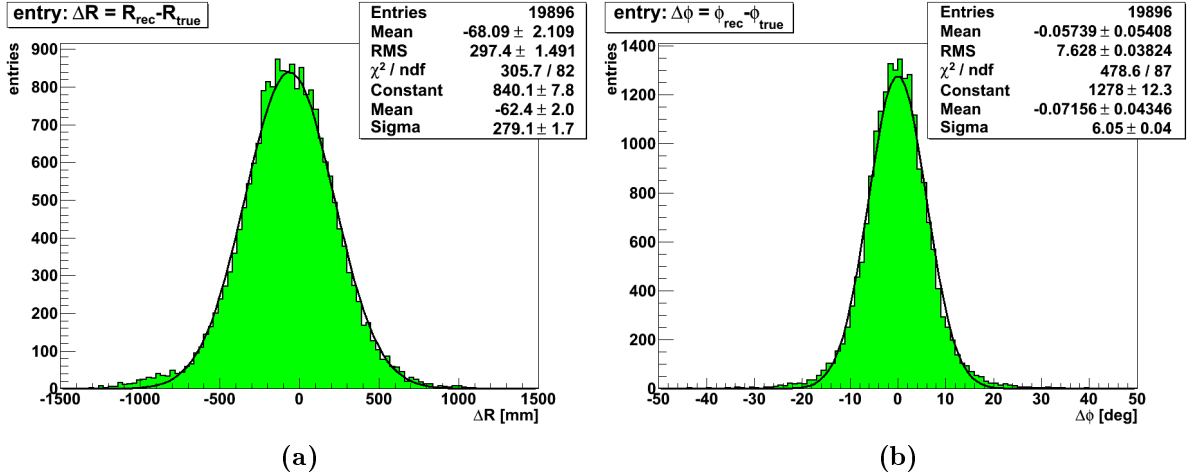
Figure 6.5: *Difference distributions for the R- and ϕ-coordinate of the entry point for vertical $100\,GeV$ muons. The distributions were fitted with a Gaussian to visualize the degree of symmetry.*

which can see this light directly.

In the corresponding distribution for $\Delta\phi$ the distortion from the Gaussian shape is a bit stronger as for the x- and y-coordinate. An explanation for this can be given by the fact that the accuracy in the determination of the polar angle worsens for smaller radii. Here a large deviation in the polar angle causes only a small deviation in the corresponding x- and y-coordinates. For the reconstructed entry point this effect is relatively small compared to the exit point reconstruction shown in the next section. This can be explained by the void at the center, which effectively limits the reconstructed radius to values larger than $600\,mm$.

6.4.2 Exit point reconstruction

In figure 6.6 the true and reconstructed exit points are depicted. The plot for the true exit points shows no voids and all 20 000 muons could have been reconstructed. The reconstructed exit points again show a inhomogeneous distribution with the following characteristics:

- **Clustering:** As seen for the entry points, the exit points show a clustering of the PMTs near PMT positions and on their connecting lines. This can be explained in the same way as for the entry points: the nature of the barycenter calculation and the short time window.

- **Six voids:** One also can see six voids in figure 6.6b. These voids are caused by the six buffer feet (a mechanical structure of the detector, see figure 2.7). The buffer feet are not completely closed as the chimney, but nevertheless can have an effect on the reconstruction by shadowing effects. As mentioned before shadowing
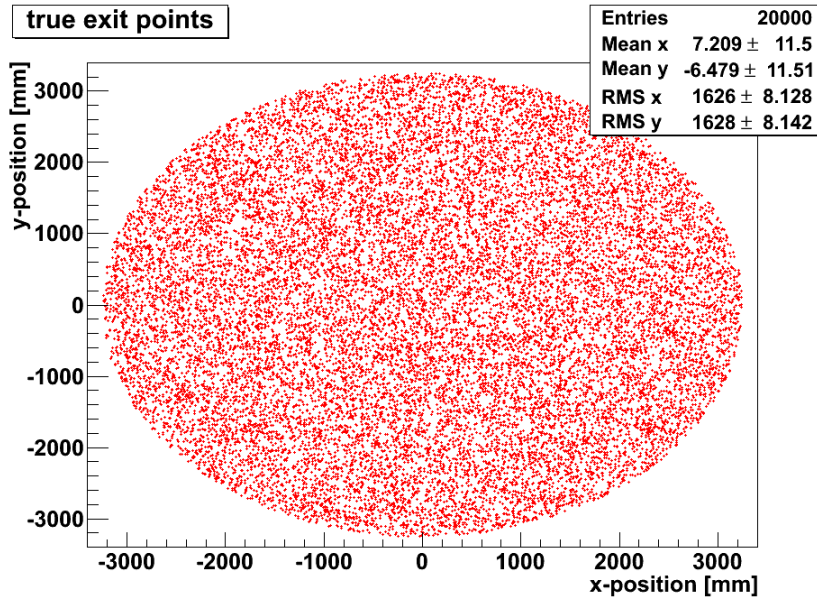
(a) True exit points
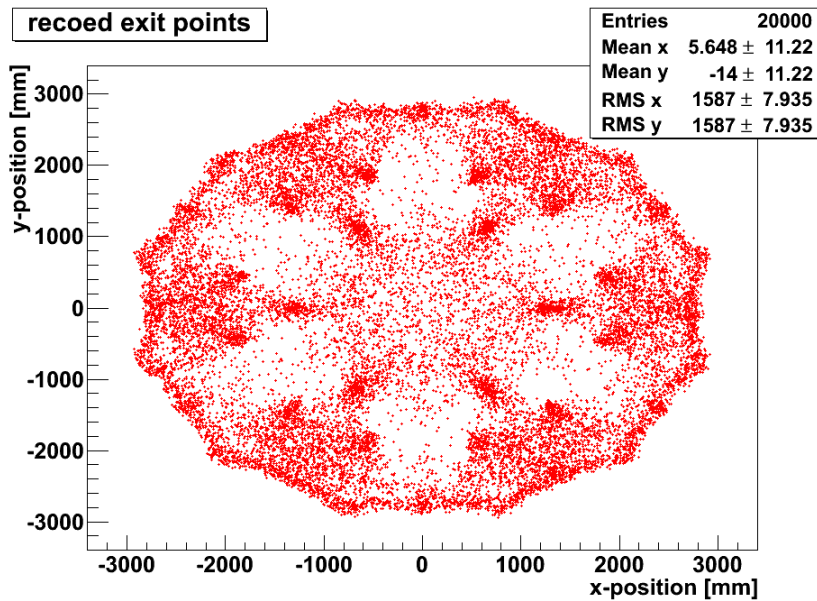
(b) Reconstructed exit points

Figure 6.6: *The true (a) and reconstructed (b) exit points in the x-y-plane at the bottom PMT mean z-position for vertical muons. The six voids can be explained by the six buffer feet. The clustering of the points can be explained by the nature of the barycenter calculation and the time window.*

causes the PMTs to see the reflected light produced by the muons. The information concerning the muon track is strongly distorted as the resulting charge is smaller and the hit time later than for direct light produced at the same distance. This causes the reconstructed points to be shifted to that side of the buffer feet, where the PMTs can see the direct light, hence, on that side of the buffer feet, where the muon passes the bottom inner veto. Muons passing inside a buffer foot may only be seen directly by the PMT facing this buffer foot. This causes a shift towards this PMT, i.e. a shift to larger radii. A similar effect appears for muons passing close to a buffer foot, but not inside the foot. Here the direct light is most likely seen by the inwards watching outer ring PMTs, while the inner ring PMTs see reflected light (see figure 6.6b). Hence, the reconstructed entry points are shifted to larger radii.

- **Maximum reconstructable radius:** Again one can see that the maximum reconstructed radii of the exit points are limited, what is due to the barycenter calculation, causing all points to be within the area between the contributing PMTs. The outer ring PMT radius coordinates are $\sim 2.9\,\mathrm{m}$ for the inwards watching and $\sim 3.1\,\mathrm{m}$ for the upwards watching PMTs.

The distributions for the exit point ΔX and ΔY (see figure 6.7) are both symmetric and centered close to zero. The RMS of the histograms are about $245\,\mathrm{mm}$ and the σ of the fitted Gaussians slightly larger than about $230\,\mathrm{mm}$. Compared to the entry point reconstruction the exit points seem to be reconstructed a bit better by about $20\,\mathrm{mm}$. As one can see the Gaussians fit even worse than the ones for the entry points, indicated by the larger maxima and the increased number of entries at the tails, especially for the distribution of ΔX. The larger contribution of entries at large $|\Delta X|$ than at large $|\Delta Y|$ is caused by the different symmetries in the arrangement of the PMTs.

The ΔR-distribution (figure 6.8a) shows a stronger asymmetry than the one for the entry points (figure 6.5a). Furthermore, the mean of the distribution is shifted to about $-20\,\mathrm{mm}$, what is smaller than the shift for the entry points to about $-70\,\mathrm{mm}$. Here two contrary effects play a role: one effect is the shift of the mean to negative values caused by the maximum radius of the PMT positions together with muons passing behind the inwards watching outer ring PMTs. The second effect is a shift to larger radii due to the buffer feet causing the shoulder at $\Delta R > 500\,\mathrm{mm}$.

As it was already explained for the $\Delta\phi$ distribution of the entry points, the accuracy in the determination of the polar angle worsens with decreasing radius. This can also be seen in the distribution for the exit points depicted in figure 6.8b. Here this effect is much stronger than for the entry points and results in a stronger discrepancy to the Gaussian fit. Furthermore, the buffer feet play also a role in this distribution as they cause the reconstructed entry points to be shifted on that side of the buffer feet where the muon has passed. The number of muons shifted to one side of a buffer foot is approximately equal to the number of muons reconstructed to the opposite side. Therefore, these muons contribute to the $\Delta\phi$-distribution symmetrically.
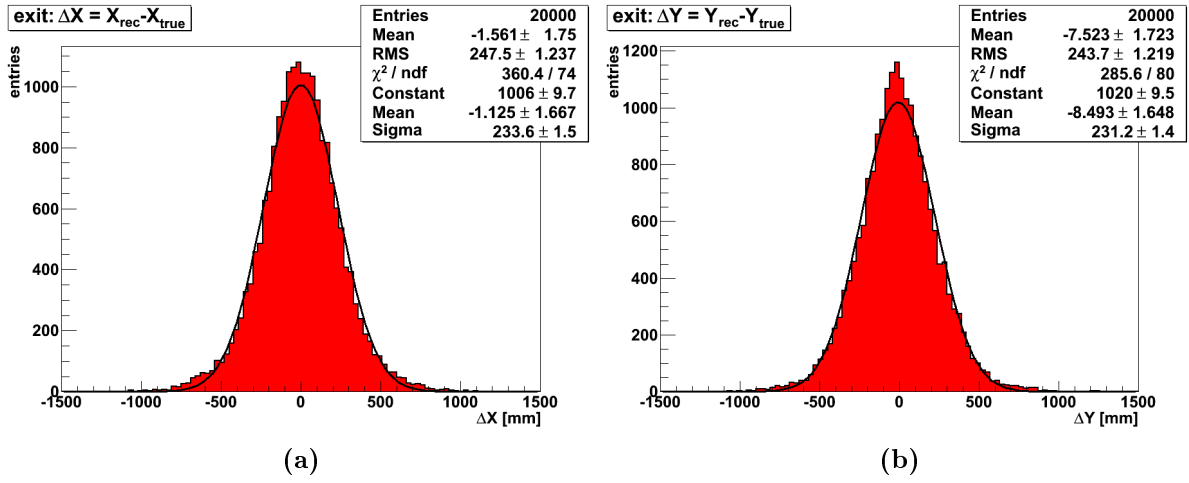
Figure 6.7: *Difference distributions for the x- and y-coordinate of the exit point for vertical 100 GeV muons. The distributions were fitted with a Gaussian to visualize the degree of symmetry.*
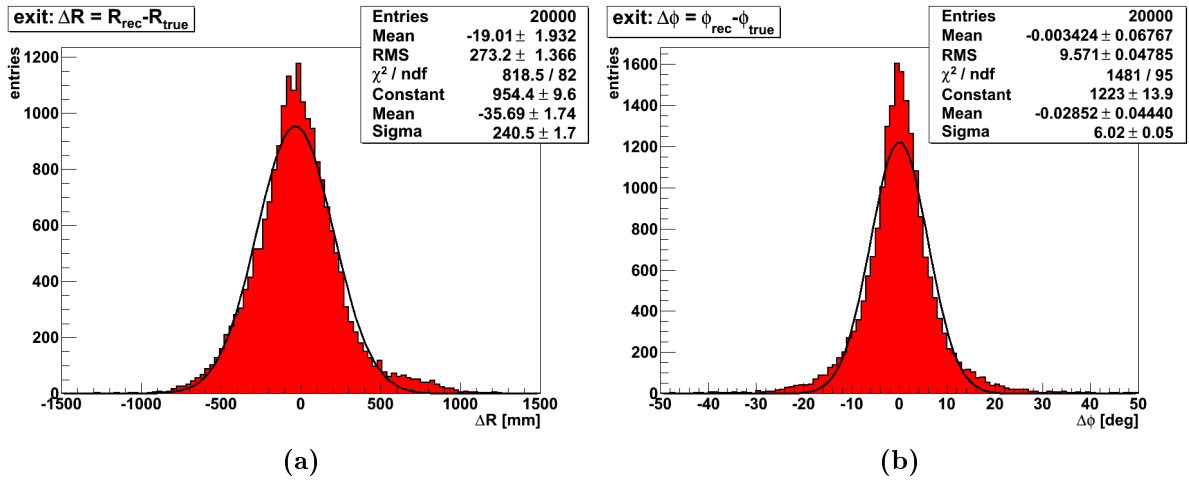
Figure 6.8: *Difference distributions for the R- and φ-coordinate of the exit point for vertical 100 GeV muons. The distributions were fitted with a Gaussian to visualize the degree of symmetry.*

6.4.3 Reconstructed momentum direction

From the reconstructed entry and exit point the reconstructed muon momentum direction $\hat{p}_{rec}$ can be calculated by equation 6.1. To check the performance the angle between the true momentum direction[3] $\hat{p}_{true}$ and the reconstructed momentum direction $\hat{p}_{rec}$ was calculated for each muon event. Figure 6.9 shows a histogram of these values for the 20 000 vertical muons. Furthermore, the distribution is relatively narrow, i.e. the muon momentum direction is reconstructed with a relatively good precision: the maximum is at about 2.5 degrees. The good precision can be achieved because of the relatively large distance between the reconstructed entry and exit points, which is about 6.3 m.
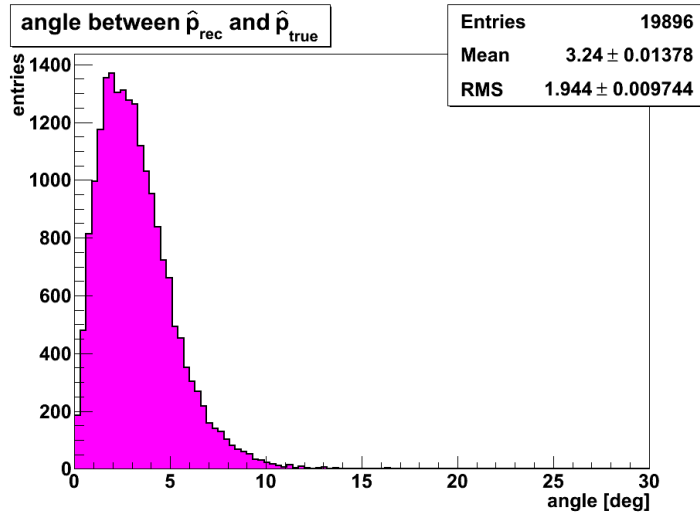
Figure 6.9: *The distribution of the angle between the true primary momentum direction $\hat{p}_{true}$ and the reconstructed momentum direction $\hat{p}_{rec}$ of vertical muons (angle in degree (deg)).*

6.5 Finding the best performance configuration

The performance was analysed for different sets of the reconstruction parameters. First different configurations of the exponents in the weightings (equation (6.3)) were tested with values for the charge term exponent m between 0 and 4 and values for the timing term exponent n between 0 and 3, where $t_{window} = 30\,\text{ns}$ and $q_{thresh} = 1\,\text{pe}$ were fixed. The different exponents n for the timing term were tested with a fixed exponent $m = 2$ for the charge term. As shown in figure 6.10a the reconstruction performance - as indicated by the widths of the ΔX-distributions - does not change very much for the different exponents. The best results for both the entry and the exit point reconstruction can be obtained for $n = 1$. Furthermore, one can see that the worst result is achieved, when the timing information is not used, what means $n = 0$.

---

[3]Here the primary momentum direction of the muons is used.

The different exponents m for the charge term were varied for a fixed $n = 1$. This parameter seems to have a larger effect on the performance of the barycenter reconstruction. As one can see in figure 6.10b an increasing n causes a significant reduction of the shift of the mean of the ΔR-distribution to negative values for both the entry and the exit point. The widths of the ΔX distributions indicated by the RMS of the histograms show a minimum for $m = 2$ (exit point) and $m = 3$ (entry point). This is depicted in figure 6.10c. As for the timing information the reconstruction shows the worst result, when the charge information is not used (i.e. $m = 0$). Finally, the causes for choosing $m = 2$ are the following:

- The performance of the momentum direction reconstruction is the best. Figure 6.10d shows the mean values of the distributions of the angle between the true momentum direction $\hat{p}_{true}$ and the reconstructed momentum direction $\hat{p}_{reco}$ for different exponents m.

- The distributions of ΔX and ΔY have a minimal width (see figure 6.10c for ΔX).

- The reconstructed points do not cluster as much in the vicinity of the PMT positions as for larger exponents m of the charge term.

- The reconstruction of the polar angle ϕ shows the best results.

After the exponents were fixed to $m = 2$ and $n = 1$, the charge threshold q_{thresh} was varied between $1\,\mathrm{pe}$ and $100\,\mathrm{pe}$ for a fixed time window $t_{window} = 30\,\mathrm{ns}$. With increasing q_{thresh} the number of reconstructable muon events decreases for both the entry and the exit points, what could be expected. As one can see in figure 6.11a for the widths of the ΔX-distributions, the performance of the entry point reconstruction slightly increases by about $10\,\mathrm{mm}$ for an increasing q_{thresh}. The exit point reconstruction performance shows a contrary characteristic as it decreases by about $7\,\mathrm{mm}$. As a result of this contrary behaviour the mean values of the angle between the true $\hat{p}_{true}$ and the reconstructed muon momentum direction $\hat{p}_{rec}$ are almost constant for all values of q_{thresh} (see figure 6.11b). The relatively small effect of q_{thresh} on the reconstruction performance is caused by the weightings (see equation 6.3), which emphasize hits with large charges stronger. Hence, the influence of hits with small charges is reduced. To achieve the maximum efficiency in the reconstruction of the muons the charge threshold was set to $q_{thresh} = 1\,\mathrm{pe}$.

The impact of the size of the time window was found to be larger than that of the charge threshold. The performance was tested for three different values for the time window (with fixed exponents $m = 2$ and $n = 1$ and $q_{thresh} = 1\,\mathrm{pe}$): $10\,\mathrm{ns}$, $20\,\mathrm{ns}$ and $30\,\mathrm{ns}$. The reconstruction improves significantly for smaller time windows: the difference distributions are more narrow (see figure 6.12a for ΔX) and the ΔR-distributions show smaller shifts of the mean to negative values (see figure 6.12b). The reconstruction of the momentum direction also improves (see figure 6.12c) as the entry and exit points are reconstructed more precisely. A negative effect is that the reconstructed entry and exit points show a stronger clustering near the PMT positions. Furthermore, a decreasing

(a) ΔX-distribution width as indicated by the histograms RMS for **different timing exponents** n (fixed $m = 2$, $t_{window} = 30\,ns$ and $q_{thresh} = 1\,pe$).

(b) ΔR-distribution mean as indicated by the histograms mean value for **different charge exponents** m (fixed $n = 1$, $t_{window} = 30\,ns$ and $q_{thresh} = 1\,pe$).

(c) ΔX-distribution width as indicated by the histograms RMS for **different charge exponents** m (fixed $n = 1$, $t_{window} = 30\,ns$ and $q_{thresh} = 1\,pe$).

(d) Mean values of the distributions of the angle between $\hat{p}_{true}$ and $\hat{p}_{reco}$ for **different charge exponents** m (fixed $n = 1$, $t_{window} = 30\,ns$ and $q_{thresh} = 1\,pe$).

Figure 6.10: *The behaviour of the barycenter reconstruction for charge exponents m between 0 and 4 and timing exponents n between 0 and 3. The best performance of the reconstruction can be reached for $m = 2$ and $n = 1$.*
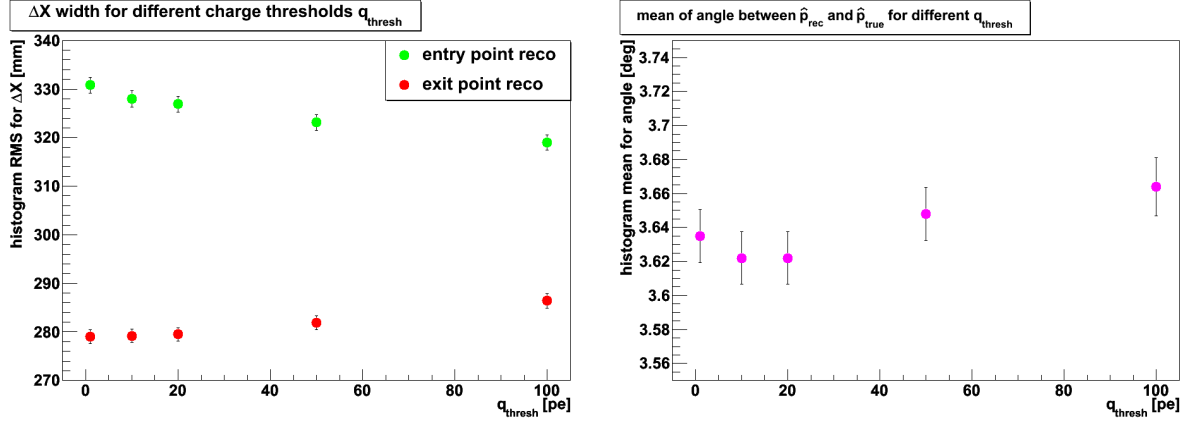
(a) ΔX-distribution width as indicated by the histograms RMS for **different charge thresholds** q_{thresh} (fixed $m = 2$, $n = 1$ and $t_{window} = 30\,ns$).

(b) Mean values of the distributions of the angle between $\hat{p}_{true}$ and $\hat{p}_{reco}$ for **different charge thresholds** q_{thresh} (fixed $m = 2$, $n = 1$ and $t_{window} = 30\,ns$).

Figure 6.11: The behaviour of the barycenter reconstruction for charge thresholds q_{thresh} between 1 and 100 pe. A threshold of $q_{thresh} = 1\,pe$ was chosen for the reconstruction plots shown in this chapter as the influence of this parameter is rather small. Furthermore, the efficiency of the reconstruction is maximal for $q_{thresh} = 1\,pe$.

time window causes a decreasing number of contributing PMT hits as less hits satisfy the selection criteria. This leads to a reduction of the reconstructable entry or exit points as it may happen that only one PMT hit passes the selection.

The improvement of the performance for smaller time windows is caused by a decreasing influence of hits due to reflected light. The PMTs, the chimney at the top inner veto and the buffer feet at the bottom inner veto cause shadowing effects. Shadowed PMTs only see reflected light from the muon, what results in hits, which appear later and with smaller charges than hits due to direct light produced by a muon at the same distance. In the weightings (equation (6.3)) these hits are wrongly taken into account. With a time window $t_{window} = 10\,ns$ the influence of hits due to reflected light can be reduced as the contributing PMTs are limited to those in a maximum distance of roughly $2\,m$ to the true muon track.

As an outcome of these systematic studies the final combination of the reconstruction parameters used for the barycenter method is the following: the exponent of the charge term in the weightings is $m = 2$, the exponent of the timing term is $n = 1$, the time window is $t_{window} = 10\,ns$ and the charge threshold is $q_{thresh} = 1\,pe$.
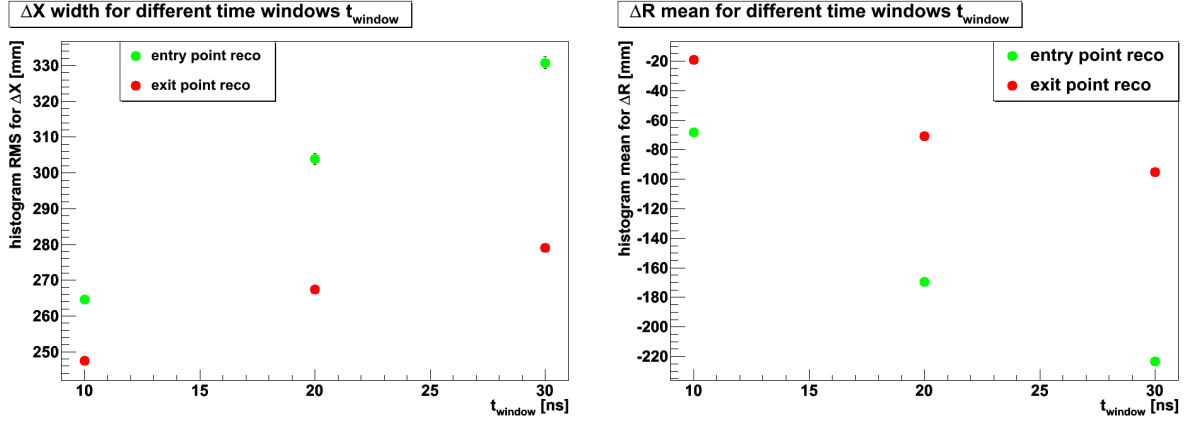
(a) ΔX-*distribution width as indicated by the histograms RMS for* **different time windows** t_{window} *(fixed* $m = 2$, $n = 1$ *and* $q_{thresh} = 1\,pe$).

(b) ΔR-*distribution mean as indicated by the histograms mean value for* **different time windows** t_{window} *(fixed* $m = 2$, $n = 1$ *and* $q_{thresh} = 1\,pe$).
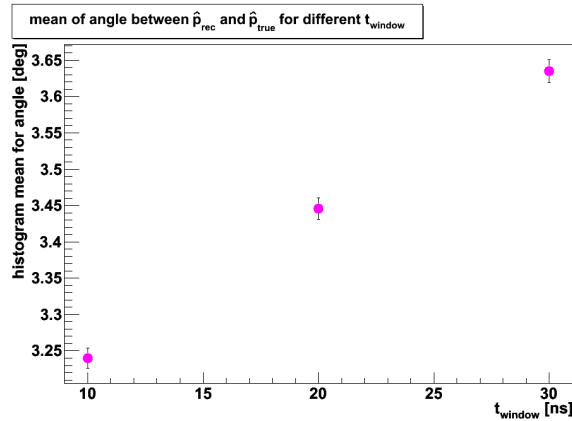
(c) *Mean values of the distributions of the angle between* $\hat{p}_{true}$ *and* $\hat{p}_{reco}$ *for* **different time windows** t_{window} *(fixed* $m = 2$, $n = 1$ *and* $q_{thresh} = 1\,pe$).

Figure 6.12: *The behaviour of the barycenter reconstruction for time windows* t_{window} *between* 10 *and* 30 *ns. The best results are obtained for a time window of* $t_{window} = 10\,ns$.

6.6 Performance for inclined muons

The barycenter reconstruction was also tested for inclined muons of the kind described in section 4.4. For all simulated inclined muons the tracking information of the primary muons are available. Thus, the true entry and exit points were determined precisely as described in section 5.2.2. The plots, which will be shown in this section (figures 6.13 to 6.19), rely on a reconstruction of 50 000 inclined 100 GeV muons with the set of parameters, which was determined in the previous section to have optimal performance.

6.6.1 Entry point reconstruction

Figure 6.13 shows the true and reconstructed entry points. As one can see the density of the true entry points (figure 6.13a) gets smaller for large radii ($R \gtrsim 3000\,\text{mm}$). This is caused by the way of simulating the inclined muons as described in section 4.4. The areas on which the two random points are generated are above and beneath the whole detector. The probability to get a pair of points leading to an almost vertical muon at large radii is relatively low. Hence, entry (and also exit) points at large radii appear less often. Figure 6.13a only contains the true points, in case that an entry point could have been reconstructed. Therefore, the void at small x and y is due to muons, which were fully contained within the chimney. In addition, some of the muons could not have been reconstructed due to the short time window $t_{window} = 10\,\text{ns}$.

The reconstructed entry points (figure 6.13b) show a behaviour which is similar to the behaviour for vertical muons, but the inhomogeneous structure is more emphasized as the plot contains more points. The following characteristics can be seen:

- **Clustering:** As for the vertical muons (see 6.4.1), the reconstructed entry points cluster near PMT positions and on the connecting lines, resulting in the star-like sixfold symmetry. The same argumentation for this behaviour as for the vertical muons holds. A difference to the vertical muons appears in the density of reconstructed points on the connecting lines between the outer ring PMTs. This is caused by the lower density of true entry points at radii $R \gtrsim 3000\,\text{mm}$.

- **Void at the center:** Also the tracks of the inclined muons can be fully contained in the chimney and thus, do not produce light in the top inner veto. This partly explains the void at the center of figure 6.13a. The size of the void is caused by the interplay of the nature of a barycenter calculation and the small time window.

- **Maximum reconstructable radius:** Again it can be seen that the maximal reconstructed radius is limited by the positions of the PMTs, caused by the nature of the barycenter calculation.

Figure 6.14 shows the distributions of ΔX and ΔY of the entry points for the 50 000 inclined muons. As for the vertical muons these distribution are centered close to zero and quite symmetric. The widths indicated by the RMS of the histograms and the σ of the Gaussian fit are about 265 mm and 245 mm and hence very similar to the widths for
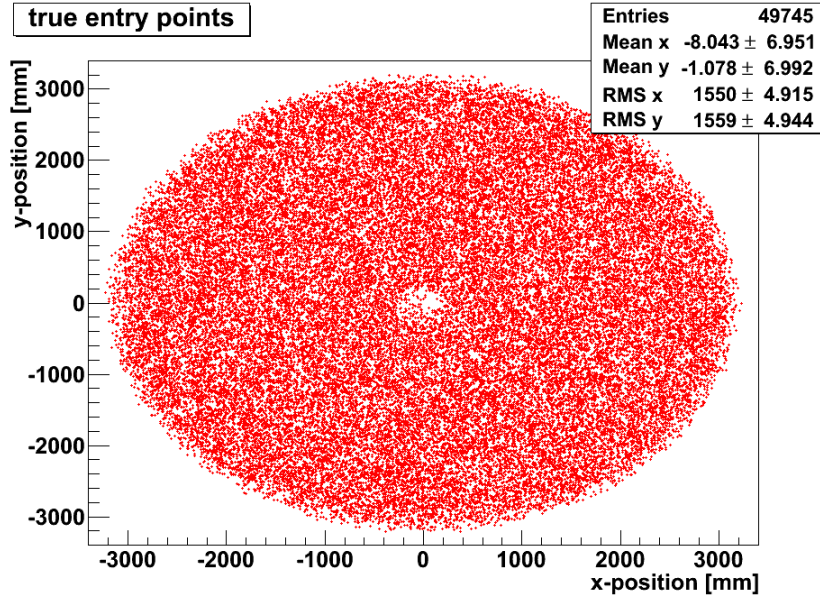
(a) True entry points
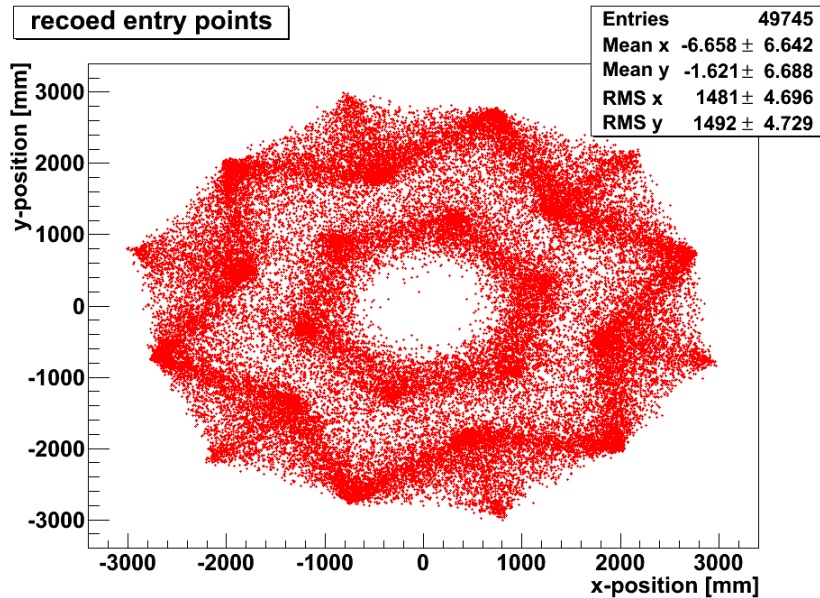
(b) Reconstructed entry points

Figure 6.13: *The true (a) and reconstructed (b) entry points in the x-y-plane at the top PMT mean z-position for 50 000 inclined 100 GeV muons (the missing muons either were contained in the chimney or were not reconstructed because of the time window). As for the vertical muons, the clustering can be explained by the nature of the barycenter method and the time window. The void in the center is due to the presence of the chimney combined with the short time window.*
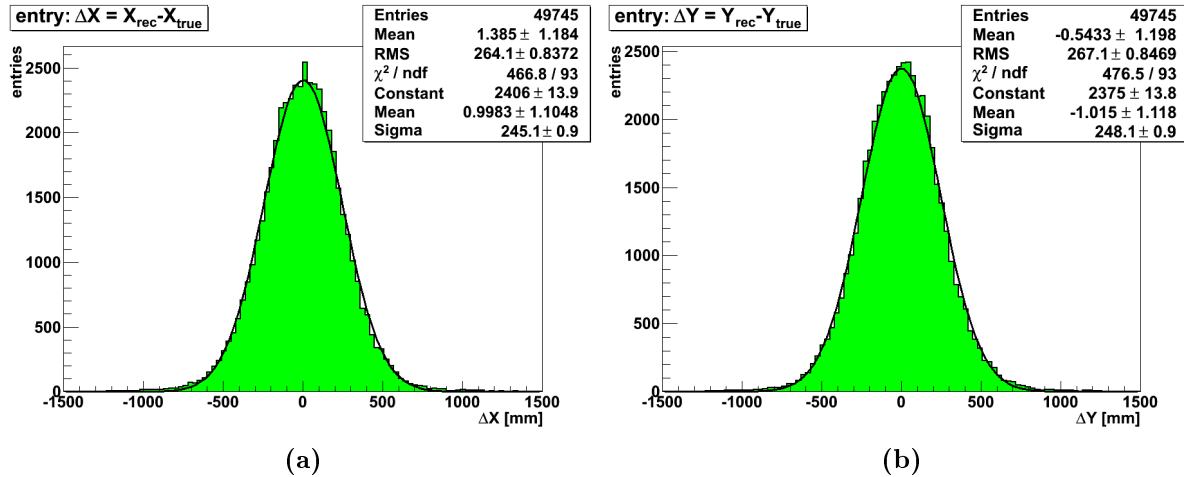
Figure 6.14: *Difference distributions for the x- and y-coordinate of the entry point for inclined 100 GeV muons. The distributions were fitted with a Gaussian to visualize the degree of symmetry.*

vertical muons. From this one can conclude that the barycenter approach depends only weakly on the inclination of the muons, what indicates that the barycenter reconstruction is a very robust method.

The difference distributions for the radius and the polar angle for the entry points are shown in figure 6.15. The distribution for ΔR shows a slight asymmetry and a shift of the mean (histogram and fit) to a negative value of about $-55\,\mathrm{mm}$. This is about $15\,\mathrm{mm}$ less than for vertical muons, what can be explained by the lower density of true entry points at large radii $R \gtrsim 3000\,\mathrm{mm}$: muons with such entry points, which are reconstructed to smaller radii, are seldom and thus, have a smaller contribution. This also explains the smaller fraction of reconstructed entry points with $\Delta R < -700\,\mathrm{mm}$ compared to vertical muons (see figure 6.5a). At the same time the contribution of muons passing the top inner veto in the vicinity of the chimney is slightly increased, what increases the contribution of reconstructed entry points with $\Delta R > 0$.

Figure 6.15b shows the difference distribution for the polar angle of the entry points. Again, one can see the deviations from the Gaussian shape indicated by the larger maximum and the increased contribution of reconstructed entry points with large $|\Delta\phi|$. Furthermore, the distribution has a width, which is by about $0.2\,$degrees larger than that for the vertical muons (indicated by the RMS of the distributions). This small deviation is caused by the lower density of muons with true entry points at $R \gtrsim 3000\,\mathrm{mm}$ as the contribution of muons with smaller true radii is increased.
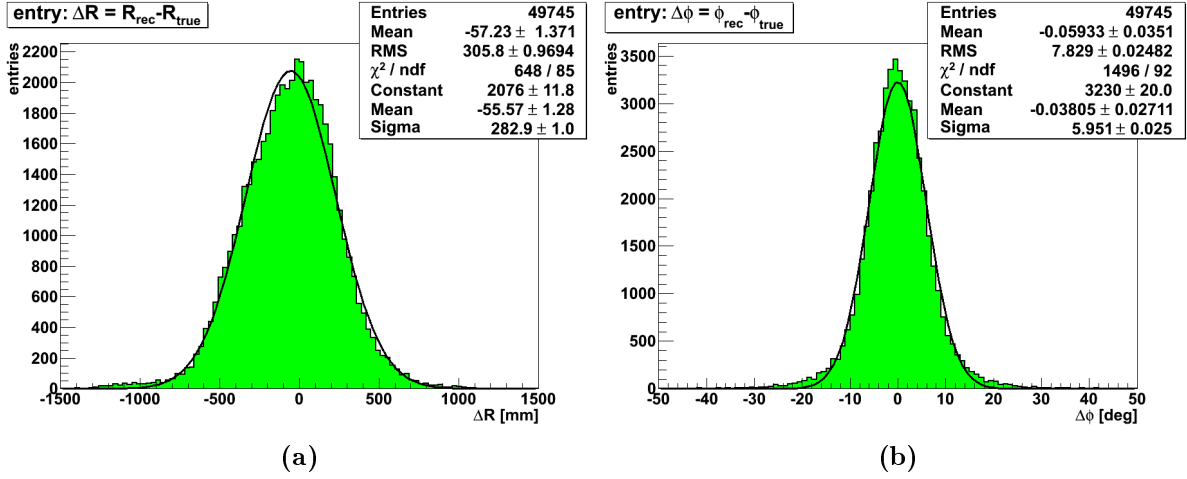
Figure 6.15: *Difference distributions for the radius and the polar angle of the entry point for inclined 100 GeV muons. The distributions were fitted with a Gaussian to visualize the degree of symmetry.*

6.6.2 Exit point reconstruction

Figure 6.16 shows the true and reconstructed exit points for the 50 000 inclined muons. Regarding the distribution of the true exit points (figure 6.16a) one can see the lower density of points at large radii again. The missing four muons were not reconstructed because of the time window of 10 ns. Figure 6.16b shows the distribution of the reconstructed exit points. As for the reconstructed entry points the reconstructed exit points show an inhomogeneous distribution similar to the distribution for vertical muons (see figure 6.6b). One can see the following characteristics:

- **Clustering:** Also the reconstructed exit points show clustering and the density of the points on the connecting lines between the outer ring PMTs is lower than for the vertical muons caused by the lower density of true points at large radii.

- **Six voids:** As for the vertical muons one can see the six voids in the vicinity of the buffer feet caused by shadowing effects.

- **Maximum reconstructable radius:** Again the maximum reconstructed radii are limited by the nature of the barycenter method.

Figure 6.17 shows the distributions of ΔX and ΔY for the exit points for inclined muons. Again, the distributions look symmetric and are centered close to zero. The widths indicated by the RMS of the histogram and the σ of the fit are about 240 mm and about 230 mm, respectively. These values again are very similar to the widths for the corresponding distributions for vertical muons (see figure 6.7). Hence, the exit point reconstruction also seems to have a weak dependency concerning the inclination of the muons.
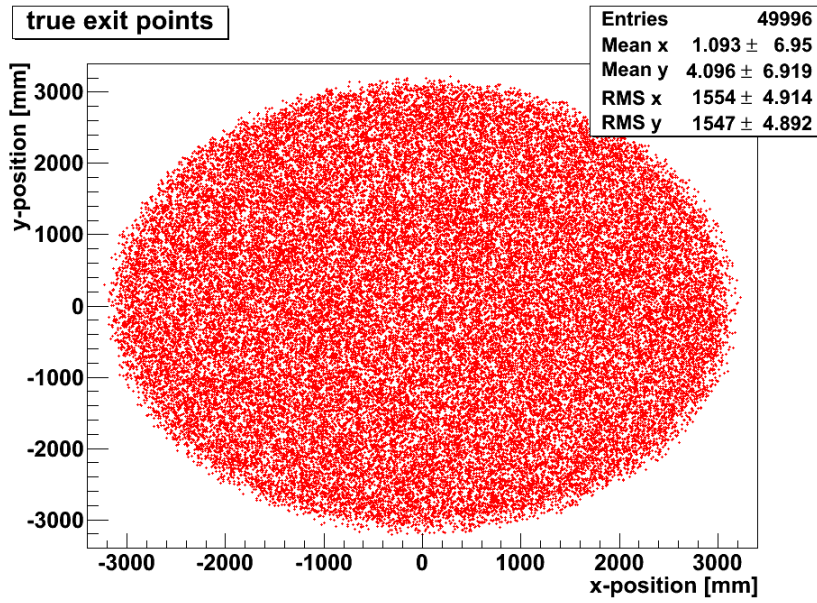
(a) True exit points
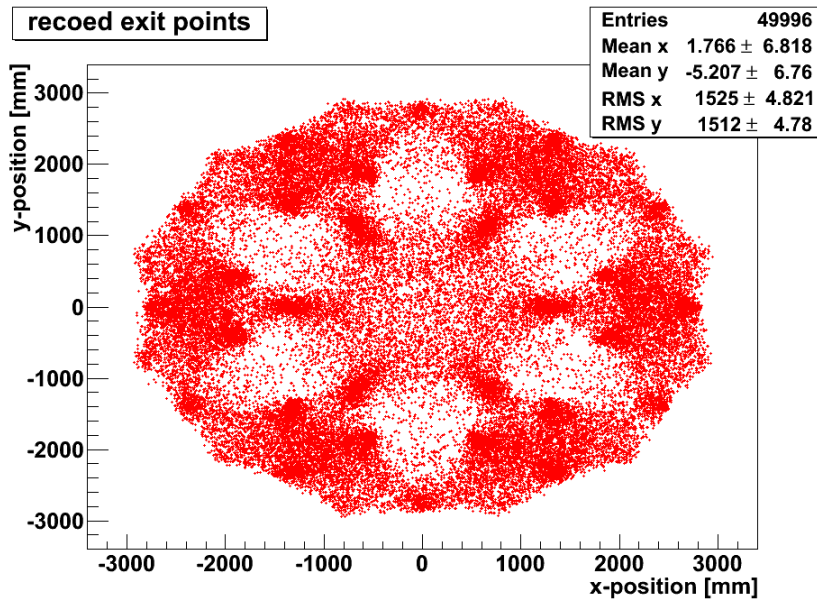
(b) Reconstructed exit points

Figure 6.16: *The true (a) and reconstructed (b) exit points in the x-y-plane at the bottom PMT mean z-position for 50 000 inclined 100 GeV muons (some muons were not reconstructed because of the time window). The six voids can be explained by the six buffer feet. The clustering of the points can be explained by the nature of the barycenter calculation and the time window.*
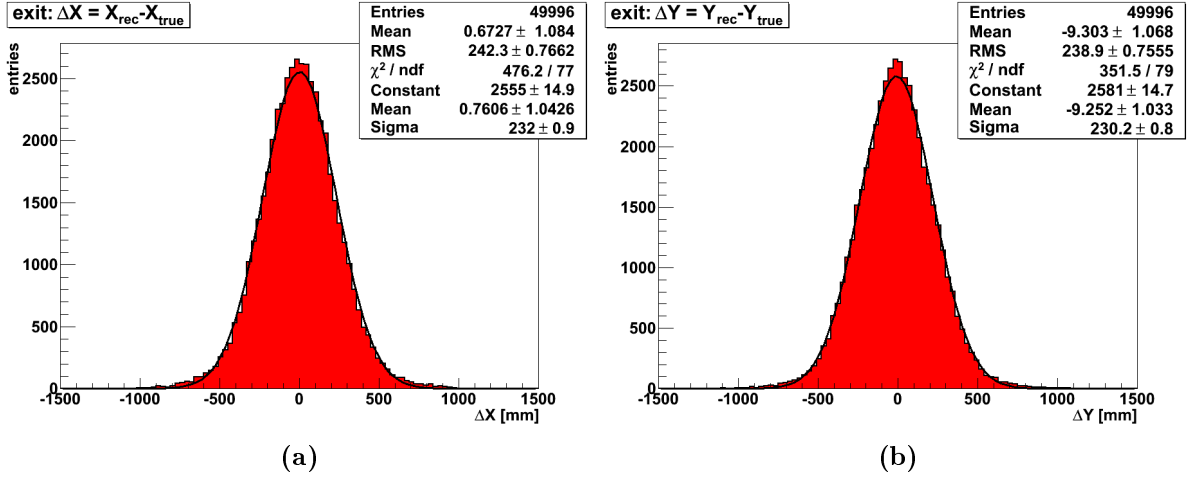
Figure 6.17: *Difference distributions for the x- and y-coordinate of the exit point for inclined 100 GeV muons. The distributions were fitted with a Gaussian to visualize the degree of symmetry.*

The distributions of ΔR and $\Delta\phi$ for the exit points are depicted in figure 6.18. The distribution of ΔR shows a shift of the mean to a negative value, which is smaller by about 7 mm compared to the shift for vertical muons. This is caused by a smaller contribution of entries at $\Delta R < -500$ mm due to the lower density of true exit points at large radii, while the shoulder at $\Delta R > 400$ mm has a similar size.

As for the entry points, the width of the $\Delta\phi$-distribution for the exit points is slightly broader for the inclined muons than for the vertical muons by about 0.1 degrees.

6.6.3 Reconstructed momentum direction

In figure 6.19 one can see the distribution of the angle between the true and the reconstructed muon momentum direction - $\hat{p}_{true}$ and $\hat{p}_{rec}$ - for the inclined muons. As one can see the maximum of this distribution is at about 3 degree and therefore is about 0.5 degrees larger than the value for the plot corresponding to vertical muons (figure 6.9). Furthermore, the value for RMS is also increased by about 0.2 degrees compared to that for vertical muons. In spite of these slightly increased values the obtained results show that the barycenter reconstructions performs very robust regarding the inclination of the muons.
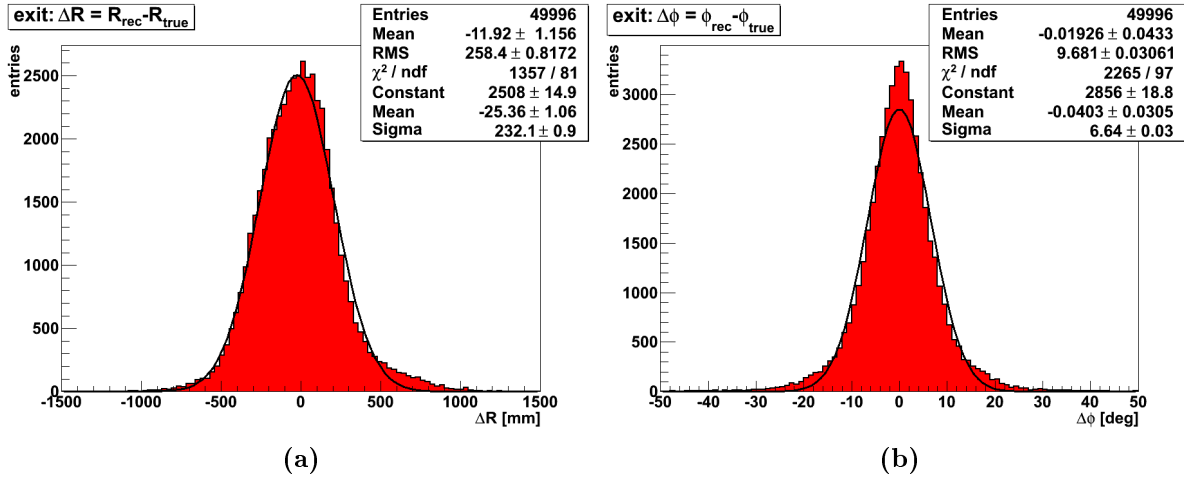
Figure 6.18: *Difference distributions for the radius and the polar angle of the exit point for inclined 100 GeV muons. The distributions were fitted with a Gaussian to visualize the degree of symmetry.*
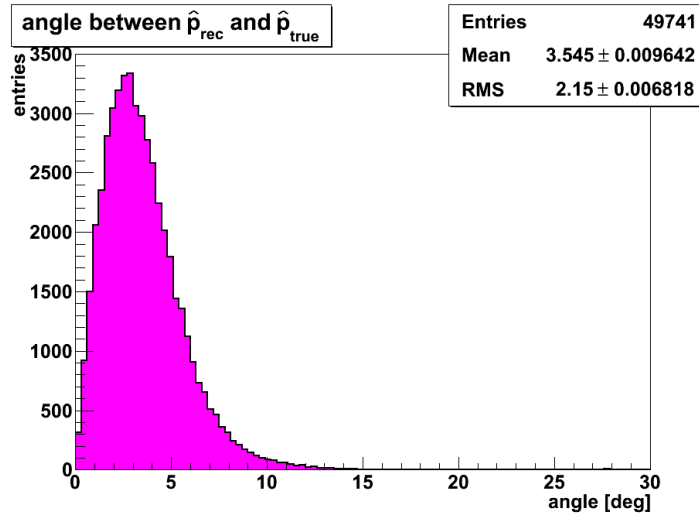
Figure 6.19: *The distribution of the angle between the true primary momentum direction $\hat{p}_{true}$ and the reconstructed momentum direction $\hat{p}_{rec}$ of inclined 100 GeV muons (angle in degree (deg)).*

6.7 Summary

The barycenter method relies on the reconstruction of an inner veto entry point and an inner veto exit point and uses the charge and timing information of the hit PMTs. The hits used to reconstruct these points are selected by a charge threshold and a time window, which is opened after the first hit at the top and bottom inner veto, respectively. As the barycenter method is based on a rather simple formula - and not on a time consuming fit to the data - the speed of reconstructing the points is very high.

In the present work the algorithm was tested for vertical 100 GeV muons with different sets of the reconstruction parameters. The results for the set showing the best performance of the reconstruction were discussed in more detail. This parameter set was also used to test the method with inclined 100 GeV muons and the results were found to be very similar to those for vertical muons, what suggests that the barycenter reconstruction hardly depends on the inclination of the muons. Compared to earlier studies on muon track reconstructions for DOUBLE CHOOZ the accuracy of the determination of the muon momentum direction with about 3.5 degrees is the best that could be achieved up to now.

7 Maximum likelihood method

The idea for a maximum likelihood approach for a muon tracking with the inner veto arose by problems concerning the barycenter method. In the early phase of the studies on the barycenter reconstruction a time window of 30 ns was used as a default value. This time window causes a huge shift of the mean value of the ΔR-distribution to negative values, what is caused by more hits due to reflected light than for a shorter time window. The distribution for the entry point is shown in figure 7.1. As one can see the shift of the mean to negative values exceeds 200 mm and the width is also large with more than 300 mm.

entry: $\Delta R = R_{rec}-R_{true}$	
Entries	19906
Mean	-223.5 ± 2.368
RMS	334.1± 1.674
χ^2 / ndf	266.4 / 88
Constant	746.7 ± 6.9
Mean	-219.7 ± 2.2
Sigma	314.4 ± 1.9
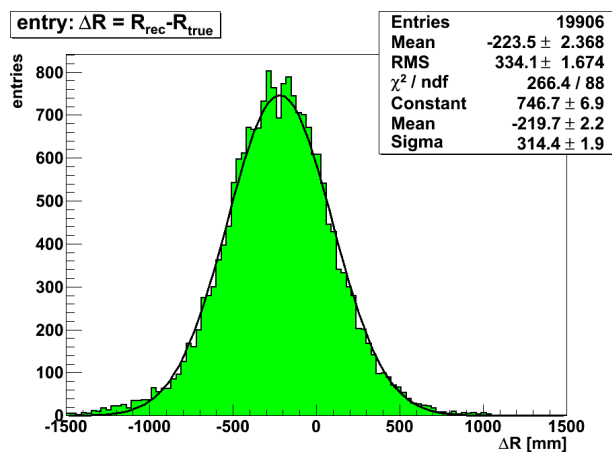
Figure 7.1: *Difference distribution for the radius coordinate for vertical muon reconstructed with the barycenter method. In contrast to the optimum parameter set as described in section 6.5 a time window of 30 ns was used here. This was the default configuration used in the early phase of the studies on a muon tracking with the inner veto. As one can see the shift of the mean to a negative value exceeds 200 mm.*

As described in the previous chapter the barycenter method mainly suffers from shadowing effects, which cause hits due to reflected light. Therefore, efforts were made to find a new method, which considers these hits in a more suitable manner. The approach was to find a correlation between the timing of the PMT hits and the distance to the true muon track and use this correlation for the reconstruction of the inner veto entry and exit points[1].

---

[1] The charge information is not directly used in the maximum likelihood reconstruction as the charge information can be distorted by saturation of the PMT pulses (see section 5.1). The charge is used for the PMT hit selection only.

In figure 7.2 two examples for plots, which were produced to improve the understanding regarding such a correlation, are depicted: figure 7.2a shows the PMT pulse start times plotted against the distance of the hits to the muon track for the top inner ring PMTs, which are watching radially outwards (TIo-PMTs). Figure 7.2b shows the same for the bottom outer ring PMTs, which are watching inwards and are not facing a buffer foot (BOiNF-PMTs). The distance was calculated to be the distance of the hit PMTs to the true entry and exit points in the corresponding x-y-plane at the top and the bottom mean PMT z-positions ($\bar{z}_{top} = 3178.75$ mm and $\bar{z}_{bottom} = -3170$ mm).

On both plots one can see that for an increasing distance to the muon track the earliest start times appear later. The sharp cut at distances slightly above 5000 mm for the TIo-PMT plot is caused by the fact, that the maximal distance in the x-y-plane is limited by the inner veto geometry. For the TIo-PMTs this results in a maximal distance of about 5050 mm and for the BOiNF-PMTs in a maximal distance of about 6100 mm.

The offset of the start times in the plots is due to an internal offset of 50 ns used by RoSS and the time the muon needs to propagate from the top to the bottom inner veto. The sharp cut at times above 250 ns is caused by the 256 ns time window of the channel read out [Nov09]. Furthermore, both plots show a stripy distribution of the points, which is caused by the 2 ns sampling rate of the ADCs (simulated by RoSS) [Nov09]. The points for start times above about 150 ns are due to reflected light. The few points below about 52 ns in figure 7.2a and below about 75 ns in figure 7.2b are caused by prepulses and accidental dark pulses, where the prepulses should dominate (see section 5.1).

The empty regions above the band of early hits at small distances (distances lower than ~ 1300 mm for the BOiNF-PMT plot and lower than ~ 500 mm for the TIo-PMTs) are partly caused by the smaller number of PMT hits in these regions, what also causes the lower density of prepulses. An additional explanation can be given by the small distance to the muon track: the PMT hits are mainly caused by direct light in this region, i.e. light, which has not been reflected. This also explains the smaller distance range with no points above the early hit band for the TIo-PMT plot: here this range ends above about 500 mm caused by the fact that the inner ring PMTs also see light from a muon passing behind the PMT. This light from behind is only seen by the PMT after being reflected repeatedly. This actually applies also for the distances smaller than 500 mm. As one can see this region is narrower for the BOiNF-PMT plot: these PMTs also see reflected light from muons passing behind them, but the number of these muons is much smaller as these PMTs are placed close to the inner veto wall. The broadening for distances of about 1300 mm is caused by shadowing of the inner veto PMTs and the buffer feet.

(a)

(b)
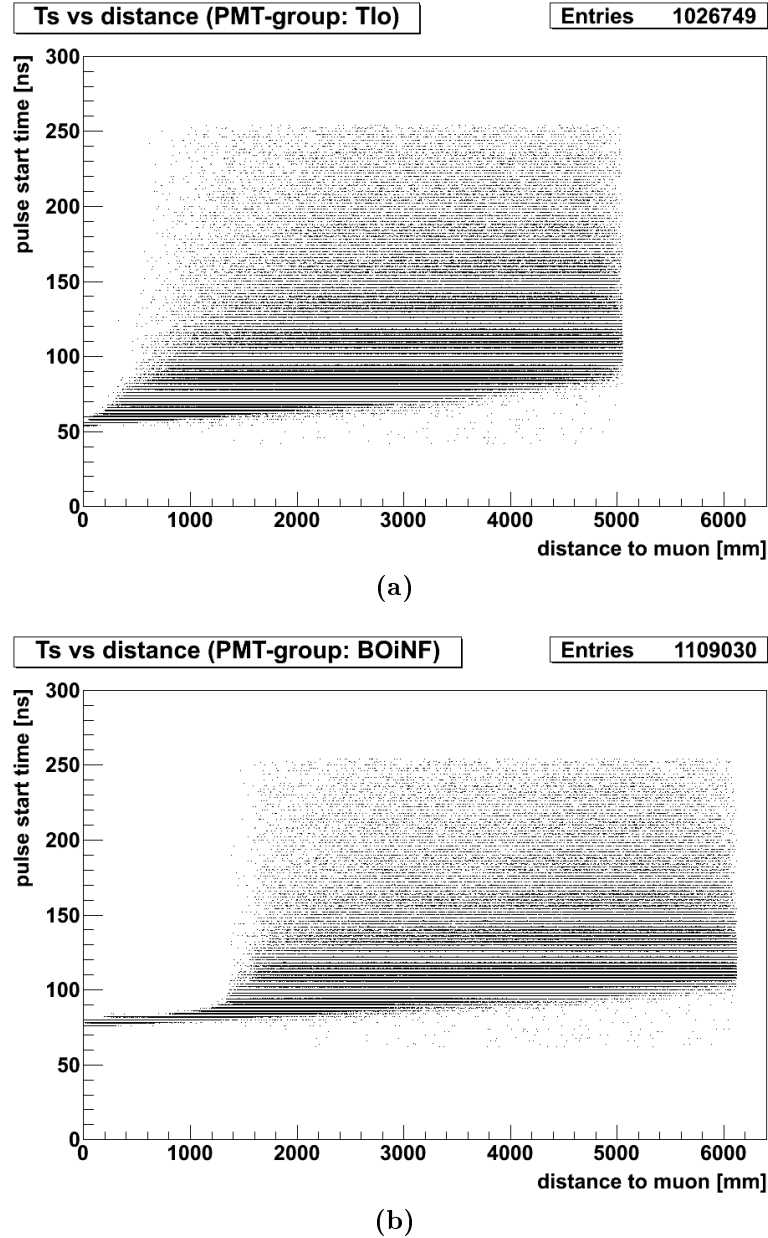
Figure 7.2: *The PMT pulse start times plotted against the distance of the hit PMT to the true muon track, i.e. the true entry or exit point, respectively (see section 5.2): (a) shows the plot for the top inner ring PMTs watching outwards (TIo) and (b) shows the plot for the bottom outer PMTs watching inwards, which are not facing a buffer foot (BOiNF). Both plots rely on the data of 280 000 simulated vertical 100 GeV muons. The offset of the start times in both plots is caused by the internal offset of 50 ns in RoSS. The stripy structure regarding the timing is due to the 2 ns sampling rate of the ADCs. The points below the main bands are mainly prepulses.*
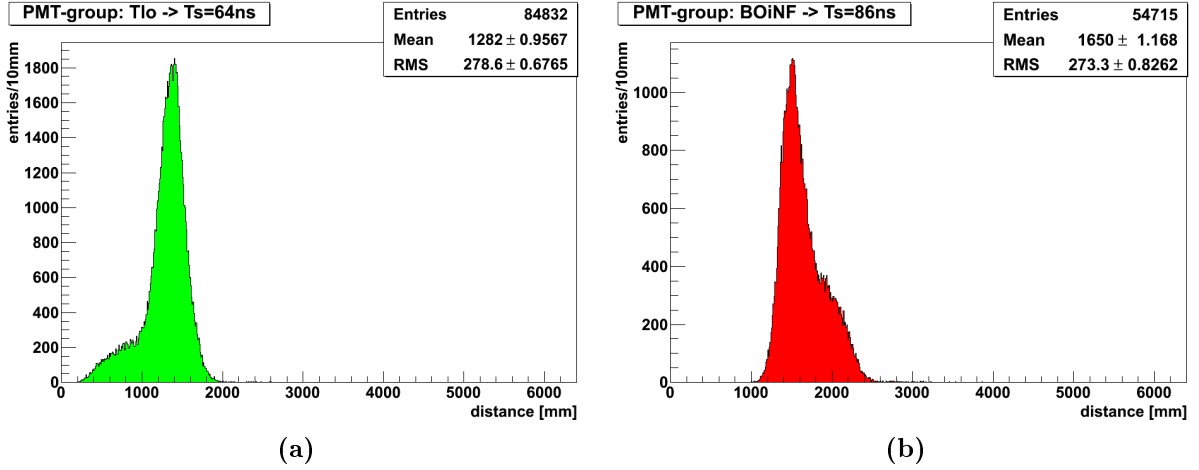
Figure 7.3: *Examples for PDHs: (a) for a start time of 64 ns for the TIo-PMTs and (b) for the BOiNF-PMTs for 86 ns. Both histograms rely on the data of 280 000 simulated vertical 100 GeV muons.*

7.1 The algorithm

7.1.1 Probability density histograms

The plots like the ones shown in figure 7.2 already contain the correlated information between the timing and the distance to the muon track. Therefore, the main idea of the maximum likelihood method is to use the distribution of points in these plots for a reconstruction of the inner veto entry and exit points. This was realized by filling the 2 ns stripes caused by the ADC sampling into histograms and use these as probability density functions in the reconstruction: the *probability density histograms* (PDHs).

In figure 7.3 two examples for PDHs are depicted. These histograms rely on the same muon data as the plots in figure 7.2. Figure 7.3a shows the distribution of the distances of the real muon track to the hit TIo-PMTs with a start time of 64 ns. The distribution has a main peak with a maximum at a distance of about 1400 mm. This peak is basically caused by direct light from muons passing the top inner veto in front of the TIo-PMTs. The shoulder at smaller distances is caused by light produced behind those PMTs, which has to be reflected several times to cause a hit in the corresponding PMT. As one can see, the histogram has no entries above about 2 m. This can be explained by the start time of 64 ns, which is related to a time difference to the first hit PMT at the top inner veto of about 6 ns to 10 ns[2]. In general, it can be assumed that the entries at largest distances in the PDHs are most likely due to hits caused by direct light. The entries at small distances can be interpreted as hits due reflected light, where this light was produced in regions, which are not directly in the line of sight of the PMT.

Figure 7.3b shows the distribution of the distances to the true muon track regarding the BOiNF-PMT hits with a start time of 86 ns. One can see a main peak with a

---

[2]Here again the RoSS internal start time offset of 50 ns and the muon propagation have to be considered.

maximum at about 1500 mm and a shoulder to larger distances, so the other way round as for the PDH for the TIo-PMTs: here the shoulder is due to direct light and the main peak due to reflected light. This is caused by the bottom inner ring PMTs and the buffer feet. Both the inner ring PMTs and the buffer feet are at a distance of roughly 1200 mm to the BOiNF-PMTs. Hence, light produced by muons passing behind the buffer feet or the inner ring PMTs (behind from the BOiNF-PMTs point of view) has to be reflected to be seen by the BOiNF-PMTs. Furthermore, one can see that the maximum distance to the muon track is about 2.5 m, what is caused by the start time of 86 ns, which is related to a time difference to the first hit bottom PMT of about 8 ns to 12 ns.

Here an advantage of using PDHs for a reconstruction appears: in contrary to the barycenter method the approach using PDHs for a reconstruction suffers less from reflected light. The information on the muon track is strongly distorted for reflected light as the resulting start times are larger and the charges are smaller. Hence, PMT hits due to reflected light look like hits caused by light produced at a larger distance than the actual one. In the barycenter method these hits are considered in an inaccurate manner (see section 6.1): here the contribution of hits due to reflected light could be reduced by applying a time window of 10 ns (see section 6.5), but this is connected with a loss of information as hits due to direct light appearing later than 10 ns after the first hit are not taken into account. In the PDHs reflected light is considered in a more suitable way as the related pulse start times appear at the corresponding true distance. This is nicely demonstrated by the PDH in figure 7.3b, where the contribution of hits from reflected light dominates.

7.1.2 PDH production and PMT subgroups

To obtain the additional information about the distance of the hits to the muon track the PDHs have to rely on data from simulations. Therefore, the PDHs, which will be used in the final version of the reconstruction, have to rely on a simulation, which is as close as possible to reality.

As mentioned before, the PDHs are produced for different hit start times in steps of 2 ns. Due to the symmetric arrangement of the top and bottom inner veto PMTs it is not necessary to produce the PDHs for each single PMT. The PDHs can be produced for certain subgroups, which contain PMTs of the same ring and with the same viewing direction (see figures 2.6 to 2.8). Therefore, the number of simulated muons needed can be reduced significantly without reducing the statistics.

In sum there are four subgroups for the top inner veto PMTs and five subgroups for the bottom PMTs[3]. The bottom outer ring PMTs watching inwards were classified into two additional subgroups: the PMTs facing a buffer foot and the ones, which do not face a buffer foot. As described in sections 6.4 and 6.6 the buffer feet had some effects on the barycenter calculation. All subgroups for the top and the bottom inner veto PMTs are summarized in table 7.1.

---

[3]The PMTs at the side wall are not used in the maximum likelihood method. Therefore, no PDHs are needed for these.

PMT ring / viewing direction	top		bottom	
	inner ring	outer ring	inner ring	outer ring
inwards	6 TIi	6 TOi	6 BIi	–
outwards	6 TIo	–	12 BIo	–
downwards	–	6 TOd	–	–
upwards	–	–	–	12 BOu
inwards facing no foot	–	–	–	6 BOiNF
inwards facing foot	–	–	–	6 BOiF

Table 7.1: *The top and bottom inner veto PMT subgroups with the number of PMTs per group and their abbreviations.*

7.1.3 Using PDHs for the reconstruction

As the barycenter reconstruction the maximum likelihood method reconstructs an inner veto entry point from the top PMT hits (PMTs 390 to 413) and an inner veto exit point from the bottom PMT hits (PMTs 426 to 467). These points are reconstructed in the x-y-planes at the top and bottom mean PMT z-positions as the PDHs rely on distances calculated in those planes. Again the reconstructed muon momentum direction $\hat{p}_{rec}$ is calculated from these two reconstructed points using equation 6.1.

The PDHs can be written as distributions $N_i(d)$, where d is the distance in the x-y-plane to the hit PMT i and $N_i(d)$ the number of entries in the bin related to d. Therefore, the probability $p_i(d)$ that a muon passed the inner veto in a distance d to the hit PMT i can be calculated as follows:

$$p_i(d) = \frac{N_i(d)}{N_{PDH,i}} \tag{7.1}$$

where $N_{PDH,i}$ is the total number of entries in the PDH for the hit PMT i.

The inner veto entry and exit point are reconstructed by a scan of the x-y-planes at the top and bottom mean PMT z-positions. For each step (x, y) of the scan the distance $d_i(x, y)$ to each contributing hit PMT i is calculated (for details on the hit selection see section 7.1.5), where the photocathode's center of mass is used for the PMT-coordinates. This results in probabilities $p_i(d_i(x, y))$ for all contributing hits:

$$p_i(d_i(x, y)) = p_i(x, y) = \frac{N_i(d_i(x, y))}{N_{PDH,i}} \tag{7.2}$$

The total probability $P(x, y)$ for a muon, which passed the inner veto at the current step (x, y), is calculated to be the product of all probabilities $p_i(x, y)$:

$$P(x, y) = \prod_i p_i(x, y) \tag{7.3}$$

The (x, y) pair with the largest total probability $P(x, y)$ is then taken as the reconstructed entry or exit point, respectively. For the reconstructed z-coordinate the top and bottom mean PMT z-positions are used.

7.1.4 The way of scanning in x and y

As mentioned before the maximization of the total probability $P(x, y)$ is performed by scanning the x-y-planes at the top and bottom mean PMT z-positions with a certain step size in x and y. This scan can be performed in different ways. The conservative approach is to scan the whole x-y-plane within the inner veto tank, i.e. the radius $R = \sqrt{x^2 + y^2}$ is always smaller or equal $3250\,\mathrm{mm}$. In the algorithm this is realized with a step size of $10\,\mathrm{mm}$ as the bin size of the PDHs is also set to $10\,\mathrm{mm}$. The advantage is that this conservative scan determines the maximal probability with the highest possible reliability, but the problem is that it is very slow.

A first approach to increase the speed of the reconstruction was to scan only a certain area around the first hit PMT - again for the top and the bottom separately. The acceleration of the reconstruction is obvious as the number of (x, y) pairs is reduced. The ranges for the top and the bottom scan were optimized regarding the speed and the performance of the reconstruction. For the top the optimum range was found to be $\Delta x = \Delta y = 1600\,\mathrm{mm}$, where it is scanned in $x_{PMT} \pm \Delta x$ and $y_{PMT} \pm \Delta y$. The optimum range for the exit point reconstruction could be determined to be $\Delta x = \Delta y = 1800\,\mathrm{mm}$. Again, all (x, y) pairs have to lie within the inner veto and the step size was chosen to be $10\,\mathrm{mm}$.

A further acceleration of the reconstruction could be achieved by a scan in two steps: first a coarse scan with a step size of $100\,\mathrm{mm}$ is performed (either conservatively or in a range around the first hit PMT). Then a fine scan in a range around the (x, y) pair with the maximum total probability $P(x, y)$ in the rough scan is done with a step size of $10\,\mathrm{mm}$. This range was also optimized for the top and the bottom scan regarding speed and performance. The optimal fine scan ranges were found to be $500\,\mathrm{mm}$ for the top and $700\,\mathrm{mm}$ for the bottom.

All plots in this theses regarding the performance of the maximum likelihood reconstruction rely on the double scan method.

7.1.5 The PMT hit selection

As for the barycenter method the PMT hits contributing to the reconstruction are selected by a time window and a charge threshold (see section 6.2 and 6.2). In addition to this selection, start time limits for the first PMT hits at the top and the bottom are defined. This is necessary as there are only PDHs available in certain time ranges for the top and the bottom. For all reconstruction results presented in this thesis a time limit of $110\,\mathrm{ns}$ for the hits at the top and a time limit of $130\,\mathrm{ns}$ for the hits at the bottom inner veto have been used.

The PMT hits contributing to the PDHs are also selected using a charge threshold. This charge threshold is always chosen to be the same as the one used for the reconstruction to eliminate the influence of the hits with smaller charges than the threshold used for the reconstruction.
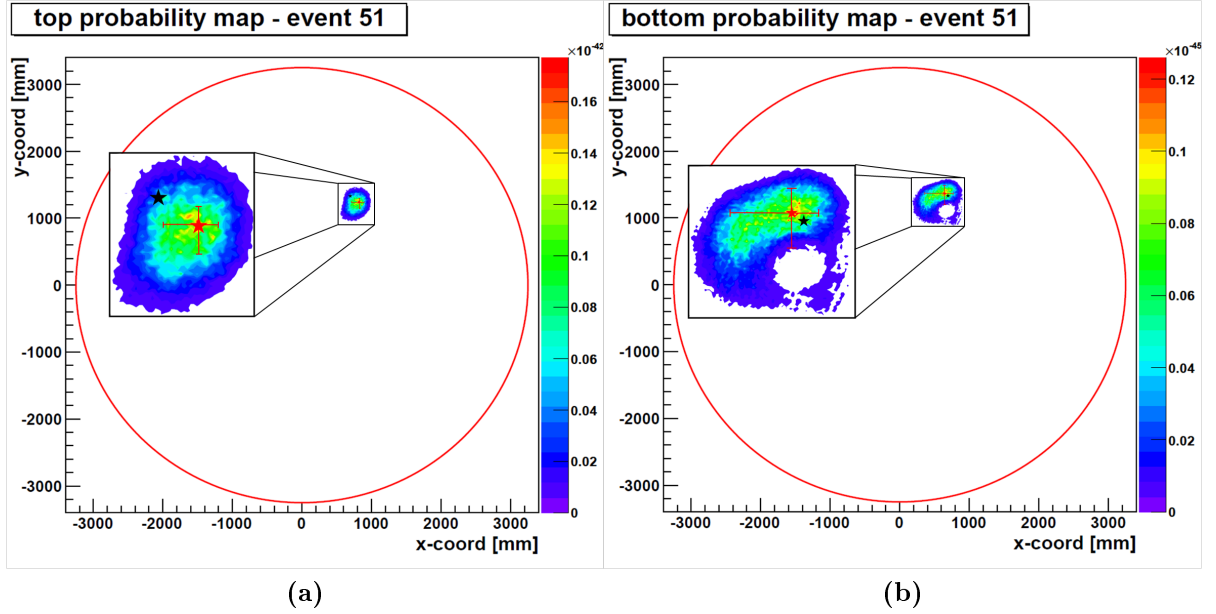
Figure 7.4: *Maps of the total probability $P(x, y)$ for the top and bottom x-y-planes (for a vertical muon) with a zoomed image of the interesting region. The different colours correspond to different probabilities. The black stars indicate the true inner veto entry and exit points, while the red stars show the reconstructed entry and exit points, i.e. the (x, y) with maximum $P(x, y)$. The error bars correspond to the maximum and minimum x- and y-coordinates on the 1σ-contour. The red circle shows the position of the inner veto side wall.*

7.1.6 Probability maps and error estimation

In figure 7.4 maps of the total probability $P(x, y)$ for the x-y-scans at the top (figure 7.4a) and bottom inner veto (figure 7.4b) are depicted for a typical event generated by a vertical muon. As one can see the regions with a probability $P(x, y) > 0$ are concentrated in a relatively small area for both the top and the bottom probability map: this region has a diameter of about 500 mm for the top and about 700 mm for the bottom x-y-plane.

In both probability maps error bars for the reconstructed points are shown. The errors for the entry and exit points reconstructed by the maximum likelihood method are estimated as described in the following: the total probability $P_{s\sigma}$ on the contour, which defines the extreme limits for the s standard deviation errors for x and y, is given by [PDG10]

$$\ln P_{s\sigma} = \ln P_{max} - \frac{s^2}{2} \tag{7.4}$$

where $P_{max} = \max\{P(x, y)\}$. Therefore, the total probability corresponding to one standard deviation (1σ) is

$$P_{\sigma} = P_{max} \cdot e^{-\frac{1}{2}} \tag{7.5}$$

The errors for the x- and y-coordinates of the reconstructed entry and exit point are determined by the smallest rectangle, which includes all points (x, y) with a probability $P(x, y) \geq P_\sigma$.

As one can see, the bottom probability map shows a void in the region with non-zero $P(x, y)$ area with a diameter of about 200 mm. This is caused by a hit PMT, which is located at the center of this void. This PMT hit has a start time, which corresponds to a PDH with no entries for the distance range from 0 to about 200 mm. Therefore, all scanned (x,y) pairs with a distance of 200 mm to this PMT result in $P(x, y) = 0$. This probability map shows that the errors determined as described above ensure that all (x,y) pairs with a total probability larger than P_σ lie within the range of the errors. This is even then the case, when two separated areas with finite $P(x, y)$ appear.

7.2 Performance for vertical muons

The maximum likelihood reconstruction was first tested with simulated vertical muons with an energy of 100 GeV as described in section 4.3. 280 000 of the simulated vertical muons were used to produce the PDHs. All plots, which will be shown in this section, rely on reconstructions of the same 20 000 muons.

7.2.1 Reconstruction parameter configuration

As described in section 7.1.5 the PMT hits used to reconstruct the inner veto entry and exit points are selected in the same way as for the barycenter reconstruction using a charge threshold q_{thresh} and a time window t_{window} (and two time thresholds, which are not meant to be varied). Therefore, the reconstruction was tested for different values for q_{thresh} and t_{window}.

Again the difference distributions as described in section 6.3 were used to characterize the goodness of the reconstruction. The parameters of interest are the width of the distributions for ΔX and ΔY, the shift of the mean of the ΔR-distribution to negative values and the mean value of the distribution for the angle between the reconstructed and the true muon momentum direction. Furthermore, the shift of mean for the radius difference distribution should be small, as well as the mean of the distribution for the angle between the true and reconstructed muon momentum direction, which is always larger than zero.

First the influence of the time window on the reconstruction was tested for $t_{window} = 10, 20$ and 30 ns, where $q_{thresh} = 1$ pe was fixed. Figure 7.5 shows the plots regarding the above mentioned criteria for the goodness of the reconstruction. The best performance of the reconstruction concerning the width of the ΔX-distribution and the mean angle between $\hat{p}_{true}$ and $\hat{p}_{rec}$ could be reached for a time window $t_{window} = 30$ ns. Therefore, this time window is used as the best performance t_{window} in the following.

One can see that the width of the ΔX-distribution for the entry point, indicated by the RMS of the histogram (see figure 7.5a), increases for an decreasing time window by more than 40 mm. This is not observed for the exit point reconstruction, where the
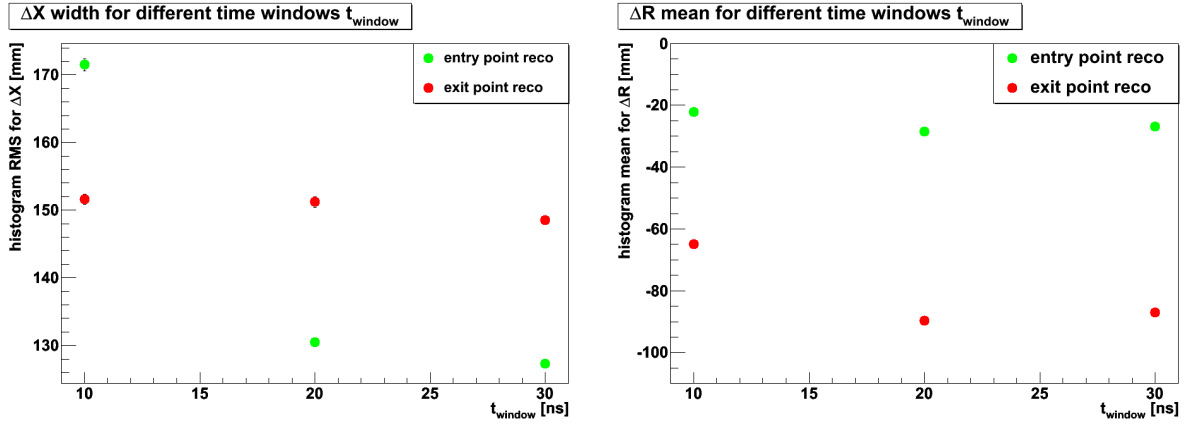
(a) ΔX-distribution width as indicated by the histograms RMS for **different time windows** t_{window} (fixed $q_{thresh} = 1\,pe$).

(b) ΔR-distribution mean as indicated by the histograms mean value for **different time windows** t_{window} (fixed $q_{thresh} = 1\,pe$).
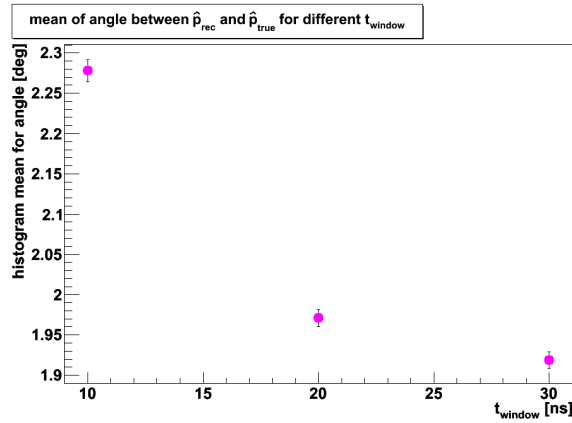
(c) Mean values of the distributions of the angle between $\hat{p}_{true}$ and $\hat{p}_{rec}$ for **different time windows** t_{window} (fixed $q_{thresh} = 1\,pe$).

Figure 7.5: *The behaviour of the maximum likelihood reconstruction for different time windows t_{window} of 10, 20 and 30 ns. The best results are obtained for a time window of $t_{window} = 30\,ns$.*

width is relatively constant. An explanation for this contrary behaviour may be given by the larger number of PMTs at the bottom inner veto. A smaller time window basically reduces the contributing PMT hits to those in a restricted range around the incident muon. Therefore, reducing t_{window} has a smaller effect on the bottom inner veto than on the top inner veto, where for example only half as much outer ring PMTs are as at the bottom.

Regarding the shift of the ΔR-distributions mean to negative values (figure 7.5b) both the entry and the exit point reconstruction perform in a similar way: the shift is reduced for a time windows of 10 ns, where the shift is almost constant for time windows of 20 and 30 ns. The smaller shift for $t_{window} = 10$ ns may be explained by the reduced region around the muon track in which PMT hits contribute to the reconstruction. This already caused some features regarding the barycenter reconstruction, for example the large void for the reconstructed entry points at small x and y. For the maximum likelihood method there may be a similar effect due to the restricted range around the true muon track, which is still not understood, but causes a shift to larger radii.

The behaviour for the reconstruction of the momentum direction can be seen in figure 7.5c. Here the histogram mean value for the distribution of the angle between the true $\hat{p}_{true}$ and the reconstructed momentum direction $\hat{p}_{rec}$ is plotted against the time window size. One can see that the mean value of the distribution decreases from almost 2.3 degree to less than 1.95 degree for an increasing size of the time window. Furthermore, the behaviour looks similar to that for the width of the ΔX-distribution for the entry point reconstruction. This behaviour can be expected as the precision of the reconstructed muon momentum obviously depends on the precision of reconstructing the entry and the exit point.

The maximum likelihood reconstruction was also tested with different charge thresholds of 1, 10, 20 and 50 pe. As mentioned before in section 7.1.5 the PDHs used for the reconstruction are always produced by selecting the contributing PMT hits with the same charge threshold as the one used for the reconstruction. Figure 7.6 shows the behaviour of the reconstruction regarding the width of the difference distribution of the x-coordinate for the entry and exit points (figure 7.6a), the shift of the mean of the distribution of ΔR for the entry and exit points (figure 7.6b) and the mean value of the distribution of the angle between the true and the reconstructed momentum direction (figure 7.6c).

As one can see the width for the ΔX-distribution of the entry and exit points is rather constant for $q_{thresh} = 1$ pe and $q_{thresh} = 10$ pe. Then the width rises for an increasing q_{thresh} for the entry and the exit points. This rise can be explained by the PDHs, which were produced with the same threshold. Therefore, the PDHs have less entries for larger q_{thresh} as the threshold reduces the PMT hits contributing to the PDHs.

In figure 7.6b one can see that the shift of the mean ΔR to negative values decreases for an increasing threshold. The reducing radius shift is not understood, yet, but the effect might have the same source as the effect for the time window as the charge threshold also basically reduces the number of the PMT hits contributing to the reconstruction.

The mean of the distribution for the angle between the true and the reconstructed
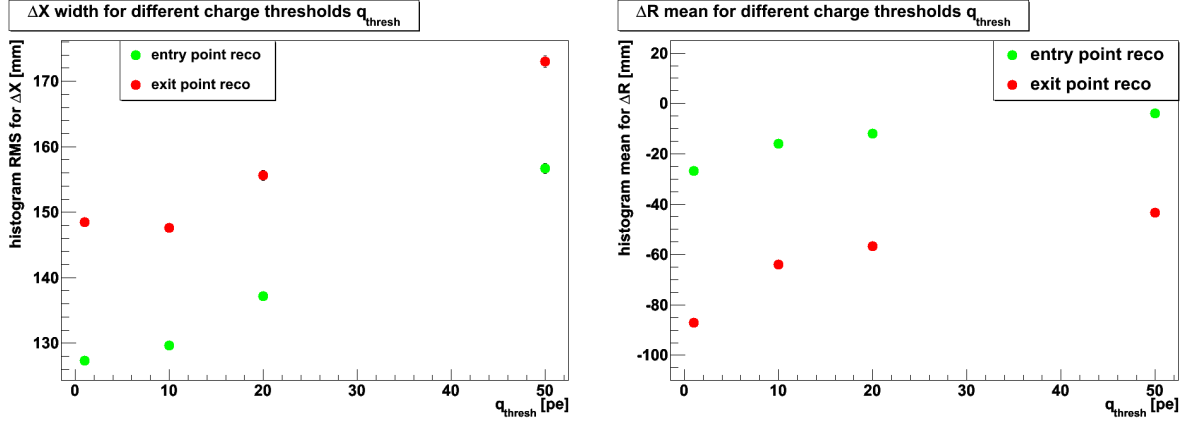
(a) ΔX-distribution width as indicated by the histograms RMS for **different charge thresholds** q_{thresh} (fixed $t_{window} = 30\,ns$).

(b) ΔR-distribution mean as indicated by the histograms mean value for **different charge thresholds** q_{thresh} (fixed $t_{window} = 30\,ns$).
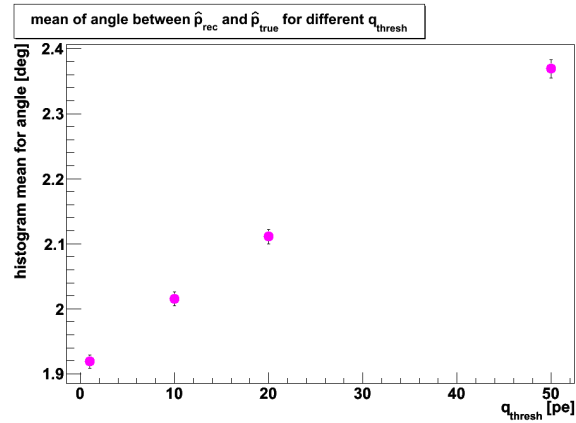
(c) Mean values of the distributions of the angle between $\hat{p}_{true}$ and $\hat{p}_{rec}$ for **different charge thresholds** q_{thresh} (fixed $t_{window} = 30\,ns$).

Figure 7.6: *The behaviour of the maximum likelihood reconstruction for different charge thresholds q_{thresh} of 1, 10, 20 and 50 pe. The best results are obtained for a charge threshold of $q_{thresh} = 1\,pe$.*

momentum direction (figure 7.6c) increases for larger charge thresholds and is minimal for $q_{thresh} = 1\,pe$. From the almost constant widths of the ΔX-distributions for small thresholds one might expect a similar behaviour for the reconstructed momentum direction. This is not the case, even if the difference between the mean angles between $\hat{p}_{rec}$ and $\hat{p}_{true}$ for $q_{thresh} = 1\,pe$ and $q_{thresh} = 10\,pe$ is only about 0.1 degree. This small difference must be caused by the different radius shifts for both thresholds.

As the reconstruction of the momentum direction performs best for a charge threshold $q_{thresh} = 1\,pe$ the final set of parameters used is $q_{thresh} = 1\,pe$ and $t_{window} = 30\,ns$. Therefore, the PDHs used for the reconstruction contain only data from hits with a charge above $1\,pe$. All plots in the following regarding the performance of the method for vertical muons rely on a reconstruction with this parameter set (figures 7.7 to 7.14).

7.2.2 Entry point reconstruction

In figure 7.7 the true and reconstructed entry points are depicted in the x-y-plane. One can see the following main characteristics in the plot for the reconstructed points:

- **Homogeneous distribution of the points:** Compared to the barycenter method the entry points reconstructed by the maximum likelihood method are distributed much more homogeneously. Therefore, an improvement could be achieved as the distribution of the reconstructed points is more similar to the distribution of the true entry points.

- **Void at the center:** As for the barycenter method the distribution of the reconstructed entry points shows a void at small x and y caused by the chimney. Compared to the barycenter method this void is much smaller. Few reconstructed points appear within the void as the current version of the reconstruction does not forbid reconstructed entry points within the chimney .

- **Voids at PMT positions:** In figure 7.7b one can see six voids at large radii and twelve voids at medium radii, where the latter cannot be seen that precisely in some cases. These voids were not vilsible for the barycenter method and are caused by the PDHs. As it could be seen for the two examples for PDHs in figure 7.3 the histograms can have zero entries for small distances. Only the PDHs for the earliest start times show entries at the smallest distances. PMT hits close to the muon track may appear slightly later due to the $2\,ns$ sampling and the $2\,ns$ jitter (see section 4.2.2). Therefore, the corresponding PDHs have no entries for small distances up to about $200\,mm$ causing $P(x, y) = 0$ in a range around the hit PMT.

  An explanation for the appearance of only six voids at large radii, while there are twelve PMTs at the top outer ring, can be given by the viewing direction. The voids occur for the outer ring PMTs watching inwards. The PDHs for the downwards watching PMTs show no or just a small region with no entries at small distances.
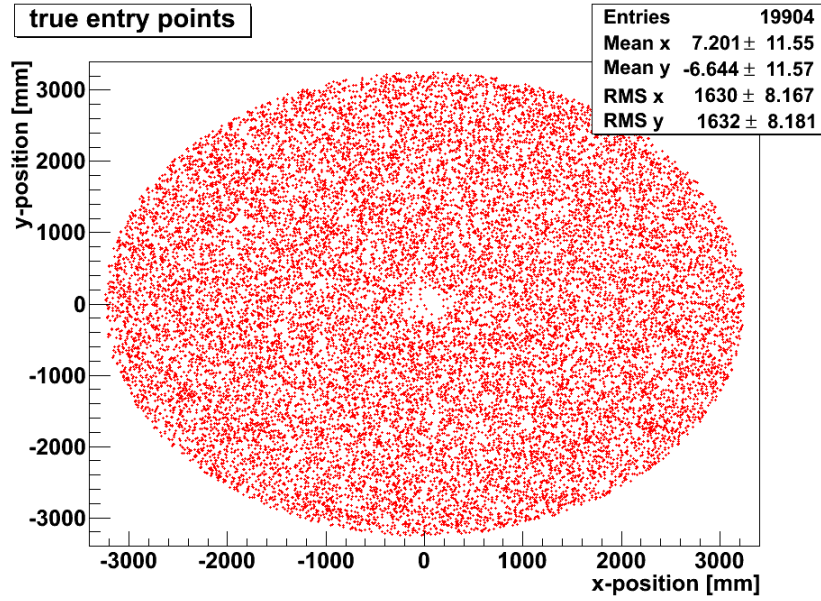
(a) True entry points
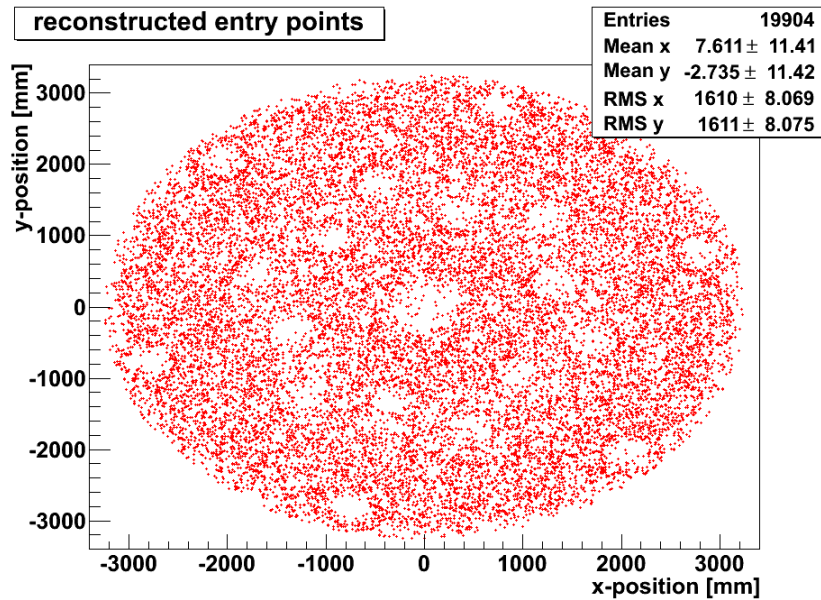
(b) Reconstructed entry points

Figure 7.7: *The true (a) and reconstructed (b) entry points in the x-y-plane at the top PMT mean z-position for 20 000 vertical 100 GeV muons (the missing muons were either contained in the chimney or were not reconstructed as no $P(x, y) > 0$ could be found). The void at the center of both the true and the reconstructed points plot is caused by the chimney. Compared to the barycenter method the distribution of the reconstructed points is much more homogeneous. The voids at the PMT positions for the reconstructed points is caused by the PDHs.*
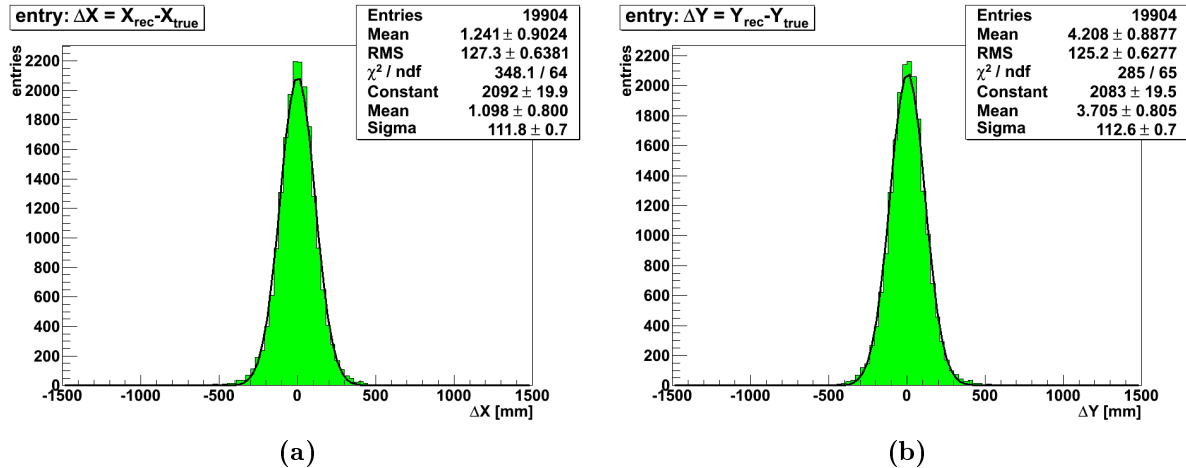
Figure 7.8: *Difference distributions for the x- and y-coordinate of the entry point for vertical 100 GeV muons. The distributions were fitted with a Gaussian to visualize the degree of symmetry.*

Figure 7.8 shows the distributions of the difference between the reconstructed and the true x- and y-coordinates for the inner veto entry points. As one can see the widths of both distributions are much smaller compared to that for the corresponding distributions for the barycenter reconstruction. The widths indicated by the histograms RMS are about 125 mm and the widths indicated by the σ of the Gaussian fit about 112 mm and hence, more than a factor of two better than the ones for the barycenter reconstruction. Both distributions are symmetric and centered very closely to zero. The small deviations from the Gaussian shape may be caused by the voids around the PMT positions mentioned in the list above. Furthermore, one can see a slightly lower density of reconstructed entry points at radii larger than about 3000 mm compared to the plot for the true entry points (see figure 7.7). This indicates a shift to smaller reconstructed radii for muons passing at large radii.

Figure 7.9 shows the distributions for ΔR and $\Delta\phi$ for the entry points. Regarding the distribution for the radius (figure 7.9a) one can see that there is a small shift of the mean by less than 30 mm to a negative value. This shift is by more than a factor of two smaller than the shift of the corresponding plot regarding the barycenter method. The distribution also shows a small asymmetry indicated by the entries at $\Delta R < -300$ mm. Both characteristics should be caused by the slightly lower density of the reconstructed entry points at large radii.

Like for x and y the distribution for the polar angle ϕ (figure 7.9b) is symmetric and centered closely to zero, but here the Gaussian fit is worse. The cause is that the determination of the polar angle gets less precise for small radii, what was already the cause for the shape of the corresponding distributions regarding the barycenter reconstruction. The width of the distribution as indicated by the RMS of the histogram is about 3.9 degree, what is about a factor of two better than for the barycenter method (see figure 6.5b).
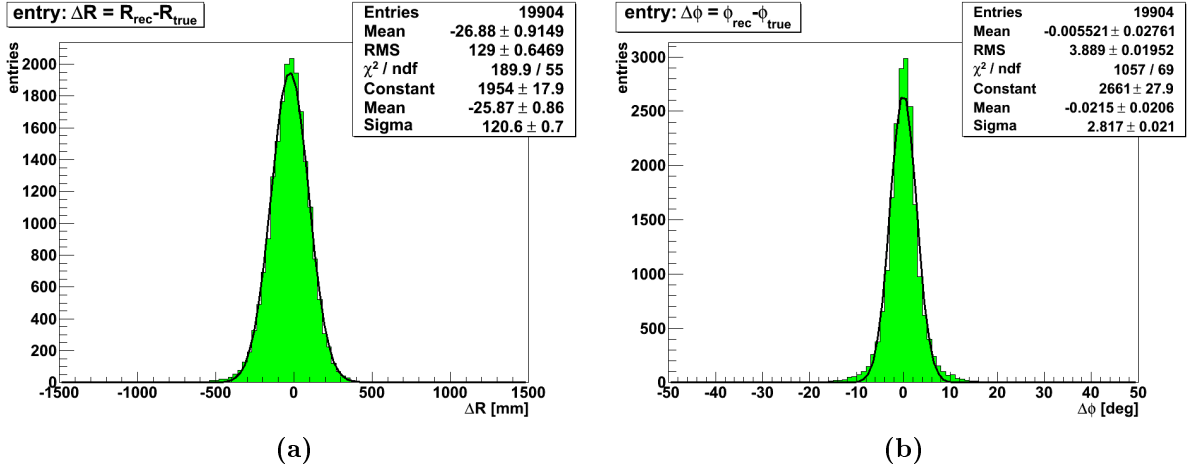
Figure 7.9: *Difference distributions for the R- and φ-coordinate of the entry point for vertical $100\,GeV$ muons. The distributions were fitted with a Gaussian to visualize the degree of symmetry.*

7.2.3 Exit point reconstruction

Figure 7.10 shows the true and the reconstructed exit points for the 20 000 vertical muons. The plot for the true exit points shows no voids and all 20 000 muons could have been reconstructed. The distribution of the reconstructed exit points shows the following features:

- **Voids at PMT positions:** As for for the reconstructed entry points one can see voids at the positions of the bottom inner veto PMTs. These voids are not as defined as the voids for the entry points, but especially for medium radii one can see that there are six regions where the density of the points is reduced significantly. There are twelve voids corresponding to the outer ring PMTs watching inwards. These are relatively small and arranged like the hours on a clock. The voids have the same explanation as the ones for the entry points. The explanation for the smaller voids is that the ranges with no entries at small distances are smaller than the ones in the PDHs for the top PMTs.

- **Low density of points for R > 3000 mm:** Comparing the plot for the true exit points and the plot for the reconstructed exit points one can see that the density of points at radii larger than about 3000 mm are reduced significantly. Furthermore, one can recognize regions between the 12 voids at the BOi-PMT positions where the density of points is slightly increased. These are due to voids caused by the 12 outer ring PMTs watching upwards. The reason for the lower density at large radii is not fully understood, yet, but can partly be explained by the voids at the outer ring PMT positions.

- **No hint for the buffer feet:** In contrary to the barycenter reconstruction this plot does not show voids caused by the buffer feet (see figure 6.6b). Here, one can
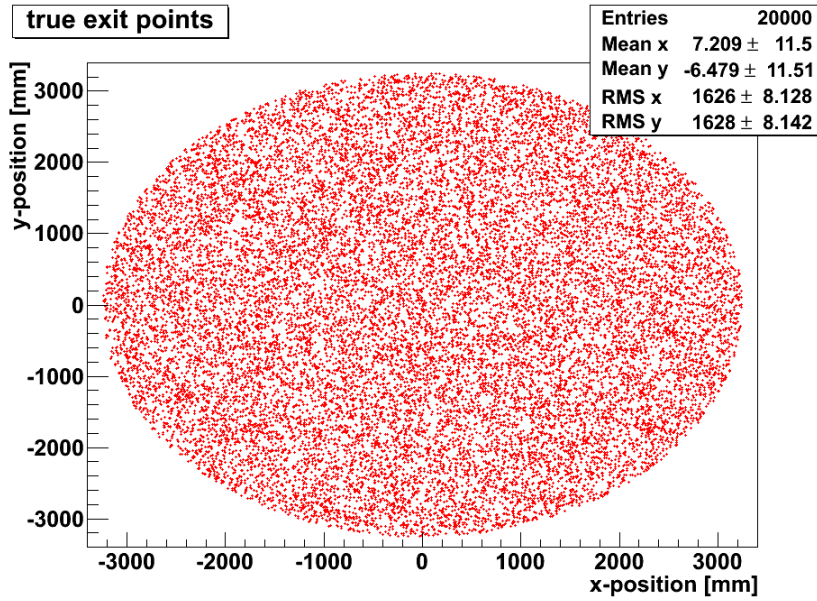
(a) True exit points
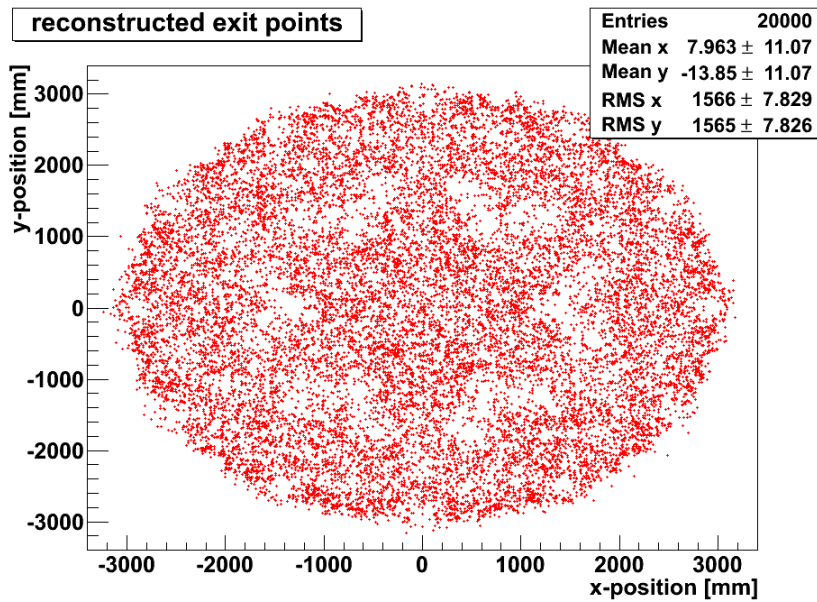
(b) Reconstructed exit points

Figure 7.10: *The true (a) and reconstructed (b) exit points in the x-y-plane at the bottom PMT mean z-position for* 20 000 *vertical* 100 *GeV muons. The voids at the PMT positions for the reconstructed points is caused by the PDHs. The same effect partly explains the low density of reconstructed points at R > 3000 mm. Combared to the barycenter method here no voids due to the buffer feet appear as the use of PDHs considers hits due to reflected light in a more suitable way.*
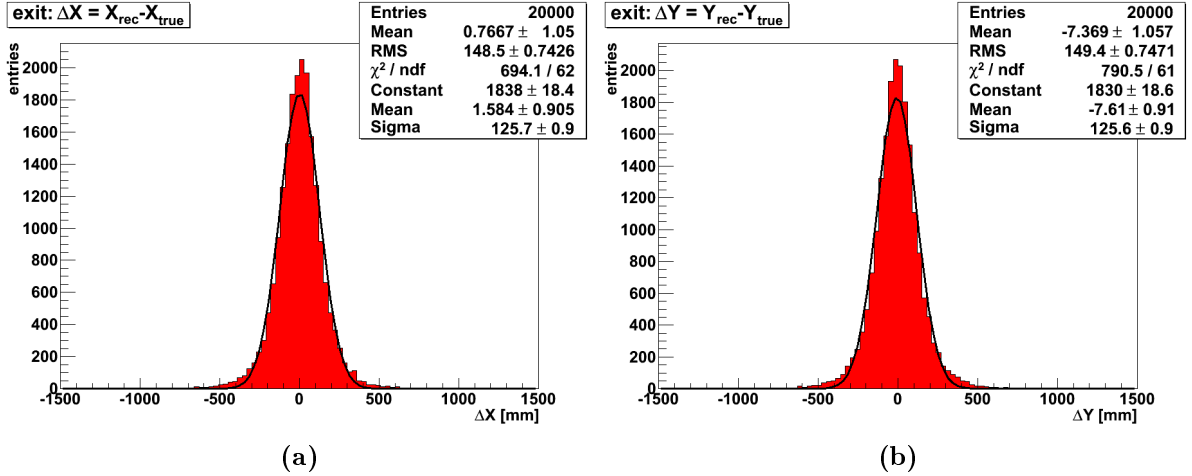
Figure 7.11: *Difference distributions for the x- and y-coordinate of the exit point for vertical 100 GeV muons. The distributions were fitted with a Gaussian to visualize the degree of symmetry.*

see the voids at the PMT positions and a homogeneous distribution of points in the vicinity of the buffer feet. This can be explained by using the PDHs for the reconstruction. This has the advantage that the information about the muon track is not lost, when the light is reflected. Therefore, the muons passing the inner veto near or inside a buffer foot can be reconstructed with relatively good precision.

The distributions of ΔX and ΔY (figure 7.11) have significantly smaller widths than the corresponding ones for the barycenter reconstruction. The RMS of the histograms indicate widths of about 150 mm and the σ of the Gaussian fit a width of about 125 mm. Both are by about 100 mm smaller than the ones for the barycenter method.

The distribution of ΔR (figure 7.12a) shows a shift of the mean value to negative values by almost 90 mm and is rather asymmetric. A shift of the mean value could be expected by the low density of reconstructed exits at large radii. This is also thought to be the source for the asymmetry: the muons with true exit points at large radii are reconstructed with a lower radius. Therefore, these muons appear in the ΔR-distribution at negative ΔR.

Figure 7.13 shows a scatter plot for ΔR versus the true radius of the exit point of the muon track R_{true}. One can see that the muons are reconstructed to a smaller radius than the true radius with $\Delta R < -30$ mm basically in two regions: a region at medium R_{true} between about 1200 mm and 1700 mm and a region for $R_{true} > 2800$ mm. In the first region at medium R_{true} the inner ring PMTs are located. Hence, this shift has to be caused by the voids at the positions of these PMTs. The second region at $R_{true} > 2800$ mm reflects the lower density of points at large radii in figure 7.10b. In this region the outer ring PMTs are located - the radius of the positions of the BOi-PMTs is about 2900 mm. For $R_{true} > 2800$ mm the whole ΔR distribution drifts increasingly to negative values. This again is an argument for the explanation that the voids cause the
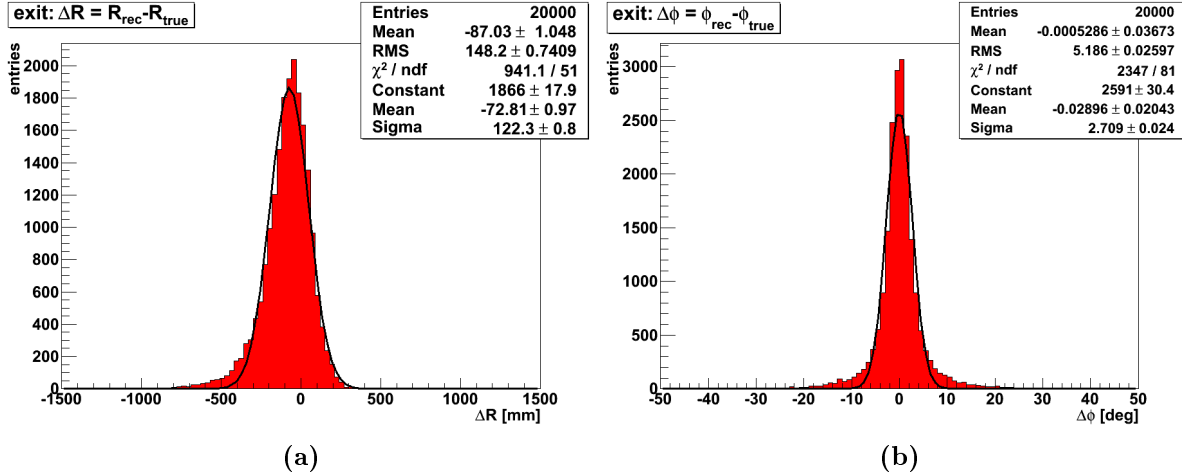
Figure 7.12: *Difference distributions for the R- and φ-coordinate of the exit point for vertical $100\,GeV$ muons. The distributions were fitted with a Gaussian to visualize the degree of symmetry.*

shift to smaller radii. The effect causing the voids does not allow reconstructed points in the vicinity of the outer ring PMTs. As there are 24 outer ring PMTs at the bottom inner veto it may happen for certain muon events with $R_{true} > 2800\,mm$ that $P(x,y) = 0$ for all points with $R > 2800\,mm$. As a result the algorithm reconstructs the exit points of these muons shifted inwards.

Figure 7.12b shows the distribution of $\Delta\phi$ for the exit points of vertical muons. Compared to the corresponding plot for the barycenter reconstruction (see figure 6.8b) the width of this distribution is about a factor of two smaller.

7.2.4 Reconstructed momentum direction

As for the barycenter method the reconstructed momentum direction of the muons is calculated from the reconstructed entry and exit point (see equation (6.1)). In figure 7.14 the distribution of the angle between the true $\hat{p}_{true}$ and the reconstructed momentum direction $\hat{p}_{rec}$ is depicted. The maximum of this distribution is at 1.5 degree, what is considerably smaller than the value for the barycenter reconstruction (see figure 6.9) of 2.5 degree. The better performance in the reconstruction of the momentum direction could be expected as both the entry and the exit points are reconstructed more precisely by the maximum likelihood method.
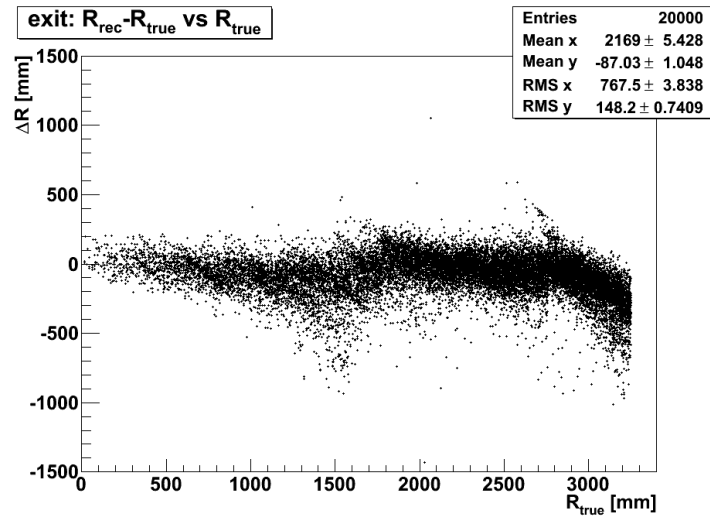
Figure 7.13: *Scatter plot for $\Delta R = R_{rec} - R_{true}$ versus the true exit point radius R_{true} for 20 000 vertical 100 GeV muons. The density of points increases for increasing ΔR as the muons are started uniformly distributed on a circle area. Therefore, the number of muons at a radius R is proportional to R^2.*
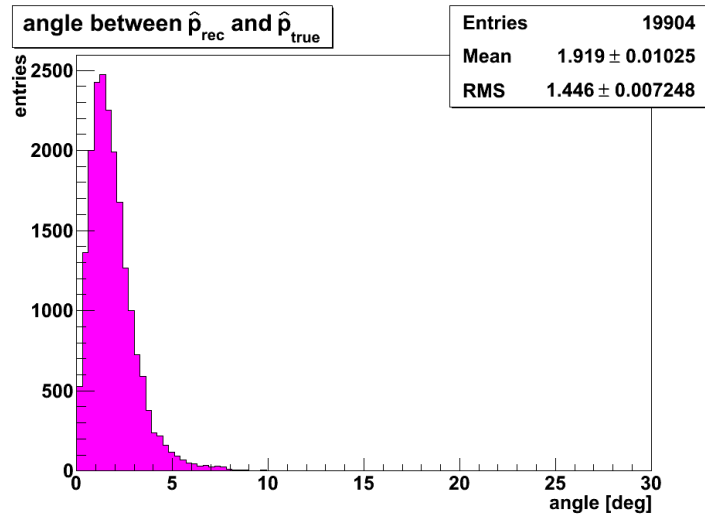
Figure 7.14: *The distribution of the angle between the true primary momentum direction $\hat{p}_{true}$ and the reconstructed momentum direction $\hat{p}_{rec}$ for vertical 100 GeV muons (angle in degree (deg)).*

7.3 Performance for inclined muons

The maximum likelihood reconstruction was also tested with the simulated inclined 100 GeV muons (see section 4.4). In sum, 550 000 muons were simulated, where 500 000 are used for the production of the PDHs. The remaining data from 50 000 muons is meant to test the reconstruction and is the same muon data, which was used to test the barycenter method. The set of parameters used for the plots in the following is (figures 7.15 to 7.29 except figures 7.19 and 7.24): $t_{window} = 30\,\mathrm{ns}$ and $q_{thresh} = 1\,\mathrm{pe}$.

7.3.1 Entry point reconstruction

Figure 7.15 shows the true and the reconstructed entry points. The plot for the true entry points (figure 7.15a) again shows a void at the center, which is caused by the chimney. The reduced density of points at radii $R > 3000\,\mathrm{mm}$ is caused by the way of simulating the inclined muons as described in section 4.4.

In figure 7.15b one can see that the reconstructed entry points are again distributed quite homogeneously and show similar characteristics as for the vertical muons:

- **Void at the center:** Again one can see the void at the center, which is caused by the chimney.

- **Voids at PMT positions:** One can again recognize voids at the positions of the PMTs due to empty bins at small distances in the PDHs. Compared to the plot regarding the vertical muons (see figure 7.7b) the voids can be seen even better as more points contribute to the plot (six voids for TOi-PMTs and twelve voids at the positions of the inner ring PMTs). For the TOd-PMTs no voids appear as these have PDHs with a smaller region with no entries at small distances.

The distributions of ΔX and ΔY for the entry point are shown in figure 7.16. Compared to the corresponding plots of the barycenter method (see figure 6.14) these distributions have smaller widths by a factor of about 2.3. The widths indicated by the RMS of the histograms are about 113 mm and about 105 mm according to the σ of the Gaussian fit. Both are even smaller than the ones for the vertical muons (figure 7.8) and therefore, the best values obtained in the present work up to now. This can be partly explained by the lower contribution of muons with a true entry point at $R > 3000\,\mathrm{mm}$, what results in a smaller fraction of muons reconstructed with a smaller radius than the true one.

The ΔR-distribution (figure 7.21a) shows a small shift of the mean to negative values of slightly more than 20 mm, which is smaller than the shift for vertical muons of about 27 mm. This can again be explained by the lower contribution of muons at large true radii. The distribution of $\Delta\phi$ (figure 7.9b) is very similar to the one for the vertical muons and has a slightly smaller width.
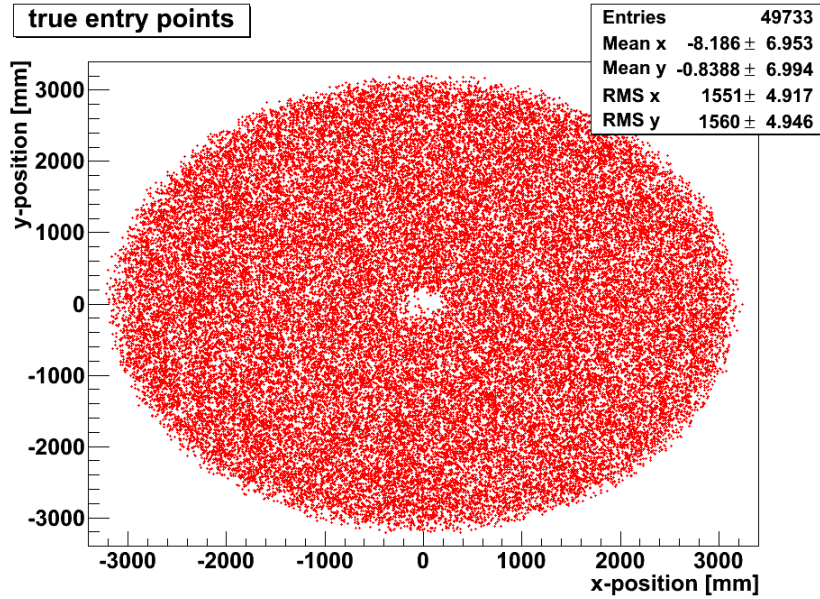
(a) True entry points
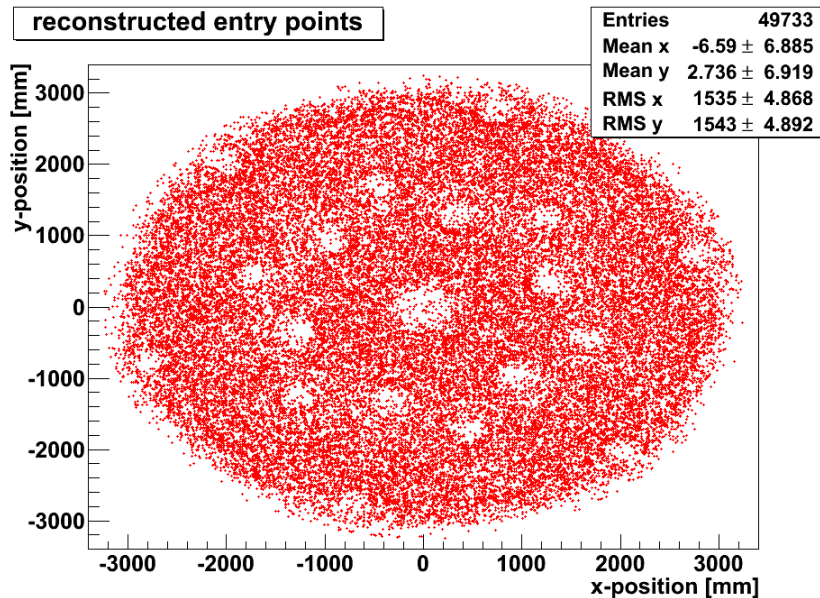
(b) Reconstructed entry points

Figure 7.15: *The true (a) and reconstructed (b) entry points in the x-y-plane at the top PMT mean z-position for 50 000 inclined 100 GeV muons (the missing muons were either contained in the chimney or were not reconstructed as no $P(x,y) > 0$ could be found). The decreasing density of true entry points at large radii is caused by the way of simulating the inclined muons. The voids at PMT positions for the reconstructed points are caused by PDHs with no entries at small distances and the void at the center by the chimney.*
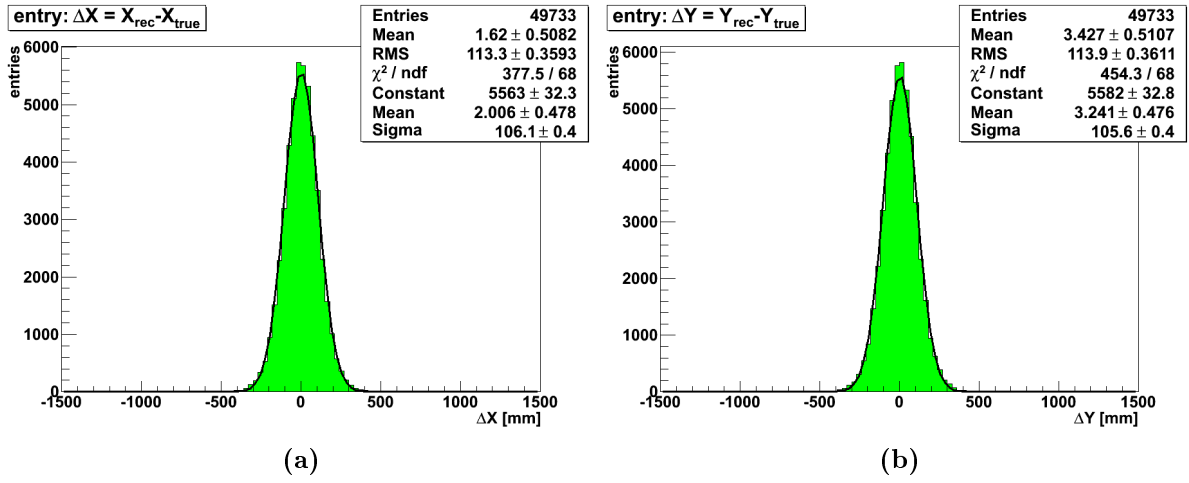
Figure 7.16: *Difference distributions for the x- and y-coordinate of the entry point for inclined 100 GeV muons. The distributions were fitted with a Gaussian to visualize the degree of symmetry.*
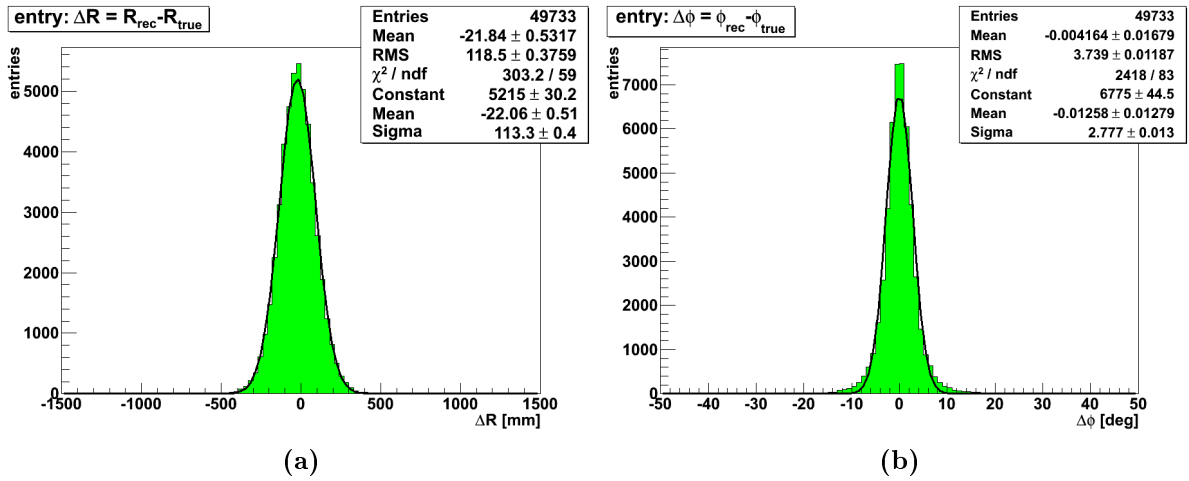
Figure 7.17: *Difference distributions for the R- and φ-coordinate of the entry point for inclined 100 GeV muons. The distributions were fitted with a Gaussian to visualize the degree of symmetry.*

7.3.2 Exit point reconstruction

In figure 7.18 the distributions of the true and the reconstructed exit points are depicted. As for the true entry points the lower density of true exit points at radii $R > 3000\,\mathrm{mm}$ is caused by the way of simulating the inclined muons. The reconstructed exit points show the following features:

- **Voids at the inner ring PMT positions:** As for the vertical muons one can see voids at the positions of the inner ring PMTs caused by the PDHs.

- **Few reconstructed points at R > 2800 mm:** At radii $R > 2800\,\mathrm{mm}$ only few points can be seen. Here an explanation by the lower density of true exit points at $R > 3000\,\mathrm{mm}$ is obviously not sufficient. As for the vertical muons, voids at the positions of the BOi-PMTs, which are arranged like the hours on a clock, can be seen. In addition, there are large empty areas around the BOu-PMTs, which are located between the BOi-PMTs. This cannot be explained by the effect causing the voids as the PDHs for the BOu-PMTs do not have that large regions with no entries at small distances.

  An explanation for this almost empty region may be given by an effect similar to the geometry in the Cherenkov effect, causing the first light produced by the muons in the scintillator to be on a cone. In the simulation the inner veto scintillator has a refractive index of about $n = 1.5$ [Gre10]. For $100\,\mathrm{GeV}$ muons, which travel in good approximation with the speed of light in vacuum, the Cherenkov angle can be estimated to be $\theta \approx 48\,\mathrm{degree}$ (see figure 7.19). For muons with an inclination with respect to the z-axis of more than $\alpha \approx 40\,\mathrm{degree}$ this can create a severe problem as the first light may be seen by two PMTs at the same time or with only a small time difference. Such a case is depicted in figure 7.19. In case that an inner ring and an outer ring PMT are hit with a small time difference, one can imagine that the reconstruction may give strange results.

  The maximum inclination to the z-axis of the simulated inclined muons, which are used here, is defined by the diameter and the distance between the two circle areas (see section 4.4 for more details). The resulting maximum angle then is $\alpha_{max} \approx 43\,\mathrm{degree}$. Therefore, inclined muons as used here only have inclinations to the z-axis in the range that matters for the problem above, when they have true entry and(!) exit points at large radii. Hence, problems due to the effect described above should appear in this region.

  Furthermore, the following effect may account for a part of the muons, which are reconstructed with a smaller radius than the true one: muons with a true entry point at a large radius produce light, which can travel along the side wall directly (without reflection) to the bottom inner veto. As estimated in section 5.1.3 this light needs about $t_\gamma(H_{IV}) \approx 23\,\mathrm{ns}$ to reach the bottom. A muon, which crosses the whole detector diagonally, needs $t_\mu(D_{IV}) \approx 32\,\mathrm{ns}$ to reach the bottom inner veto. This causes first or early hits appearing on the side of the inner veto, where the light from the top is detected. On the opposite side the muon causes hits at
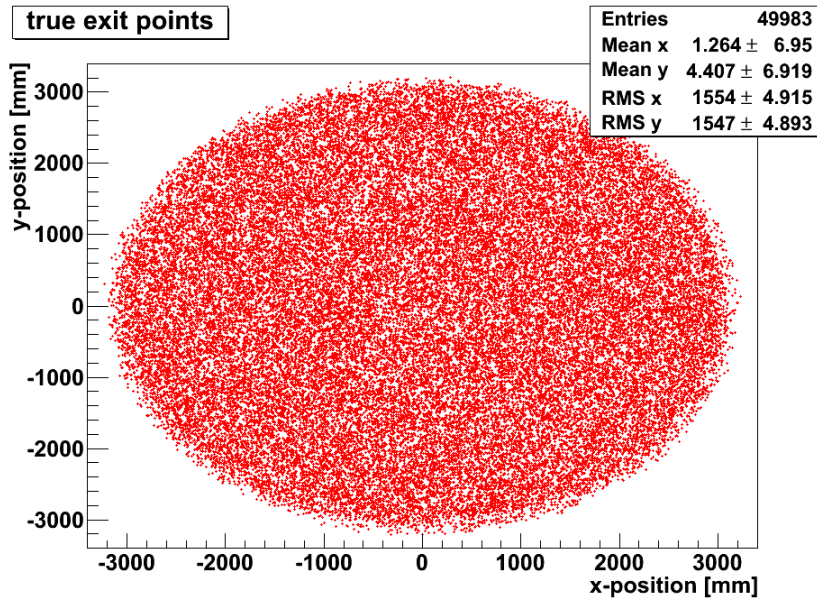
(a) True exit points
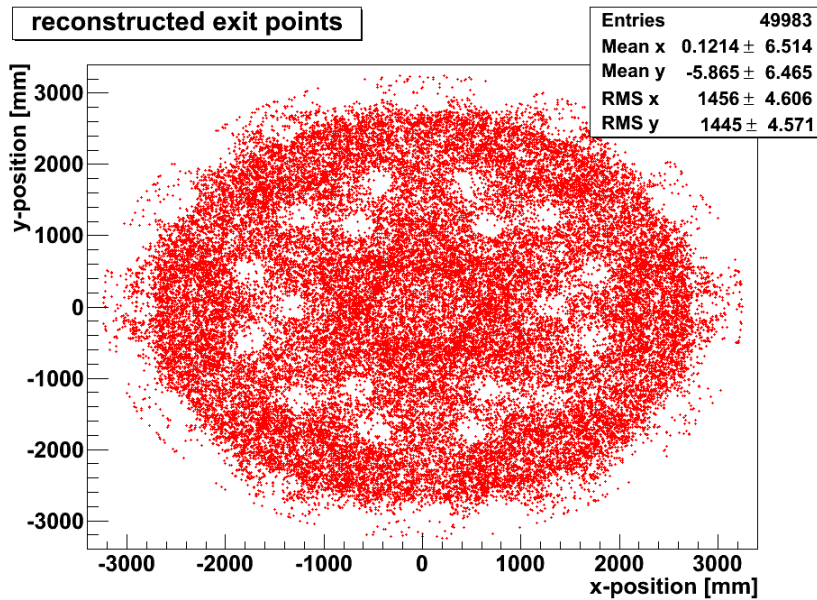
(b) Reconstructed exit points

Figure 7.18: *The true (a) and reconstructed (b) exit points in the x-y-plane at the bottom PMT mean z-position for $50\,000$ inclined $100\,GeV$ muons (the missing muons were not reconstructed as no $P(x,y) > 0$ could be found). Besides the voids at the inner ring PMT positions an almost empty region for large radii $R > 2800\,mm$ can be seen in the plot for the reconstructed exit points. This almost empty region cannot be completely explained by the effect causing the voids at the PMT positions. Here highly inclined muons cause problems (see text).*
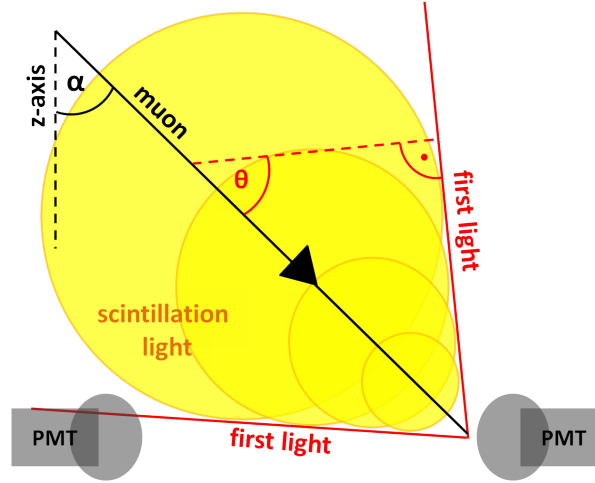
Figure 7.19: *A sketch of the Cherenkov effect and the resulting cone on which the first light (scintillation and Cherenkov light) from the muon can be seen. α denotes the inclination of the muon with respect to the z-axis and θ the Cherenkov angle, which is about 48 degrees in the inner veto liquid scintillator. An event as depicted here can cause hits in the inner and outer bottom PMT rings at the same time, while the muon passes close to the outer ring.*

almost the same time. Obviously these events at the bottom inner veto are not reconstructed properly, if at all a point with $P(x, y) > 0$ can be found. A possible extension of the algorithm to address this problem will be given later (see section 7.4).

Figure 7.20 shows the distributions of ΔX and ΔY for inclined muons reconstructed with the maximum likelihood method. As expected from the empty region at large radii in the reconstructed entry point plot both distributions are broadened compared to the ones for vertical muons. The widths indicated by the RMS of the histograms are about 225 mm and therefore, almost 80 mm larger than for the vertical muons. This is basically due to the flat tails of the distributions, which are caused by the muons with exit points at large radii reconstructed systematically to lower radii. Nevertheless, the widths of the distributions are again more narrow than for the barycenter method.

In figure 7.21 the distributions of ΔR and $\Delta \phi$ are shown. As one can see, the distribution for the polar angle is clearly broader than the one for the vertical muons (see figure 7.17b), what could be expected as both the ΔX- and the ΔY-distribution are broadened. The plot for ΔR also shows a shape, which could be expected due to the empty region at large radii in figure 7.18b.

In figure 7.22 $\Delta R = R_{rec} - R_{true}$ is plotted versus the true radius of the exit point R_{true}. Most of the points are concentrated in a main band. In a region between $R_{true} \approx 800$ mm to $R_{true} \approx 1500$ mm the center of this band is shifted to negative ΔR. This is due to the inner ring PMTs which are located in the region between $R \approx 1300$ mm and $R \approx$
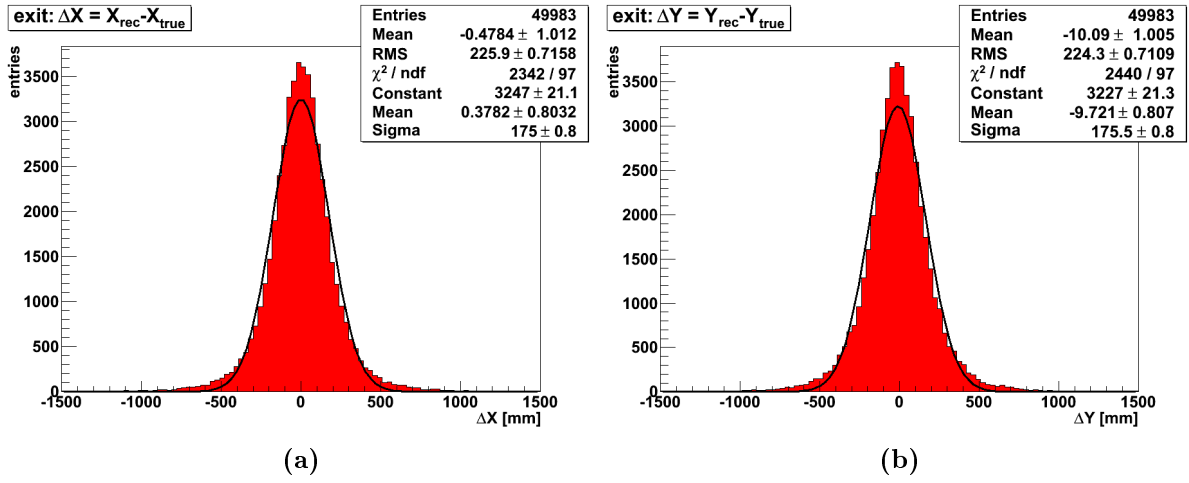
Figure 7.20: *Difference distributions for the x- and y-coordinate of the exit point for inclined 100 GeV muons. The distributions were fitted with a Gaussian to visualize the degree of symmetry.*
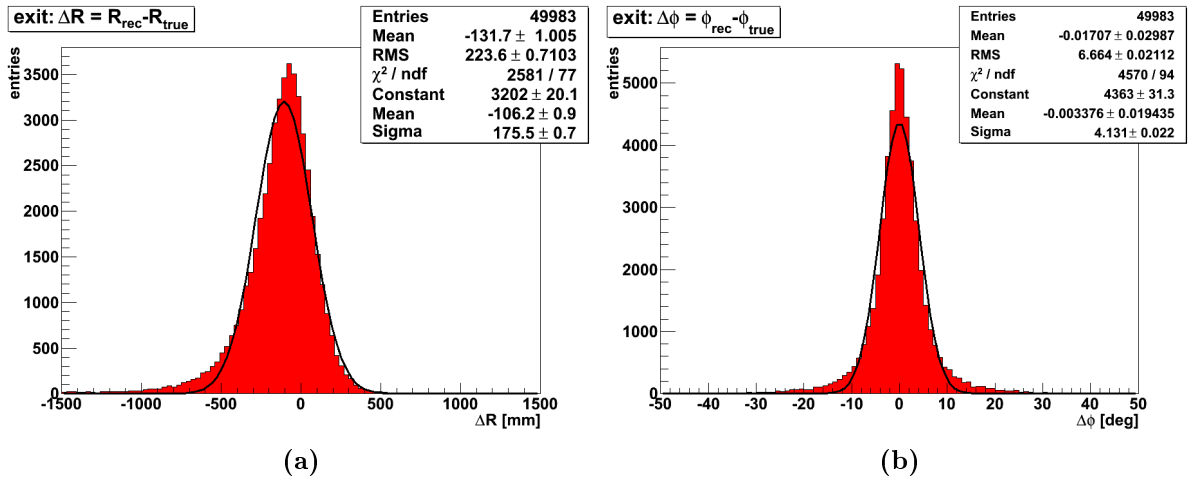
Figure 7.21: *Difference distributions for the R- and φ-coordinate of the exit point for inclined 100 GeV muons. The distributions were fitted with a Gaussian to visualize the degree of symmetry.*
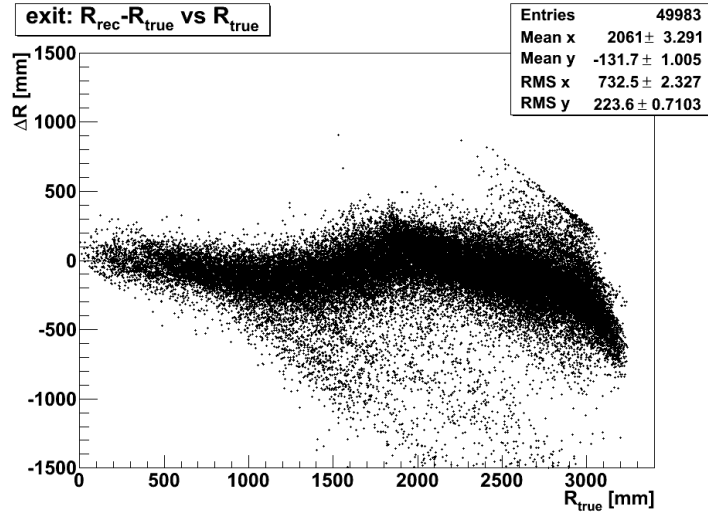
Figure 7.22: *Scatter plot for $\Delta R = R_{rec} - R_{true}$ versus the true exit point radius R_{true} for $50\,000$ reconstructed inclined $100\,GeV$ muons.*

$1800\,mm$. Due to the voids the reconstructed points seem to be shifted systematically to smaller radii in the region of the inner ring PMTs. Furthermore, the center of the main band decreases rather linearly from about $R_{true} \approx 1900\,mm$ to about $R_{true} \approx 2800\,mm$, where it starts to decrease stronger. In the range from $R_{true} \approx 2800\,mm$ to larger radii the outer ring PMTs are located. Here the voids cause a shift to smaller reconstructed radii. The decreasing behaviour of the band center for the region between the inner and the outer ring PMTs is not understood precisely up to now. It partly may be due to muons with a relatively large inclination to the z-axis causing PMT hits in the inner and the outer ring with the same time or with a small time difference (see list above).

Furthermore, one can see many points below the main band. In the range of the inner ring PMTs these may partly be due to the voids around the PMTs. In addition, these points may be explained by the effects described in the list above regarding the almost empty region for $R > 2800\,mm$ in the reconstructed exit point plot. The points in the upper right region of the plot are exit points reconstructed to $R_{rec} \approx 3250\,mm$.

7.3.3 Reconstructed momentum direction

Figure 7.23 shows the distribution of the angle between the true and the reconstructed muon momentum direction. As for the vertical muons (figure 7.14) the maximum lies at 1.5 degree, but the mean and the RMS of the histogram are increased. This could be expected as the widths of the ΔX- and ΔY- distributions are larger for the exit point. Nevertheless, this distribution shows that even with the problems described above the maximum likelihood method works better than the barycenter method (see section 6.6 and figure 6.6.3).
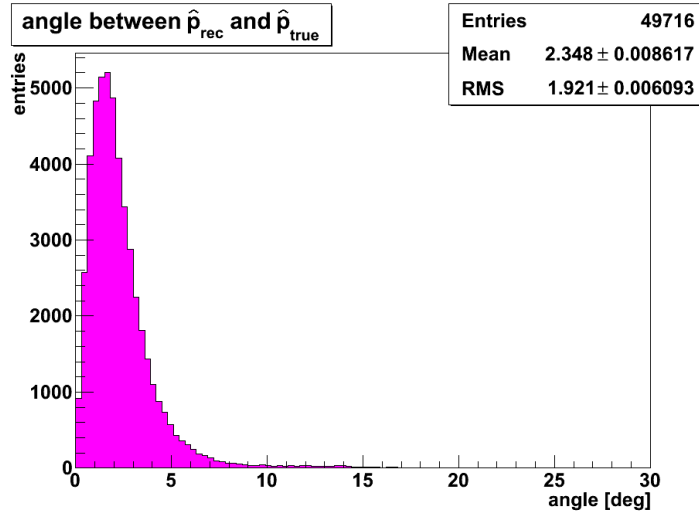
Figure 7.23: *The distribution of the angle between the true primary momentum direction $\hat{p}_{true}$ and the reconstructed momentum direction $\hat{p}_{rec}$ for inclined muons (angle in degree (deg)).*

7.4 Restricted exit point reconstruction

As described in the previous section light from the top can cause problems, when the muon passes the whole detector diagonally. In such cases hits appear on two opposite sides of the bottom inner veto, where the hits due to the light produced at the top inner veto can have charges exceeding 50 pe. Therefore, it is not possible to handle all these events by a charge threshold.

7.4.1 Changes in the reconstruction

To reduce the problems due to these events the following changes to the algorithm have been introduced: the main idea is to use only the PMT hits on the side of the bottom inner veto, where the muon had passed. All hits in the vicinity of the muon see much light causing large charges, while the light from the top basically causes hits with medium charges in the bottom outer ring. Therefore, the sum of the charges seen by PMTs in certain regions can be used to gather the information where the muon has passed and use the PMTs of the region with the largest summed charge. This is realized by a classification of the bottom PMTs into different sectors as depicted in figure 7.24. The algorithm distinguishes between three different kinds of events at the bottom inner veto:

- **First hit PMT is BIo, BOu or BOiNF:** In this case the sums of the charges seen by the PMTs of the sectors depicted in **green** (see figure 7.24) are calculated after all contributing PMTs have been selected by the standard selection as described in section 7.1.5. Then, the sector with the largest summed charge is determined. This maximum charge sector, the both neighbouring sectors and the two BOiF-PMTs between these sectors are then used for the reconstruction. An example: the green
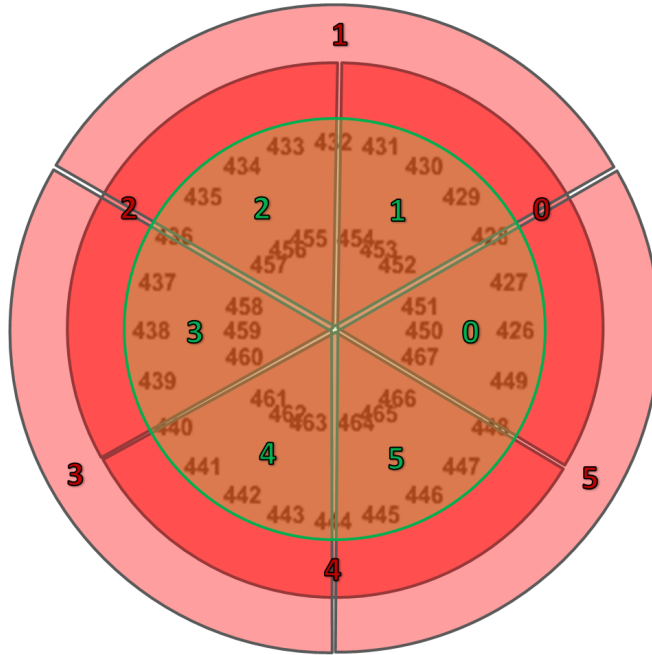
Figure 7.24: *Classification of the bottom inner veto PMTs into sectors. Depending on the first hit PMT the sectors depicted in green or the sectors depicted in red are used to reconstruct the exit point. The green sectors consist of the PMTs between the buffer feet: green sector 1, for example, consists of the PMTs 429, 430, 431, 452, 453 and 454. The sectors depicted in red contain the PMTs of two neighbouring green sectors and the BOiF between these sectors: for example the red sector 0 consists of the green sectors 0 and 1 and the BOiF-PMT 428.*

sector with the largest charge sum is sector 3. Then, the PMTs from sector 2, sector 3, sector 4, and the BOiF-PMTs 436 and 440 are used for the reconstruction.

- **First hit PMT is BOiF:** In case that the first PMT is a BOi-PMT facing a buffer foot the sectors depicted in **red** in figure 7.24 are used. After the standard selection the summed charges of the red sectors are determined. The red sector with the maximum summed charge is then used to reconstruct the exit point.

- **First hit PMT is BIi:** The events at the bottom inner veto, where the first PMT is a inner ring PMT watching inwards, are handled in the standard way, i.e. all PMTs, which satisfy the standard selection criteria (time window and charge threshold), are used for the reconstruction. For muons passing the bottom inner veto inside the inner PMT ring the hit information of all BIi-PMTs is important.

In the current version of the maximum likelihood method it is only possible to reconstruct all muons using the restricted exit reconstruction described above or to reconstruct them in the standard way with the selection using only the time window and the charge threshold.
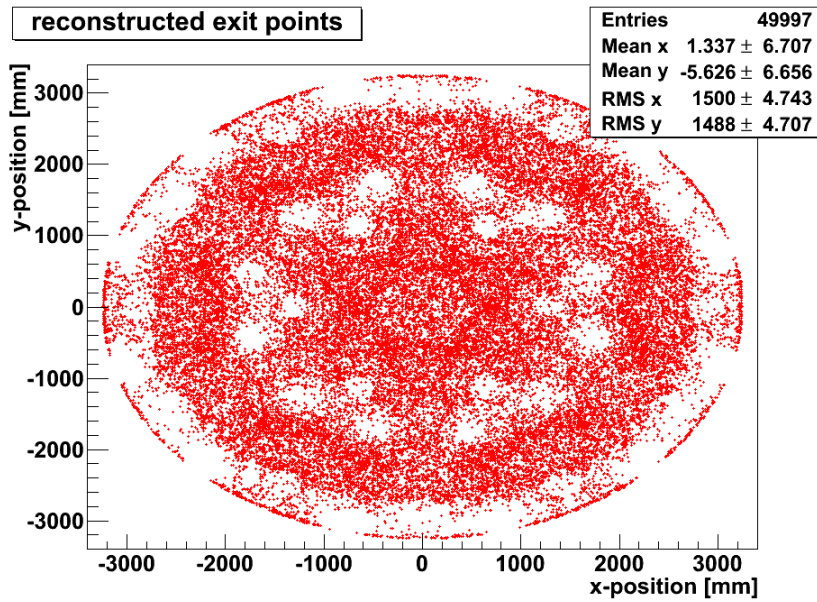
Figure 7.25: *The reconstructed exit points in the x-y-plane at the bottom PMT mean z-position for $50\,000$ inclined $100\,GeV$ muons using the maximum likelihood method with the restricted exit point reconstruction as described in section 7.4.1 (the missing muons were not reconstructed as no $P(x,y) > 0$ could be found). The main difference to the plot for the reconstruction without using only hits from certain sectors (see figure 7.18b) is that many points appear at $R \approx 3250\,mm$.*

7.4.2 Results

Again, the $50\,000$ inclined muons were reconstructed with the changes described above. Figure 7.25 shows the reconstructed exit points. Again, one can see the voids at the inner ring PMT positions. The main difference to the corresponding plot without the restricted exit reconstruction (see figure 7.18b) are the points appearing close to the edge of the inner veto. Furthermore, one can see slightly more points in the vicinity of the BOiNF-PMTs. Hence, the restricted bottom reconstruction seems to have solved the problem with the wrongly reconstructed muons at large true radii at least partly. In addition, one can see that for more muons the exit point could have been reconstructed.

In figure 7.26 the corresponding distributions of ΔX and ΔY are shown. Compared to the reconstruction without the restriction (see figure 7.16) these distributions are marginally broadened by few millimetres according to the RMS of the histograms. The values for the σ of the Gaussian fit are increased stronger by about $10\,mm$ as the central part of the distribution is broadened and therefore, the Gaussian fits less badly than for the reconstruction without restriction.

Figure 7.27 shows the difference distributions for the radius and the polar angle. The distribution for $\Delta \phi$ appears to be slightly more narrow by about 0.1 degrees compared to the corresponding plot without the restricted exit reconstruction (see figure 7.21b).
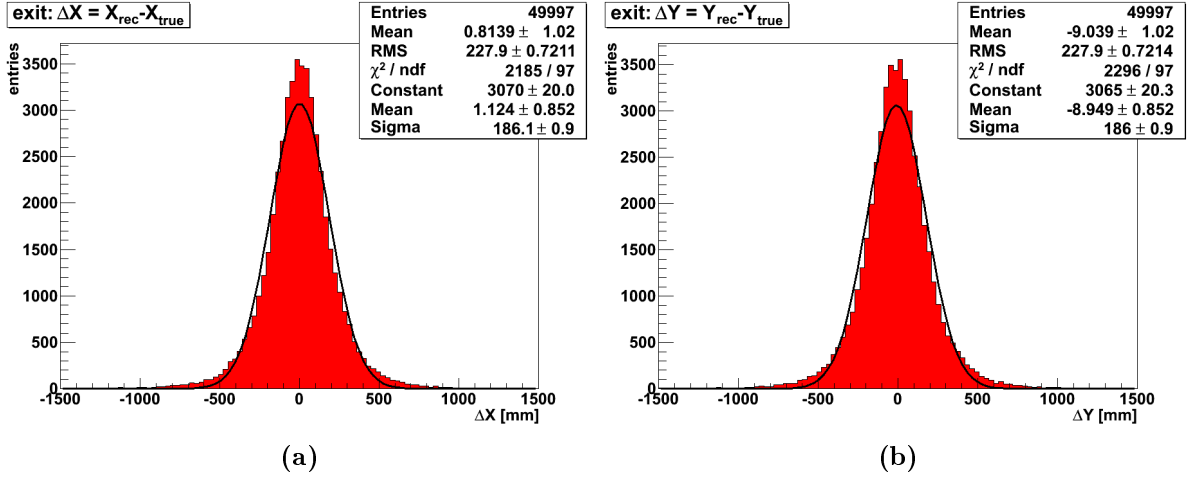
Figure 7.26: *Difference distributions for the x- and y-coordinate of the exit point using the maximum likelihood method with the restricted exit point reconstruction as described in section 7.4.1. The distributions were fitted with a Gaussian to visualize the degree of symmetry.*

This can be explained by the reconstructed exit points at $R \approx 3250$ mm. The difference distribution for the radius coordinate (figure 7.27a) shows a width, which is larger by more than 30 mm compared to the plot for the reconstruction without the restriction (see figure 7.21a). Furthermore, the shift of the mean to negative values is smaller by about 45 mm according to the mean of the histograms. Both features are caused by the larger contribution of muons reconstructed with $\Delta R > 0$. These muons are at least partly those, which appear at $R \approx 3250$ mm in the plot for the reconstructed exit points (figure 7.25).

In figure 7.28 ΔR is plotted versus the true exit point radius R_{true}. As for the corresponding plot for the reconstruction without the restrictions for the exit point reconstruction (see figure 7.22) one can see a main band, but here this band jumps to $\Delta R > 0$ at $R_{true} \approx 1650$ mm. This can be explained by using the PMTs of certain sectors only. The muons passing the bottom inner veto in the region of the inner ring PMTs are reconstructed with larger radii as the outer ring PMTs can see the light produced in this region directly. Furthermore, one can see more points in the upper right part of the plot. These form a narrow band with decreasing ΔR for increasing R_{true}. This band is caused by the points at $R \approx 3250$ mm in the reconstructed exit point plot (see figure 7.25). The points at negative ΔR below the main band could not have been reduced significantly by the restricted exit point reconstruction. These points may be due to inclined muons causing hits with the same start time at the inner and the outer PMT ring, while the muon passes at large radii close to the outer ring PMTs (see figure 7.19). Such events cannot be reconstructed better by using only PMTs from certain sectors.

In figure 7.29 the distribution of the angle between the true and the reconstructed momentum angle is depicted. Although the distributions for ΔX and ΔY showed in-
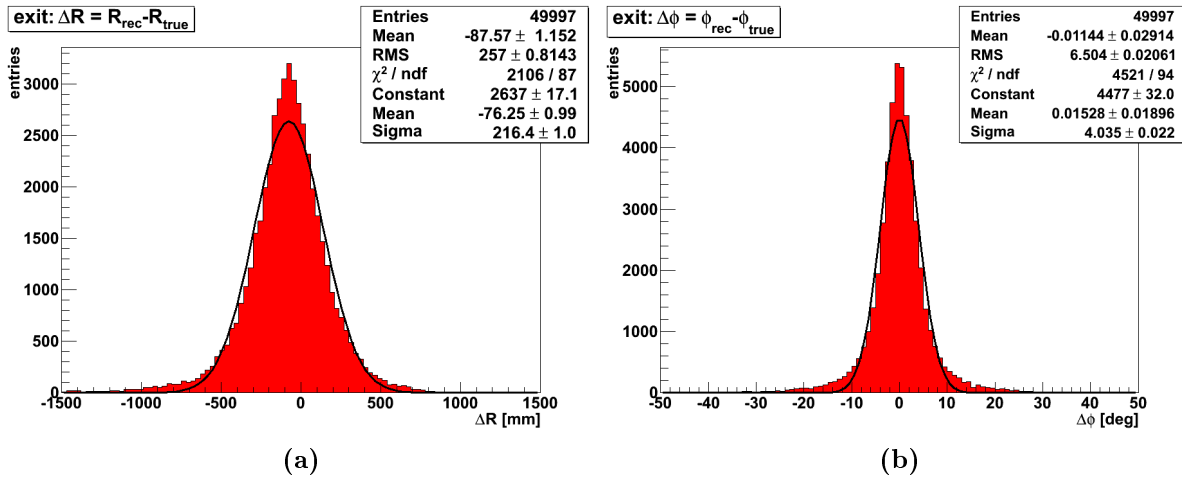
Figure 7.27: *Difference distributions for the R- and ϕ-coordinate of the exit point using the maximum likelihood method with the restricted exit point reconstruction as described in section 7.4.1. The distributions were fitted with a Gaussian to visualize the degree of symmetry.*
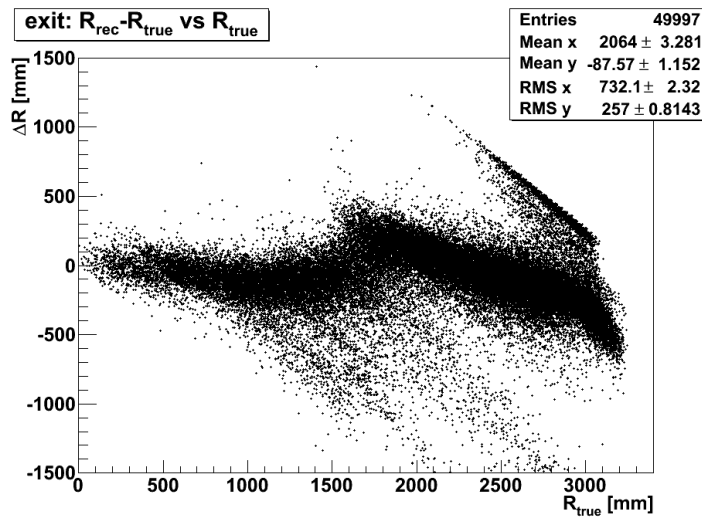
Figure 7.28: *Scatter plot for $\Delta R = R_{rec} - R_{true}$ versus the true exit point radius R_{true} for 50 000 inclined 100 GeV muons using the maximum likelihood method with the restricted exit point reconstruction as described in section 7.4.1.*
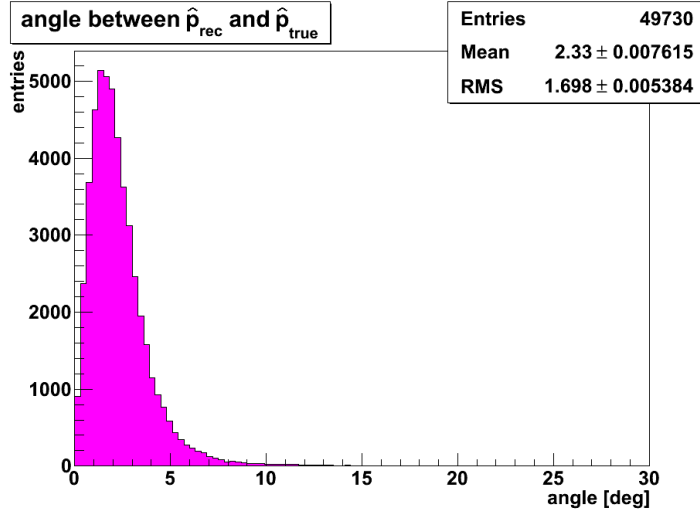
Figure 7.29: *The distribution of the angle between the true primary momentum direction $\hat{p}_{true}$ and the reconstructed momentum direction $\hat{p}_{rec}$ for inclined muons reconstructed using the maximum likelihood method with the restricted exit point reconstruction as described in section 7.4.1 (with $t_{window} = 30\,ns$ and $q_{thresh} = 1\,pe$).*

creased widths compared to the not restricted exit point reconstruction the distribution depicted in figure 7.29 has a smaller mean and a smaller RMS value. This is due to less entries at angles exceeding 10 degree.

All in all the restricted exit point reconstruction did not significantly change the accuracy in the determination of the exit points and the momentum direction, but the shift of the mean and the asymmetry of the ΔR-distribution could be reduced. The main improvement is that for more muons an exit point can be reconstructed as the events with hits due to light from the top are handled in a more suitable way.

7.5 Performance for small muon energies

Muons with small energies may be stopped within the top or bottom inner veto, what results in less produced light. Furthermore, these muons are deflected stronger than muons with large energies. Both effects may cause problems regarding the reconstruction of the entry and exit points. Therefore, inclined muons have also been simulated in a momentum range from $p_0 = 100\,\mathrm{MeV/c}$ to $p_0 = 5\,\mathrm{GeV/c}$ to test the maximum likelihood method in this range. The momenta were chosen randomly with a uniform distribution. In sum, $650\,000$ muons were simulated: $500\,000$ are used to produce the PDHs and $150\,000$ of these muons are used to test the reconstruction. All plots in the following rely on reconstructions using a time window $t_{window} = 30\,\mathrm{ns}$ and a charge threshold of $q_{thresh} = 1\,\mathrm{pe}$.
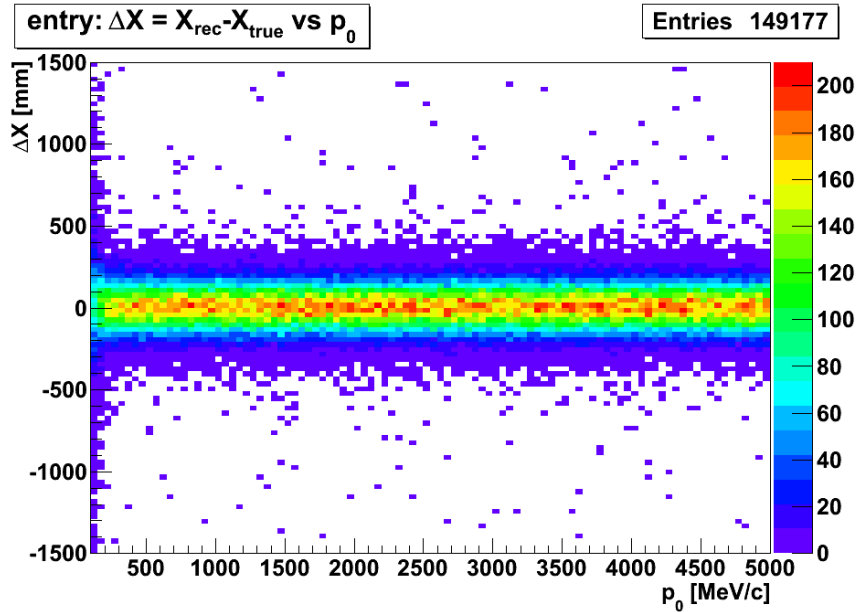
Figure 7.30: *2D-histogram for the entry point reconstruction: ΔX is plotted versus the initial muon momentum p_0 for inclined muons in a momentum range of $100\,MeV/c \leq p_0 \leq 5\,GeV/c$ (with $t_{window} = 30\,ns$ and $q_{thresh} = 1\,pe$). The colours indicate the number of entries in the bins.*

7.5.1 Entry point reconstruction

Figure 7.30 shows a 2D-histogram for ΔX regarding the entry point versus the initial muon momentum p_0, where the colours indicate the number of entries in the corresponding bins. The reconstruction shows a very constant performance down to $p_0 \approx 200\,\text{MeV/c}$. For smaller initial muon momenta the distribution gets broader.

As it can be derived from the Bethe-Bloch formula muons with momenta larger than $100\,\text{MeV/c}$ are minimum-ionizing with an energy loss of about $(2 \cdot \rho)\,\text{MeV/cm}$, where ρ is the density of the material the muon is propagating through [Leo94, PDG10]. For momenta below $100\,\text{MeV/c}$ the energy loss increases with decreasing muon energy. The scintillators for the DOUBLE CHOOZ detector have a density of about $\rho \sim 0.8\,\text{g/cm}^2$, which leads to an energy loss of the muons of approximately $1.6\,\text{MeV/cm}$. As the muons were injected at $z = 3500\,\text{mm}$, what is about $50\,\text{mm}$ above the top inner veto, all muons cause a signal in the top inner veto as long as they are not fully hidden within the chimney. Nevertheless, the muons with the smallest initial momenta may be stopped within the top inner veto, causing a reduced precision of the reconstructed entry point.

7.5.2 Exit point reconstruction

In figure 7.31 a 2D-histogram for the exit points ΔX versus the initial muon momentum p_0 is depicted. The exit points have been reconstructed with the restricted exit point reconstruction as described in section 7.4. As one can see muons down to momenta of
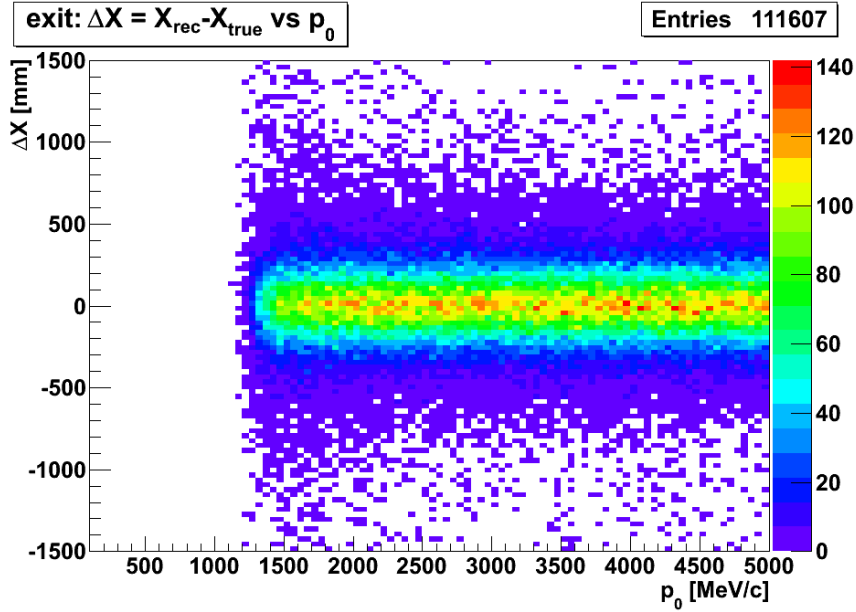
Figure 7.31: *2D-histogram for the exit points with restricted exit point reconstruction: ΔX is plotted versus the initial muon momentum p_0 for inclined muons in a momentum range of $100\,MeV/c \leq p_0 \leq 5\,GeV/c$ (with $t_{window} = 30\,ns$ and $q_{thresh} = 1\,pe$). The colours indicate the number of entries in the bins.*

about $1.6\,\text{GeV/c}$ can be reconstructed with relatively constant precision indicated by the width of the central region regarding ΔX (colour red to turquoise). For smaller p_0 the width of the central region decreases. Also the number of reconstructed exit points gets smaller. Finally, for no muon with a momentum smaller than about $1100\,\text{MeV/c}$ an exit point could be reconstructed.

This behaviour can be explained by the energy loss described above. A vertical muon starting at $z = 3500\,\text{mm}$ (the inclined muons are started here) has to cover a distance of about $6.4\,\text{m}$ to reach the bottom inner veto. The minimum energy loss in the DOUBLE CHOOZ scintillators corresponding to this distance is about $1\,\text{GeV}$. A moun with a large inclination to the z-axis has to cover a distance of up to $9\,\text{m}$ to reach the bottom inner veto, what corresponds to an energy loss of up to about $1.5\,\text{GeV}$. Therefore, the number of muons with a reconstructed exit point is expected to decrease to zero for momenta of about $1.5\,\text{GeV/c}$ to momenta of about $1\,\text{GeV/c}$, what can be seen nicely in figure 7.31.

The results demonstrate that the maximum likelihood method performs very robust down to small energies at the top and bottom inner veto. The performance at the smallest muon energies is limited by the physical processes only.

7.6 Summary

In this chapter the maximum likelihood method was described and motivated. It uses so-called probability density histograms (PDHs), which contain the correlated information about the pulse start times of the hits and the distance to the true muon track gathered from detailed muon simulations. As the barycenter approach the maximum likelihood method relies on the reconstruction of an inner veto entry and an inner veto exit point. These two points are reconstructed by scans of the x-y-planes at the top and bottom inner veto PMT positions, which search for the coordinates with the best agreement between the PDHs and the timing data of the contributing PMTs. The reconstructed track is approximated as the straight line defined by the two determined points.

The method was tested with vertical 100 GeV muons first using different sets of the reconstruction parameters. The results obtained for the set showing the best performance were discussed in more detail: the maximum likelihood method reaches an accuracy, which is by a factor of about two better than the accuracy of the barycenter method regarding the determination of the inner veto points. The same parameter set was used to test the method with inclined 100 GeV muons. The obtained results show that the accuracy in the determination of the entry point is even better than for the vertical muons, while the exit points are reconstructed less precise. This is thought to be mainly caused by different effects regarding highly inclined muons.

To reduce certain effects due to the highest inclined muons the algorithm for the exit point reconstruction was changed to use only PMTs from selected sectors at the bottom inner veto. The obtained results regarding the accuracy do not differ much from the results without the changes, but the efficiency of the reconstruction could be increased.

Furthermore, the maximum likelihood method was tested for inclined muons with smaller energies and both the entry and the exit point reconstruction perform rather independent from the energy except for the smallest energies at the top and the bottom inner veto.

All in all the maximum likelihood method is a very promising approach for a muon track reconstruction with the inner veto. The accuracies in the determination of the entry and exit points and the resulting precision in the reconstruction of the momentum direction are the best, which could be reached in all studies on muon track reconstructions within the Double Chooz collaboration up to now.

8 Conclusion and outlook

DOUBLE CHOOZ is a reactor neutrino experiment in the French Ardennes, which is designed to search for the last unknown neutrino mixing angle ϑ_{13}. Up to now only an upper limit for this parameter of $\sin^2(2\vartheta_{13}) < 0.16$ could be determined. DOUBLE CHOOZ uses two identical cylindrical detectors: a near detector is placed in a distance of about 400 m to the reactors to monitor the flux of the electron antineutrinos and its spectral shape without an effect due to oscillations. A far detector is placed at a distance of 1.05 km to the reactors, which is close to the optimum position for a measurement of the neutrino flux and its shape with the maximum oscillation amplitude $\sin^2(2\vartheta_{13})$. The desired sensitivity in case that no oscillation effect can be observed is $\sin^2(2\vartheta_{13}) \leq 0.03$ after three years of data taking with both detectors.

The DOUBLE CHOOZ detectors have an overburden of only 115 m.w.e. for the near and 300 m.w.e. for the far site, what implies a huge background induced by cosmic muons. To detect the electron antineutrinos from the reactors DOUBLE CHOOZ uses the inverse beta decay, which causes events with a delayed coincidence of a prompt energy deposition by the positron followed by a neutron capture on gadolinium after about 30 µs. This reduces the critical backgrounds to those mimicking this delayed coincidence: besides the accidental background, these are the fast neutrons and the cosmogenic isotopes ^{8}He and ^{9}Li, which are produced by muons inside or in the vicinity of the detectors. Fast neutrons can cause neutrino-like events by scattering off a proton before being captured on gadolinium. ^{8}He and ^{9}Li have large branching ratios to decay by a β-n-cascade causing a delayed coincidence signal. These backgrounds have a contribution to the neutrino-like signal in both detectors in the order of few percent and therefore, limit the reachable sensitivity in the determination of $\sin^2(2\vartheta_{13})$.

A muon track reconstruction provides possibilities to gather information on these backgrounds on the one hand and to reject these backgrounds on the other hand. In the present work two approaches for a muon tracking using the inner veto, which is the outermost cylindrical volume of both DOUBLE CHOOZ detectors, have been studied. In both methods the reconstructed muon track is approximated to be the straight line defined by two reconstructed points: an inner veto entry point using the hit PMTs at the top inner veto and an inner veto exit point with the hits at the bottom inner veto.

To test both reconstruction algorithms vertical and inclined muons with an energy of 100 GeV have been simulated using the detailed GEANT4-based DOUBLE CHOOZ detector simulation DCGLG4sim. The inclined muons were simulated in such a way that no muon enters and leaves the detector through the inner veto side wall, as such muons are more complicated to reconstruct and the current versions of the reconstruction algorithms cannot handle the corresponding events properly. All simulation data was processed through the DOUBLE CHOOZ readout system simulation (RoSS) and the pulse

characterisation tool RecoPulse. Hence, in the used data all uncertainties due to the electronic readout chain and the pulse reconstruction are fully taken into account.

The first approach was the barycenter method, which relies on the determination of barycenters of the PMT hits, where the charge and the timing information of the hit PMTs is taken into account. The hits used for the reconstruction are selected by a charge threshold and a time window, which is opened after the first hit at the top and the bottom inner veto, respectively.

In the present work the method was tested for vertical muons using different sets of the reconstruction parameters. The parameter set with the best results for vertical muons (see table 8.1) was also used to test the reconstruction with inclined muons. The accuracy in the determination of the inner veto points was found to be rather independent regarding the degree of inclination of the muons and is about 27 cm for the entry points and 25 cm for the exit points. Due to the large distance between both reconstructed points of at least 6.3 m the momentum direction of the muons can be reconstructed with an accuracy of about 3.5 degrees for inclined muons and slightly better with an accuracy of 3.2 degrees for vertical muons.

parameter	m	n	t_{window}	q_{thresh}
barycenter method	2	1	10 ns	1 pe
maximum likelihood method	–	–	30 ns	1 pe

Table 8.1: *Reconstruction parameter sets showing the best results for the barycenter and maximum likelihood method. m and n are exponents used in the weightings of the barycenter formula. t_{window} and q_{thresh} are a time window and a charge threshold used to select the PMT hits, which contribute to the reconstruction of the inner veto entry and exit points.*

The barycenter reconstruction basically suffers from intrinsic problems of a barycenter calculation and from shadowing effects, which cause hits due to reflected light. The contribution of such hits could be reduced by applying a short time window of 10 ns in which the PMT hits have to appear. The method also shows clustering of the reconstructed points near PMT positions and on the connecting lines between the PMTs. This effect may be reduced by different time windows for the weightings and for the PMT hit selection. A longer time window in the weightings would emphasize the earliest hits less strong with respect to the later ones and therefore, the calculated barycenters would be shifted less towards the first hit PMTs. Furthermore, different charge thresholds and time windows for the PMT selection for the entry and the exit point reconstruction may result in a further improvement of the accuracy of the barycenter method. This should be addressed in further studies.

	vertical muons			inclined muons		
	entry	**exit**	**p̂**	**entry**	**exit**	**p̂**
barycenter method	$\sim 27\,\mathrm{cm}$	$\sim 25\,\mathrm{cm}$	$\sim 3.2\,\mathrm{deg}$	$\sim 27\,\mathrm{cm}$	$\sim 24\,\mathrm{cm}$	$\sim 3.5\,\mathrm{deg}$
maximum likelihood method	$\sim 13\,\mathrm{cm}$	$\sim 15\,\mathrm{cm}$	$\sim 1.9\,\mathrm{deg}$	$\sim 11\,\mathrm{cm}$	$\sim 23\,\mathrm{cm}$	$\sim 2.3\,\mathrm{deg}$

Table 8.2: *Accuracies of the reconstruction methods regarding the entry and exit points and the muon momentum direction p̂. The accuracies of the maximum likelihood method regarding inclined muons are quoted for an applied restricted exit point reconstruction.*

Problems in the early phase of the studies on the barycenter method inspired the second approach presented in the present work: the maximum likelihood method uses histograms, which contain the timing information of the PMT hits correlated with the distance to the muon track gathered from detailed muon simulations - the probability density histograms (PDHs). The inner veto entry and exit points are reconstructed to be the points in the x-y-planes at the top and bottom PMT z-positions with the best agreement between the data and the PDHs. As for the barycenter method the hits used for the reconstruction are selected using a charge threshold and a time window.

The maximum likelihood reconstruction was tested for vertical muons with different sets of the reconstruction parameters, too. Regarding the best performance parameter set for vertical muons (see table 8.1) the maximum likelihood method shows very promising results: the accuracy of the reconstruction is about 13 cm for the entry points and 15 cm for the exit points, which is roughly by a factor of two better than for the barycenter method. The resulting resolution of the determined momentum direction of the muons is about 1.9 degrees and hence, more than 1.3 degrees better than the corresponding accuracy for the barycenter approach. As for the barycenter method the best performance parameter set for the vertical muons was used to test the reconstruction with inclined muons. For these the entry points are reconstructed even better with an accuracy of about 11 cm, but the accuracy in the determination of the inner veto exit points decreases to about 23 cm. The reduced precision of the exit point reconstruction is thought to be mainly caused by muons passing the detector with high inclination with true inner veto entry and exit points at large radii. Nevertheless, the precision of the momentum direction reconstruction for the inclined muons is about 2.3 degrees.

Highly inclined muons can cause events at the bottom inner veto, where hits due to light produced at the top inner veto appear at roughly the same time as hits caused by the muon at the opposite side of the bottom inner veto. The maximum likelihood method is not able to handle these events correctly. Therefore, the algorithm was changed to use only hits in certain PMT sectors to reconstruct the inner veto exit points (restricted exit

point reconstruction). The obtained results are very similar to the results without the changes, but the efficiency of the reconstruction could be improved as the critical events are reconstructed in a more suitable manner. In the current version of the algorithm this restricted exit point reconstruction can only be used for either all events or no event. An improvement of the maximum likelihood method may be achieved if the restricted exit point reconstruction is used only for those events, where it is needed. To realize this an efficient method of tagging such events is mandatory. An additional improvement of the maximum likelihood reconstruction may be obtained, when different charge thresholds and time windows for the selection of the PMT hits for the entry and exit point reconstruction are used.

Furthermore, the maximum likelihood method was tested for simulated inclined muons with initial momenta between $100\,\mathrm{MeV/c}$ and $5\,\mathrm{GeV/c}$. The entry point reconstruction shows a robust behaviour down to initial muon momenta of about $200\,\mathrm{MeV/c}$. The performance of the exit point reconstruction is very constant for initial momenta down to about $1.6\,\mathrm{GeV/c}$. The energy loss of muons reaching the bottom inner veto is $1\,\mathrm{GeV}$ to $1.5\,\mathrm{GeV}$, what results in the larger threshold for the exit point reconstruction.

Both reconstruction methods still have to be tested with simulated muons with the actual angular and energy distribution at the far and near detector site. The tests regarding the muons at the far site are the most urgent as this detector is in the final steps of the construction. To prepare the reconstruction algorithms for these muons an efficient way of tagging muons entering or leaving the inner veto through the side wall has to be developed. Furthermore, muons which are stopped in the detector have to be tagged efficiently as these can nonetheless cause reconstructed exit points due to light produced at the top or at the side wall of the inner veto.

The experiences gathered during the development of both reconstruction algorithms can be used for future studies on possible or already existing approaches for reconstruction methods using other parts of the Double Chooz detectors as the outer veto or the target and the gamma catcher. Furthermore, an improved track reconstruction may be obtained, when different methods are combined by fitting a track to all determined points in the inner detector and the outer veto, for example.

Finally, both methods wait for the completion of the far detector to be tested with the real data from the detector. Performance tests regarding the goodness of both reconstruction algorithms with the actual detector data will be possible, when the outer veto is ready to be used. The outer veto is designed to detect and track the muons with high efficiency and consists of plastic scintillator modules arranged in two layers above the inner detector. Therefore, the outer veto provides the possibility to determine the efficiency of the inner veto with real data, but its construction cannot start before the inner detector is completed.

Glossary

ADC .... analogue-to-digital converter

BC .... barycenter method

BIi .... IV bottom inner ring PMTs, watching inwards

BIo .... IV bottom inner ring PMTs, watching outwards

BOiF .... BOi-PMTs facing a buffer foot

BOiNF .... BOi-PMTs not facing a buffer foot

BOi .... IV bottom outer ring PMTs, watching inwards

BOu .... IV bottom outer ring PMTs, watching upwards

C.L. .... cinfidence level

CCin2p3 .... IN2P3 computing centre in Lyon (France)

CP .... charge and parity conjugation

DCAna .... analysis framework template within DOGS

DCGLG4sim ... DOUBLE CHOOZ generic land GEANT4 simulation

DOGS .... DOUBLE CHOOZ offline group software

DUQ .... digital units of charge

IV .... inner veto

m.w.e. .... metres of water equivalent: $1\ m.w.e. \mathrel{\hat=} 100\ g/cm^2$

ML .... maximum likelihood method

MSW .... Mikheyev-Smirnov-Wolfenstein

OV .... outer veto

PDH .... probability density histogram

pe .... photoelectron

PMNS .... Pontecorvo-Maki-Nakagawa-Sakata

PMT .... photomultiplier tube

RecoPulse ..... pulse reconstruction tool of DOGS

RMS .... root mean square

RoSS .... readout system simulation

TIi .... IV top inner ring PMTs, watching inwards

TIo .... IV top inner ring PMTs, watching outwards

TOd .... IV top outer ring PMTs, watching downwards

TOi .... IV top outer ring PMTs, watching inwards

TTS .... transit time spread

List of Figures

List of Tables

Bibliography

[Abe10]   S. ABE ET AL., KAMLAND collaboration: *"Production of radioactive isotopes through cosmic muon spallation in* KAMLAND*"*, arXiv:0907.0066v2 [hep-ex]

[Ago03]   S. AGOSTINELLI ET AL.: *"Geant4 - A simulation toolkit"*, Nucl. Instr. Meth. A **506**, 250-303 (2003)

[Akh00]   E.K. AKHMEDOV: *"Neutrino physics"*, arXiv:hep-ph/0001264v2

[Akh06]   E.K. AKHMEDOV: *"Neutrino oscillations: theory and phenomenology"*, arXiv:hep-ph/0610064v2

[Aki08]   T. AKIRI ET AL.: *"FADC status"*, DOUBLE CHOOZ internal talk: DC-doc-26-v1

[Alt05]   G. ALTARELLI: *"The Standard Model of Particle Physics"*, arXiv:hep-ph/0510281v1

[Ard04]   F. ARDELLIER ET AL., DOUBLE CHOOZ collaboration: *"Letter of Intent for* DOUBLE CHOOZ*: a Search for the Mixing Angle* ϑ_{13}*"*, arXiv:hep-ex/0405032v1

[Ard06]   F. ARDELLIER ET AL., DOUBLE CHOOZ collaboration: *"*DOUBLE CHOOZ*, A search for the neutrino mixing angle* ϑ_{13}*"*, arXiv:hep-ex/0606025v4

[Apo03]   M. APOLLONIO ET AL., CHOOZ collaboration: *"Search for neutrino oscillations on a long base-line at the* CHOOZ *nuclear power station"*, Eur. Phys. J. C **27**, 331-374 (2003) [arXiv:hep-ex/0301017v1]

[Bil99]   S.M. BILENKY ET AL.: *"Phenomenology of Neutrino Oscillations"*, Prog. Part. Nucl. Phys. **43**, 1-86 (1999) [arXiv:hep-ph/9812360v4]

[Bil01]   S.M. BILENKY ET AL.: *"Constraints on* $|U_{e3}|^2$ *from a three-neutrino oscillation analysis of the* CHOOZ *data"*, arXiv:hep-ph/0112216v1

[Blu10]   E. BLUCHER ET AL., DOUBLE CHOOZ outer veto group: *"OV electronics and test"*, DOUBLE CHOOZ internal document: DC-doc-1400-v1

[CC10]   CC IN2P3 WEB PAGE: `http://cc.in2p3.fr/` (16.11.2010)

[Cow56]   C.L. COWAN ET AL.: *"Detection of the Free Neutrino: a Confirmation"*, Science **124**, 103-104 (1956)

[DC10]   Double Chooz web page:
         http://doublechooz.in2p3.fr/ (16.11.2010)

[Gea10] Geant4 web page:
         http://geant4.cern.ch/ (16.11.2010)

[Gre10] D. Greiner, Universität Tübingen, *private communication*

[Hag00] T. Hagner et al.: *"Muon-induced production of radioactive isotopes in scintillation detectors"*, Astropart. Phys. **14**, 33-47 (2000)

[Hal84] F. Halzen and A. Martin: *"Quarks and Lepons"*, John Wiley & sons (1984)

[Hax95] W. C. Haxton: *"The solar neutrino problem"*, Annu. Rev. Astron. Astrophys. **33**, 459-503 (1995)

[Hub07] P. Huber et al.: *"Reactor Neutrino Experiments Compared to Superbeams"*, arXiv:hep-ph/0303232v3

[Irf10] CEA IRFU Homepage:
         http://irfu.cea.fr/ (16.11.2010)

[Jil96] C.J. Jillings et al.: *"The photomultiplier tube testing facility for the Sudbury Neutrino Observatory"*, Nucl. Instr. and Meth. A **373**, 421-429 (1996)

[Lac05] T. Lachenmaier: *"Double Chooz: Auf der Suche nach θ_{13} mit Reaktorneutrinos"*, http://www-zeuthen.desy.de/astro-workshop/vortraege/di-mi/session2/zeuthen_lachenmaier_2005.pdf (07.09.2010)

[Las09] T. Lasserre: *"Neutrinos oscillations: Status, on-going and up-coming experiments"*, talk at Launch 09, Heidelberg (2009)

[Leo94] W.R. Leo: *"Techniques for nuclear and particle physics experiments"*, Springer, Berlin Heidelberg (1994)

[Lub00] B.K. Lubsandorzhiev et al.: *"Studies of prepulses and late pulses in the 8″ electrontubes series of photomultipliers"*, Nucl. Instr. and Meth. A **442**, 452-458 (2000)

[Nov09] P. Novella et al.: *"DCRecoPulse"*, Double Chooz internal document: DC-doc-649-v2

[PDG10] K. Nakamura et al. (Particle Data Group), J. Phys. G (37), 075021 (2010)

[Per09] D. Perkins: *"Particle astrophysics"*, Oxford University Press, New York (2009)

[Pho02] S.O. FLYCKT AND C. MARMORIER (PHOTONIS): *"Photomultiplier tubes: principles and applications"*, Photonis, Brive (2002)

[Pov94] B. POVH ET AL.: *"Teilchen und Kerne"*, Springer, Berlin Heidelberg (1994)

[Roo10] ROOT WEB PAGE: `http://root.cern.ch/drupal/` (16.11.2010)

[Sch97] N. SCHMITZ: *"Neutrinophysik"*, Teubner Studienbücher, Stuttgart (1997)

[Tan06] A. TANG ET AL.: *"Muon simulations for* SUPER-KAMIOKANDE, KAMLAND *and* CHOOZ*"*, Phys. Rev. D **74**, 053008 (2006)

[Wur09] M. WURM: *"Cosmic Background Discrimination for the Rare Neutrino Event Search in* BOREXINO *and* LENA*"*, PhD Thesis, Technische Universität München (2009)

[Zbi08] K. ZBIRI: *"R1408 PMTs test note"*, DOUBLE CHOOZ internal document: DC-doc-103-v1

Danksagung

An erster Stelle möchte ich mich bei Prof. Franz von Feilitzsch für die freundliche Aufnahme an den Lehrstuhl E15 und viele interessante Gespräche über physikalische und auch nicht-physikalische Themen bedanken.

Des weiteren bedanke ich mich bei Prof. Tobias Lachenmaier für das Stellen eines interessanten Diplomarbeitsthemas und für die große Hilfsbereitschaft bei Fragen bezüglich dieser Arbeit.

Darüber hinaus vielen Dank an Prof. Lothar Oberauer für diverse interessante Diskussionen und die ansteckende Faszination für die Astroteilchenphysik.

Ein großes Dankeschön geht an Martin Hofmann für eine top Betreuung und das mehrmalige Korrekturlesen dieser Arbeit und der Vorträge, die ich im Rahmen dieser Arbeit halten durfte. Natürlich auch danke für die super Zeit bei den Meetings in Straßburg und Saclay.

Vielen Dank auch an Dr. Michael Wurm, der als erfahrener Myonenspur-Rekonstrukteur immer ein offenes Ohr für Fragen hatte. Außerdem möchte ich Quirin Meindl danken, der einen wichtigen Beitrag zur Realisierung der maximum likelihood Methode geleistet hat.

Bei Daniel Greiner von der Universität Tübingen möchte ich mich für die Hilfe bei diversen Problemen bezüglich DOGS und für die tolle Zeit in Chooz beim Austausch der inner veto PMTs bedanken.

Meinen Bürokollegen Andreas Zöller und Anton Röckl danke ich für eine sehr angenehme Arbeitsatmosphäre. Bei Andreas Zöller möchte ich mich besonders für die Hilfe bei programmiertechnischen Problemen bedanken und dafür, dass er eben der "Andiman" ist. Bei Anton Röckl bedanke ich mich für den bitter nötigen Frust-Kick im Garten des Chateaus nach der traurigen Niederlage der Nationalmannschaft gegen Spanien.

Ein großes Dankeschön geht an Maria Bremberger für die Hilfe bei organisatorischen Problemen und den nicht endenden Nachschub an Kaffee und Keksen.

Vielen Dank auch an Nils Haag für das Korrekturlesen der Arbeit und an alle Mitglieder des Lehrstuhls, die hier nicht namentlich genannt wurden. Die Atmosphäre am Lehrstuhl ist einfach super, was sicherlich auch an der immer vorhandenen Hilfsbereitschaft aller Mitglieder liegt. An dieser Stelle auch ein großes Dankeschön an alle Fußballer - vielleicht wird es ja nächstes Jahr was mit dem ersten Turnier-Tor.

Ein riesiges Dankeschön an meine Freundin Julia Königbauer, die immer an mich geglaubt und mich mit all ihrer Kraft unterstützt hat.

Auch meiner Familie ein dickes Dankeschön, dafür dass sie mir das Studium überhaupt erst ermöglich hat.